Coherence Effects in the Valence Photoionization of Small Molecules

vorgelegt von
Markus Ilchen
aus Pinneberg

Von der Fakultät II - Mathematik und Naturwissenschaften
der Technischen Universität Berlin
zur Erlangung des akademischen Grades

Doktor der Naturwissenschaften
– Dr. rer. nat. –

genehmigte Dissertation

Promotionsausschuss:
Vorsitzender: Prof. Dr. rer. nat. M. Dähne
Berichter/Gutachter: Prof. Dr. rer. nat. T. Möller
Berichter/Gutachter: Prof. Dr. rer. nat. J. Falta
Berichter/Gutachter: Dr. -Ing. J. Viefhaus

Tag der wissenschaftlichen Aussprache: 23. April 2012

Berlin 2012
D 83

Kohärenzeffekte in der Valenz-Photoionisation kleiner Moleküle

KURZFASSUNG

Die Untersuchung von Kohärenzeffekten in der Valenz-Photoionisation kleiner Moleküle ermöglicht Einblicke in molekulare Strukturen und Dynamiken und gibt dadurch Aufschluss über einige fundamentale quantenmechanische Prozesse. Der Schwerpunkt dieser Arbeit liegt auf derartigen Studien. Mittels Synchrotronstrahlung und der winkeldifferenzierenden Flugzeitanalyse von hierbei emittierten Photoelektronen werden molekulare Zwei-Zentren-Interferenzen für die Valenzelektronen der homonuklearen, diatomaren Moleküle N_2 und O_2 untersucht. Es wird gezeigt, dass durch die Inversionssymmetrie dieser Moleküle und die resultierende Unbestimmbarkeit des Emissionsortes der Photoelektronen Interferenzen auftreten. Die winkelaufgelöste Photoelektronenstudie in einem sehr großen Photonenenergiebereich von 20 bis 600 eV, die in dieser Arbeit vorgestellt wird, zeigt erstmalig sogenannte 'Cohen-Fano Oszillationen' in der Winkelverteilungsanisotropie. Es werden zudem weitere relevante Effekte der kohärenten Photoelektronenemission vorgestellt und im Lichte der gewonnenen experimentellen Daten analysiert. Eine energetisch hoch auflösende Studie von N_2 und O_2, besonders im niederenergetischen Photonenenergiebereich von 20 bis 50 eV, zeigt des Weiteren bisher unentdeckte Resonanzphänomene, die höchstwahrscheinlich verschiedenen Arten der Doppelanregung zuzuschreiben sind. Ausblickend wird eine Analyse für das polyatomare heteronukleare Molekül CH_4 von 20 bis 300 eV vorgestellt, um eine Diskussion über molekulare Multi-Spalt-Systeme anzustoßen.

Coherence Effects in the Valence Photoionization of Small Molecules

ABSTRACT

Coherence effects in the valence photoionization of small molecules deliver insight into molecular structures and dynamics which in turn allow to unravel details of fundamental quantum mechanical processes. The work presented in this dissertation primarily deals with such investigations, using third generation synchrotron radiation. The applied technique is angle resolving photoelectron time-of-flight spectroscopy. It is shown that due to the inversion symmetry of homonuclear diatomic molecules like N_2 and O_2 an indistinguishability of the electrons and corresponding delocalization leads to interference pattern in the angular distribution anisotropy. Such two center interferences are determined in a wide photon energy range from 20 to 600 eV in the valence photoionization angular distribution anisotropy. The observed oscillations will be discussed in the light of the Cohen-Fano formalism. The relevant photoionization dynamics of the broad photon energy study will be discussed. In this context, a high energy resolution study of N_2 and O_2 is presented for the low photon energy region from 20 to 50 eV, showing hitherto unexplored resonance phenomena most likely originated by different types of doubly excited states. In order to initialize a discussion about more complex molecular multi-slit systems, an angle resolving study from 20 to 300 eV is presented for the heteronuclear polyatomic molecule CH_4.

Contents

Chapter 1

Introduction

Phenomena like coherence and resulting interference effects of massive particles like electrons highlight the quantum world in an impressive and comparably easy accessible way [66]. The Young type double slit experiment with massive particles and its analogon, the molecular double slit, are two of the most popular experiments exploring the quantum world. It seems to be astounding that these effects still comprise new insights in the dynamics of quantum particles, but as argued in this work, angular distribution effects of electrons in such a molecular double slit experiment are hitherto almost unexplored. As Richard Feynman stated referring to the quantum double slit experiment in 1965 ([50] and references therein):

'... all of quantum mechanics can be gleaned from carefully thinking through the implications of this single experiment.'

One year later, Cohen and Fano [26] derived their famous formalism on molecular interference effects for the photoionization of N_2 and O_2 valences. They initially predicted oscillations in the photoionization cross sections caused by coherent electron emission from indistinguishable two emitter sites as it is the case for homonuclear diatomic molecules. Although their predictions were groundbreaking in the light of the quantum mechanical understanding at that time, it took 35 years to prove these oscillations for H_2 ([122] in [9]) and another 4 years until the first prove of N_2 ([107] in [9]). There is still no Cohen Fano proving data available for O_2 at all. The originally predicted interferences for the *valence ionization* of N_2 and O_2 have not been proven experimentally since the former experimental works are either located at low photon energies not in the expected period length of the oscillations or mostly dedicated to inner shell ionizations. A first approach on proving Cohen-Fano type oscillations for valence states of H_2, N_2 and CO was

presented in an article of Canton *et al.* (2011) [21] by analyzing the branching rations of several vibrational states. Two center interference signature in the valence ionization of CO was unexpected and the results of Canton *et al.* (2011) [21] will probably motivate further exploration on heteronuclear targets in the near future. Some months later Becker [9] commented in *'Nature'* on this very fundamental experiment which gives insight in the matter-wave analogy and the interference occurring in an molecular double slit experiment. However, no experimental prove as such is found for the electron angular distributions of these targets and no prove at all is available for the valence ionization of O_2. The investigation of angular distribution effects turns out to be a well-suited method for the exploration of such effects and is an essential complement to cross section studies. As Amusia put it in 1990 [2]: 'Collective effects show up in angular distributions just as in cross sections; in fact, investigation of the angular anisotropy can give even more detailed information of the photoionization process than a measurement of the total cross section'.

The presented work in this thesis shows precise experimental data in order to answer the questions arising from the long-standing discussion about real Cohen-Fano oscillations in the valence ionization of N_2 and O_2. The experimental challenge of this study lies in the very low valence ionization cross sections for high photon energies which calls for a very efficient spectroscopic setup. At the same time this setup needs to have a sufficient energy resolution in order to resolve the different valence states accurately.
During the work on this thesis a highly efficient angle resolving photoelectron spectrometer setup has been developed. Using highly brilliant storage ring based synchrotron radiation from BESSY II (Berliner Speicherring Gesellschaft für Synchrotronstrahlung) and DORIS III ('Doppel-Ring-Speicher' at the 'Deutsches Elektronen Synchrotron' (DESY), Hamburg) dense angular distribution data sets for N_2 and O_2 with a high statistical accuracy for the relevant photon energy range from threshold up to 600 eV were obtained. Since the development of this spectrometer setup and first tests of its capabilities as an photon beam online diagnosis tool were an essential experimental part during the work at DESY, the presentation of the experimental chapter was extended in this regard.

In addition to the investigations on real two-center interferences in the electron angular distributions, a general study of N_2 and O_2 covering the whole photon energy range from near threshold up to several hundreds of eV resulted in further

new phenomena observations. This study was motivated by the fact that the available angular distribution data indicates persisting discrepancies in molecular photoionization at low photon energies. In this range up to 50 eV phenomena like shape resonances and interchannel coupling effects have to be discussed in order to achieve a broad understanding of the underlying effects. These phenomena also stimulated an interesting debate [20, 38, 120, 126] which will be presented in detail in chapter 4 together with the new experimental data obtained by the spectroscopic setup developed during this thesis.

The thesis is structured as follows: First, an overview on the relevant physical basics is given before the experimental setup and the data analyzing process is described. Since the spectrometer setup is also used as a versatile online photon diagnosis tool for storage ring as well as free-electron-laser (FEL) based synchrotron radiation sources, a section highlighting the usefulness of the device is included. The scientific investigations on photoionization of the outer valence shells of N_2 just as data for the highest occupied molecular orbital (HOMO) of O_2 are presented in the light of existing theoretical and experimental findings. As most of the existing literature for these targets is dealing with effects in a low photon energy range from threshold up to $\sim$ 50 eV, a detailed analysis of the inherent effects is presented. The results at higher photon energies in the order of several hundreds of eV, exhibiting the interference effects due to electron emission from indistinguishable two emitter sites, are discussed for these targets within the Cohen-Fano formalism.
In a first examination, data for a more complex target, the heteronuclear polyatomic CH_4, is presented in the light of available theoretical and experimental data in the final experimental chapter prior the conclusion and the outlook.

Chapter 2

Atomic and Molecular Photoionization

In this chapter the relevant background for atomic and molecular photoionization in terms of electronic structures and dynamics will be presented. As it is necessary for the main part of the thesis, electron interference effects and coherence phenomena will be discussed in more detail. To facilitate the reception of the presented results and the discussion in chapter 4 for a broader group of recipients, the fundamentals in this chapter are methodically structured, beginning with the basics of atomic and molecular modeling. Subsequently, specific details being relevant for the phenomena described in this thesis are presented.

2.1 The Photoeffect

The classical concept of physics was enhanced to a new era of fundamental understanding when phenomena of quantum mechanical behavior were discovered. One of the effects showing a clearly excessive demand to the classical physics was the photoelectrical effect (or commonly 'photoeffect') Einstein explained mathematically in 1905 [42]. This effect shows that an electromagnetic wave (or 'photon') can only eject electrons out of a solid state when it overcomes a discrete electron binding energy. This implied quantization, found to be the 'Plank'sches Wirkungsquantum h' [102], of the energy and the observed interaction of matter and light is not explainable regarding the classical physical understanding of the 19th century.

Today's state of the art light sources like storage ring or free-electron-laser based

synchrotron radiation sources are able to tune the wavelength of the photons very accurately in a broad energy range which will be described more detailed in chapter 3. Concerning this work, the photon-electron interaction can be described in the simplest way regarding a photon with the energy $E = h\nu$, where h is the fundamental 'Planck'-constant and ν is the frequency of the electromagnetic wave hitting an atom or molecule which subsequently emits an electron if the photon energy is larger than the electron binding energy. This so called photoionization is described by the equation given by Einstein

$$E_{kin} = h\nu - E_{binding}. \tag{2.1}$$

In this equation the kinetic energy of the emitted electron is E_{kin}, $h\nu$ is the energy of the photon and $E_{binding}$ is the discrete binding energy of the electron. Beside photoionization the photoeffect is categorized in the inner and the outer photoeffect. The latter is also commonly called 'Hallwachs-effect' since Wilhelm Hallwachs discovered the electron emission from metal surfaces in 1886. The inner photoeffect describes e.g. electronic transitions within a semiconductor without ionization or regarding the concern of this thesis, the Auger effect (see section 2.4).
The discovery and utilization of the photoeffect is not only of fundamental quantum mechanical interest, it is also the basis of extensive studies concerning regenerative energy utilization and various other fields of applications. An example for a photoeffect based device applied in the experiments presented in this thesis is a diode for photon flux determination (see section 3.1.1).

2.2 Photoionization of Atoms

The **direct single ionization** of an atom induced by photon interaction, as pointed out in section 2.1, is the simplest showcase of the outer photoelectric effect. Depending on the binding energy of the ejected electron and the location of the created vacancy state in the target, there are several additional effects to be taken into account beside the direct single electron emission.
In addition to the described ionization process of equation 2.1, it has to be considered that with a certain probability part of the electron kinetic energy excites another electron (if present) due to electron correlation. Therefore, the kinetic energy of the photoelectron is decreased by an also quantized amount creating so called **'satellite lines'**.
Secondary effects like **fluorescence** or **Auger decay** can take place as a reaction

to the created vacancies due to the ionization process and will be described later on in this section.

If one of two excited electrons is emitted because of the relaxation of the other excited electron in a lower orbital, this sequential process is called **autoionization**.
The latter processes are based on electron correlation which is very essential for the understanding of atomic and molecular dynamics, but also for many phenomena in solid state physics.
In the following, the atomic structure will be discussed before highlighting the mentioned processes to set the base for an analysis of the relevant electron spectra discussed in chapter 4.

The genesis of atomic modeling is a complex historic development and will not be presented in a continuous way. Even though early quantum mechanical models like Bohr's atomic model [14] are not sufficient for a state-of-the-art description of an atom, some basic assumptions still have the validity to realize an easy access to this topic. Therefore, beside Schrödinger's description of the electrons as principally standing electromagnetic waves located in orbitals [115], some nomenclatures like the 'shell'-concept are mentioned in this thesis being aware of the very visualizing character. To give an overview on the electronic structure of an atom, the following discussion widely refers to the literature of Amusia in 'Atomic Photoeffect' [2], where also further details can be read.

The electronic structure of an atom can be described by the basic assumption that all electrons of an atom move in the coulombic field of the nucleus with the charge Z. In the neutral case Z is equal to the number of electrons N. The time independent Schrödinger equation neglecting all relativistic effects is given by

$$\hat{H}\Psi_E(x_1, ..., x_n) = E\Psi_E(x_1, ..., x_n) \tag{2.2}$$

where

$$\hat{H} = \sum_{n=1}^{N}(\frac{(-i\nabla_n)^2}{2} - \frac{Z}{r_n}) + \frac{1}{2}\sum_{n>q=1}^{N}\frac{1}{|r_n - r_q|} \tag{2.3}$$

Z is the charge of the nucleus, r_n is the radius vector of the nth electron and $N = Z$ for the neutral case. The electronic states are given by quantum numbers which are in contradiction to the classical physics unexceptional discrete values. The quantum numbers characterize the eigenvalues of an electronic system. These

electronic states in the coulombic field are n, l, m and s as the principal quantum number, the angular momentum quantum number, the magnetic quantum number and the spin projection quantum number [132].

The principal quantum number n characterizes the corresponding energy value of the electrons and represents the 'shell' in terms of the Bohr atomic model. In a very visual description one can point out n as the size of the orbital. Its values range from 1 to n where n is the valence shell and therefore the outermost shell containing electrons. An additional denotation for $n = 1$, 2, 3, 4, etc. are capital letters beginning with $K, L, M, N, \ldots$ proceeding alphabetically [132].

To each value l of the angular momentum correspond $2l + 1$ different functions $\Psi(\Theta, \Phi)$ with $-l \leq m \leq l$. The total number of different functions (total degeneracy of n) therefore is n^2 [2]. The values of l range from 0 to $n - 1$ and are also additionally denoted by the letters $s, p, d, f, \ldots$ proceeding alphabetically. This corresponds to the fact that the occurrence of these subshells is always 1 behind the n shell, i.e. the deepest p state is located in the second main shell ($n = 2, l = 1 \Rightarrow n - l = 1$). Visualized l gives the form of the orbital [132]. The angular momentum quantum number is essential for the discussion of angular distributions and will be extended in section 2.4 concerning the discussion of partial waves.

The magnetic quantum number m can take $2l + 1$ values for each l. Possible values are $-l, -l + 1, \ldots, +l$. It characterizes the orientation of the electron angular momentum. The spin projection quantum number s or also commonly m_s denotes the electron's internal angular momentum and may be either $\frac{1}{2}$ or $-\frac{1}{2}$ [132].
According to the 'Pauli Principle' [98], each state may be occupied by only one electron. Taking the information about quantum numbers and the fact of a successive filling of the orbitals, the electronic configuration of an atom specifies the occupancy of the individual levels. For completely filled levels in the Coulomb field the configurations are

$$1s2 \qquad 2s2, 2p6 \qquad 3s2, 3p6, 3d10 \qquad 4s2, 4p6, 4d10, 4f14 \qquad ... \tag{2.4}$$

The next step is to determine the behavior of an atom interacting with an electromagnetic field or more specific with a photon. A general description and a theoretical background can be found in literature (e.g. Möller (2010) [92], Bransden

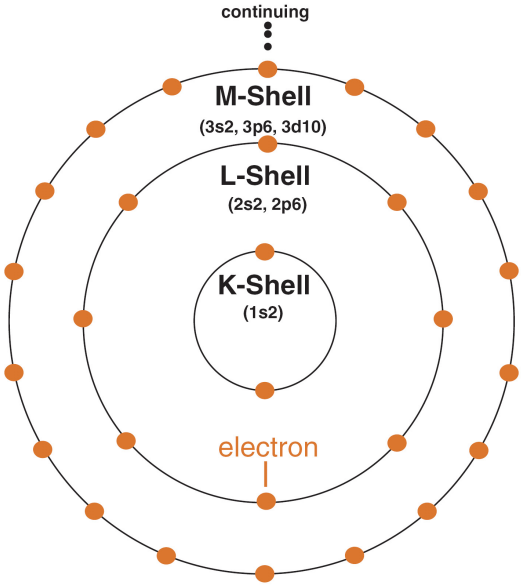

Figure 2.1: The figure illustrates the electronic occupation of atomic shells according to equation 2.4.

(1983) [16]). A basic assumption for the description of the electronic movement in an atomic system is the Born-Oppenheimer approximation which is based on the fact that the electrons move much faster than the nucleus (usually in the order of 3 to 5 magnitudes) [15]. In this respect, one can assume the electronic movement to be instantaneous and neglect the nuclear motion. According to the stationary Schrödinger equation described above, one can put the time dependent Schrödinger equation for the show case of a one-electron movement in an (hydrogenlike) atom as follows [16]

$$i\hbar\frac{\delta}{\delta t}\Psi(r,t) = [-\frac{\hbar^2}{2m}\nabla^2 + V(r,t)]\Psi(r,t). \tag{2.5}$$

The Hartree-Fock method is a common possibility to determine the orbital energies and the wave functions of many-body systems ab initio. It is the basis of most advanced theoretical models to describe atomic and molecular electronic systems and dynamics [3]. The method is based on the approximation that the electrons are only affected by the Coulombic field of the nuclei. The Hartree-Fock approximation has to be modified with respect to a collective electron excitation which can simplest be done in the frame of the 'Random Phase Approximation' (RPA) [3]. For a more general view in this context, one has to consider the rearrangement of all electronic states of a system after ionization. Not only the altered electronic states, but also the real secondary excitations or even further

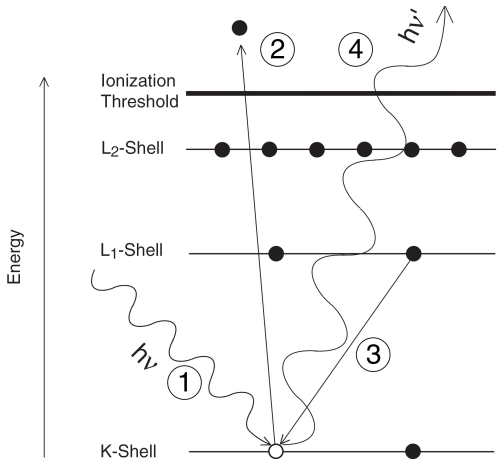

Figure 2.2: The figure illustrates a fluorescence decay after an inner shell ionization numbered as a sequential process.

ionizations have to be taken into account (electron correlation). A theoretical model for this is the 'Generalized Random Phase Approximation with Exchange' (GRPAE) [3]. Furthermore, interchannel interaction, leading to autoionization, decay processes and satellites shall be mentioned with regards to this. For a more detailed insight and an overview of advanced theoretical models of atomic interaction with photons the literature of Amusia in 'VUV and Soft X-ray Photoionization'(1996) [8] shall be announced for further reading.

The following processes were shortly mentioned above and will now be specified. They may occur after or simultaneous to photoionization of a target like e.g. an atom or a molecule underlining the great relevance of e.g. electron correlation effects not being implied in models like the basic Hartree-Fock model.

Fluorescence is a radiative decay of an excited electronic state. A fluorescence decay can take place when the initial and the final state have equal spins so there is no change in the spin projection quantum number. Usually the fluorescence photons have a larger wavelength than the exciting photons which is illustrated in figure 2.2. The fluorescence photons have discrete energies as it is the case for the electrons so fluorescence spectroscopy can be used for complementary insight into ionization dynamics.

The basic **Auger process** can take place when a core hole in e.g. an atom is created due to previous ionization or excitation. A less bound electron of a higher shell (the L-shell in the example of figure 2.3(a)) decays into the stronger bound state (the K-shell in the example) and releases energy of the amount $E_{Auger} = E_{K-shell} - E_{L-shell}$. This energy is sufficient (depending on the selection

rules and the correlated electron) to eject another electron with a binding energy $E_{binding} < E_{Auger}$. In the example shown in figure 2.3 another electron from the L-shell is ejected. This specific Auger process is therefore called 'KLL' Auger.

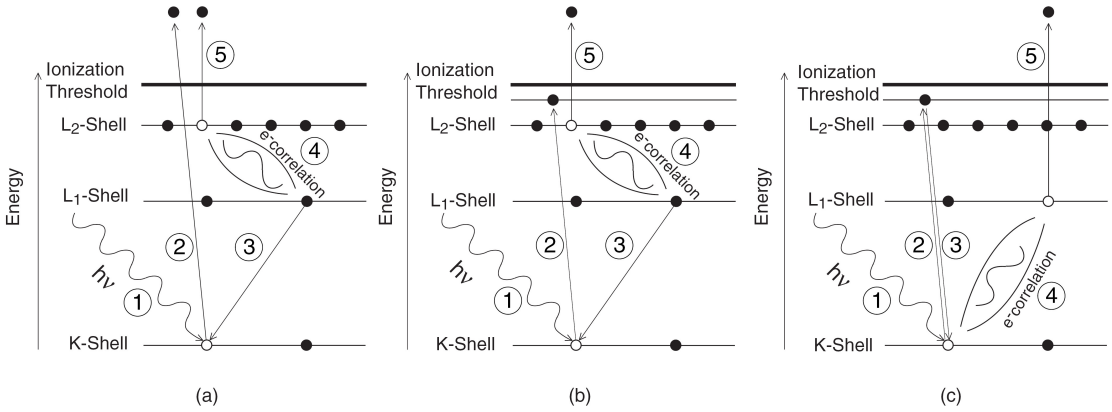

Figure 2.3: Figure (a) illustrates the Auger process for the example of a KLL Auger. Figure (b) and (c) are resonant Auger or autoionization processes. (b) shows the spectator case whereas (c) illustrates the participator case.

If the energy of the incident photon is not sufficient for a direct inner shell ionization, nevertheless exciting the electron in a bound state above the first ionization threshold, a resonant Auger electron can be emitted as it is shown in figure 2.3(b) [107]. In the resonant case the initially excited electron can be involved in this process as a spectator (figure 2.3(b)) or as a participator (figure 2.3(c)). In the latter case, the decay happens through the same channel as for the excitation. These processes (figure 2.3(b+c)) are called autoionization processes. **Autoionization** can also be triggered by vibrationally induced excitations in molecules. As discussed in section 4.1, also (doubly excited) Rydberg states can lead to autoionization.
The Auger decay is the competitive decay process to the fluorescence. According to figure 2.4 it is dominant for small atoms and molecules. The fluorescence cross section rises with higher Z of the atoms while the Auger yield decreases.

Regarding the case that beside ionization of a target part of the absorbed energy is exciting a second electron to a higher state due to electron correlation, the kinetic energy of the emitted electron is decreased by the amount of the secondary excitation energy.

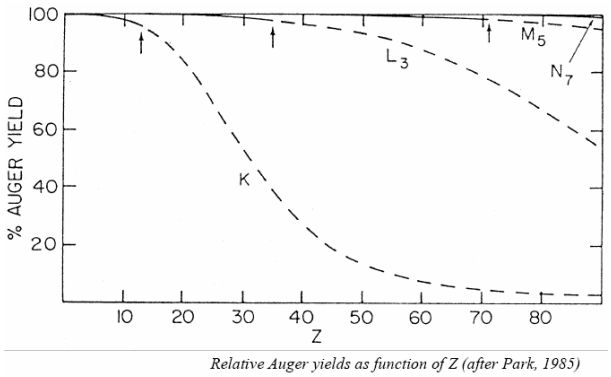

Figure 2.4: Illustration of the decreasing Auger yield with increasing Z in comparison to the also increasing fluorescence yield for selected orbitals according to [97].

$$E_{kin} = E_{h\nu} - E_{binding} - E_{excitation} \tag{2.6}$$

The possibility of this secondary process is again photon energy dependent and the resulting also discrete kinetic energies of the emitted photoelectron are called electron **shake up satellites** (see figure 2.5(a)). If $E_{excitation}$ is high enough to emit the second electron, the so called **shake off process** (see figure 2.5(b)) takes place in the frame of direct double ionization. More detailed information on this topic can be found e.g. in Hemmers (1993) [55].

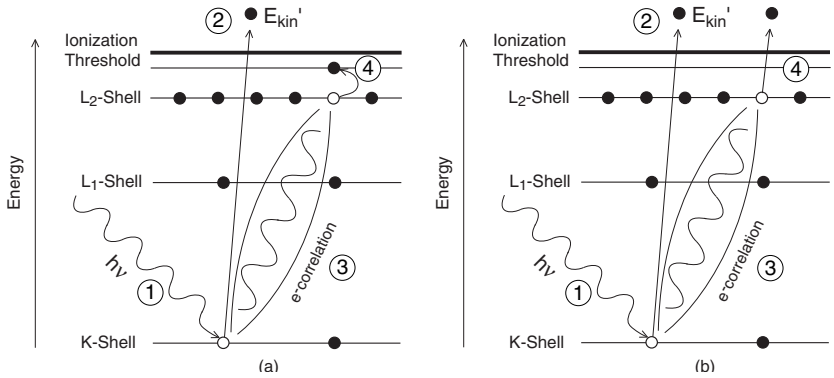

Figure 2.5: The left part of the figure (a) shows the shake up process whereas the right part (b) shows the shake off (or direct double ionization) case.

Additional non-linear processes are to be taken into account especially for strong field studies. Since their relevance is not essential for this work, I refer only to the extensive literature as e.g. [90, 113].
All the described effects have major influence on the interaction probability of a

photon with an atom or a molecule. This probability of interaction is called cross section and will be discussed in subsection 2.4.

2.3 Molecular Photoionization

Molecules and their electronic structures are much more complex in comparison to atoms, even though many of the described effects in 2.2 are similar. The simple sum of atoms is not equal to the molecule containing these atoms and its electronic structure changes by the formation of molecular orbitals. Due to this fact one has to exceed the given model qualitatively and quantitatively. Further parameters, namely vibrational and rotational dynamics of a molecule, have to be taken into account leading to the following adaptation of the photoeffect in 2.1:

$$E = h\nu - E_{binding} - E_{vibration} - E_{rotation} \tag{2.7}$$

Regarding the case that the nuclear distance is R, the electron coordinates are r, the kinetic energy of the nuclei is E_n, the kinetic energy of the electrons is E_e and the Coulomb potential for all particles is V, the Hamiltonian (in atomic units) can be written as [57]

$$\hat{H} = E_n(R) + E_e(r) + V(r, R). \tag{2.8}$$

In consequence the Schrödinger Equation can be written as [57]

$$[E_n(R) + E_e(r) + V(r, R)]\Psi(r, R) = E\Psi(r, R). \tag{2.9}$$

The assumption that the electrons move much faster than the nuclei (Born-Oppenheimer approximation see section 2.2) is also a widely valid and important approximation for molecular systems. The principal validity of the approximation leads in the molecular case to the simplification that the vibration of the molecule can be separately treated from the electronic motion as an electronic potential variation due to a change of the internuclear distance R.
According to the **Franck-Condon-Principle**, the probabilities of an electronic transition are therefore influenced by the compatibility of the vibrational wave functions of the initial and the final electronic state [107]. Therefore, electronic transitions have a higher statistical probability when the nuclei movement is neglected. This can be written as

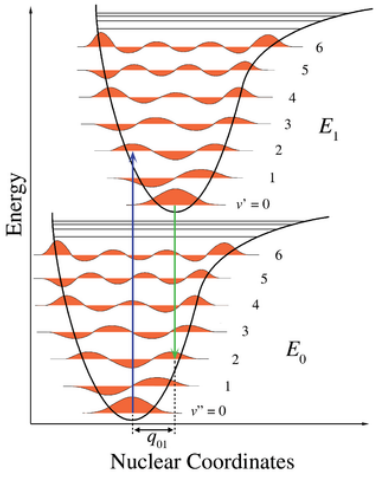

Figure 2.6: The Franck-Condon principle is illustrated using the example of a diatomic molecule. The arrows show transitions between different vibrational states. The figure is taken from [49].

$$P = \left\langle \psi_v^{'} | \psi_v \right\rangle * \left\langle \psi_\epsilon^{'} | \mu_\epsilon | \psi_\epsilon \right\rangle \tag{2.10}$$

where the left multiplier is the overlap integral or the so called 'Franck-Condon Factor' and the right multiplier is the orbital selection rule [144]. The shown principle is valid for low vibrational states where the molecule can approximately be treated as a harmonic oscillator. It has to be modified going to higher vibrational excitations. This can be done by implementing the 'Morse Potential' which compensates the lacking harmonic behavior at higher vibrational states [57].

The rotational energy of a molecule can stringently be considered regarding the common angular momentum rules. If the rotational quantum number is N and the momentum of inertia in the ground state is $I_0 = \mu R_0^2 \simeq \mu \langle r \rangle^2$, the rotational energy can be written as [57]

$$E_N = \frac{N^2}{2\mu R^2} \simeq \frac{\hbar^2}{1\mu\langle r\rangle^2} = \frac{m_e}{\mu} E_e. \tag{2.11}$$

The resulting energies of vibrational and rotational energy can therefore be calculated to be in the order of 0.1 eV and 0.001 eV.

A common model for the formation of molecular orbitals according to Lennard-Jones is the linear combination of atomic orbitals (LCAO) [79]. According to Hund and Mulliken ([88] and references therein) molecular orbitals (MO) can be formed by linear combination of independent atomic orbitals to a finite basis. Every electron is then located in a newly defined molecular orbital which is typically delocalized for the whole molecule. The limitation of this method is the implied statistical independence of the electrons and therefore a neglect of

electron correlation. Taking the simplest system as a showcase one can get an intuitive idea of the linear combination of two hydrogen atoms: Each 1s electron of a hydrogen atom has the wave function Ψ_{1s}. Combining the two is possible in two ways, namely in summation or subtraction of the wave functions. Summation $\Psi_{1s} + \Psi_{1s}$ leads to a rotational symmetric MO which has a binding character due to the increased charge density between the atoms. This combination has a 'gerade'-symmetry. Subtraction $\Psi_{1s} - \Psi_{1s}$ leads to a repulsion of the atoms and forms an anti-bonding orbital with a 'ungerade'-symmetry which has a decreased charge density between the atoms.

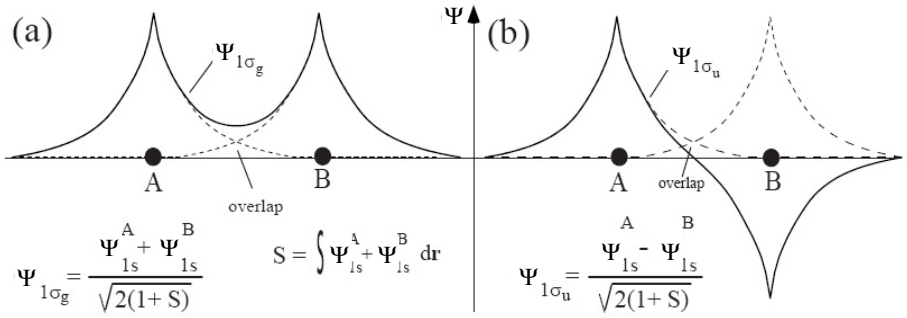

Figure 2.7: The figure is showing the different symmetric possibilities of MO forming for the case of hydrogen taken from [107]. The charge density is Ψ^2 and the plot nicely illustrates that the 'ungerade' symmetry causes a density node between the two atoms indicating the atomic repulsion.

For homonuclear diatomic molecules the electronic states are inversion symmetric which leads to an indistinguishable atomic affiliation of the electrons. This is a basic parameter for two center interference effects in the photoionization of homonuclear diatomic molecules as this is the main topic of this thesis and is valid for inner shell as well as valence electrons. Regarding the LCAO for the example of helium having two electrons in the 1s state both a bonding as well as an anti-bonding orbital would be formed. Therefore, no chemical bonding of the two He atoms is possible, but due to Van-der-Waals interaction the formation of a dimer with a very low binding energy is possible [125]. The bond length is experimentally proven to be > 50 Ångstrom which corresponds to a binding energy of $\sim 100\ neV$ [16, 52]. In such systems recently explored effects like 'Inter Coulombic Decay' (ICD) can be studied [72, 93].

Another theory on the formation of molecular orbitals is the 'Valence Bond Theory' developed by Heitler and London. This method is not as common in state-of-the-art theoretical calculations as e.g. the self consistent Hartree-Fock method and shall only be mentioned at this point[1]. Homonuclear diatomic molecules like N_2 and O_2 are much more complex in comparison to H_2 but can still be described in the MO theory. Figure 2.8 shows the LCAO MO for N_2 as an example of molecular orbital nomenclature and in order to depict the relevant orbital binding energies which is important for the discussion in chapter 4. In accordance to figure 2.7, this figure illustrates e.g. for the inner shell orbitals that the ungerade orbital formation leads to a decreased binding energy due to a lower probability of charge density between the atoms.

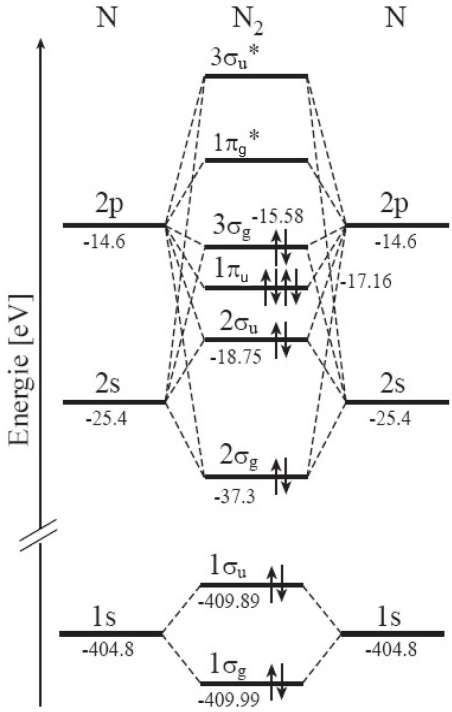

Figure 2.8: LCAO MO diagram of molecular nitrogen. The figure is taken from [107] and references therein.

[1] Further details can be read in e.g. [16, 57].

2.4 Partial and Differential Cross Sections

Regarding the interaction of a photon with matter and more specific the ionization process according to 2.1, it is obvious that a determination of the interaction probability, the so called cross section, is of high interest. This parameter includes much information on the electronic structure, the quantum mechanical processes in the ionized target and the general dynamics of a system. Classically it is understood to be the ratio of absorbing area of a target divided by the total area of the target. The most common unit in literature is [barn] for the cross section or also commonly used as [Megabarn] which is not an SI unit. To point out the formally correct description it shall be announced that according to e.g. [55]

$$1Mb = 10^{-22}\ m^2. \tag{2.12}$$

Quantum mechanically the cross section is given by the transition probabilities between two electronic states [55]. This is shown in Fermi's Golden Rule [48]. It determines the probability of a transition from an eigenstate to the continuum due to the interaction with an electromagnetic field.

$$T_{i\to f} = \frac{2\pi}{\hbar}|X|^2\delta(E_f - E_i - h\nu) \tag{2.13}$$

with the transition matrix element

$$X =< \Psi_f|\hat{H}_{pt}|\Psi_i > \tag{2.14}$$

$T_{i\to f}$ is the transition probability, Ψ_i the initial, Ψ_f the final wave functions with given eigenvalues $E_{i,f}$ and the perturbing Hamiltonian is $\hat{H}_p t$ [107].
If one of the states is located in the continuum, the process is called ionization [55]. The total ionization (or absolute) cross section has been studied extensively since decades giving the absolute probability of a photon-electron absorption for a whole target (as e.g. relevant for this work [18, 53, 58, 147]). Methods like e.g. electron-energy-loss-spectroscopy or photo-absorption-spectroscopy are able to determine total ionization cross sections [8].
The spectrometer setup introduced in chapter 3 will intrinsically be able to determine partial photoionization cross sections. For the determination of absolute cross sections the voluminous variety of parameters like actual gas pressure in the interaction region, quantum efficiency dynamics of a photo-diode and absolute photon flux of the photon-source make such a determination very challenging. Nevertheless, in principle it will become possible with the experimental setup. Although absolute ionization cross sections are a powerful indicator for electronic

structures and dynamics of atoms and molecules, it provides only information about the whole system interacting with the photon. For a more selective understanding of the cross section development for single orbitals one has to analyze the so called partial cross section given by

$$\sigma_{if}(h\nu) = \frac{4\pi^2\alpha a_0^2}{3} h\nu |M_{if}|^2 \tag{2.15}$$

In this equation the matrix element M includes the dipole approximation and gives the transition probability between the initial and the final state [8]. The dipole approximation assumes the electromagnetic field of the photon beam where $e^{(ikr)}$ expressed as a Taylor-series expansion $1+ikr+\ldots$ can be truncated to unity [13, 56].

$$|M_{if}|^2 = |\langle f|\Sigma r_\mu|i\rangle|^2 \tag{2.16}$$

Partial cross sections have an excitation energy dependent behavior, as it is the case for absolute cross sections, which is affected by many effects like delayed onsets, shape resonances or Cooper minima [8]. Furthermore, many-electron dynamics are reflected in the partial cross section. In former times when first investigations on this topic were performed, discrete photon sources were used. This is a severe limitation for these studies [8]. Today's tunable light sources, such as storage rings or free-electron-lasers, allow very highly resolved studies of partial cross sections in a wide energy range (see section 3.2). These sources improved the situation of such science in a remarkable way. Facing the circumstance that the angular momentum quantum number, or more visual the shape of an orbital, plays a major role in terms of the direction in which an electron is most probably emitted one can implicitly understand the need of a differentiation of the spatial emission distribution.

This so called differential cross section is the derivative of the partial cross section with respect to the solid angle.

$$\frac{d\sigma_{if}(h\nu)}{d\Omega}(\Theta) = \frac{\sigma_{if}(h\nu)}{4\pi}[1 + \beta_{if}(h\nu)P_2(cos\Theta)] \tag{2.17}$$

where σ is the total cross section, Ω is the solid angle, Θ is the photoelectron emission polar angle measured between the electric vector ϵ and the photoelectron momentum vector p, $P_2(cos\Theta)$ the Legendre polynomial of second degree and β is the dipolar angular distribution anisotropy parameter, ranging from 2 ($\frac{d\sigma}{d\Omega} \sim cos^2(\Theta)$) to -1 ($\frac{d\sigma}{d\Omega} \sim sin^2(\Theta)$) [8, 149].

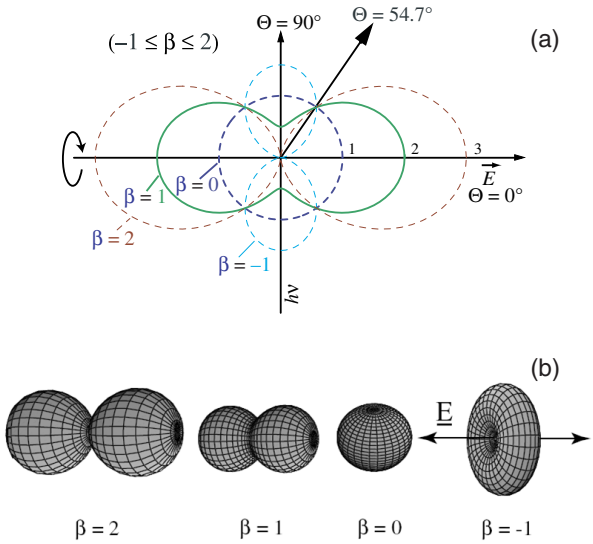

Figure 2.9: The figures show the different possible angular distribution anisotropies ranging from -1 to +2 according to equation 2.17. In the two dimensional figure (a) the angle at 54.7° called *magic angle* is pronounced since no angular distribution anisotropy is influencing this angular position. Figure (b) visualizes different angular distribution cases in a three dimensional plot. Both are provided by [137].

The angular distribution possibilities and the given physical range are plotted in figure 2.9. It can be derived from the equation above or directly seen in figure 2.9(a) that at the angle $\Theta = 54,7^{\circ}$, the differential partial cross section becomes proportional to the integral partial cross section. All other angles yield information about β for a known σ [8]. This angular distribution information is sensitive to the phase of the quantum mechanically possible ionic states and is therefore an essential addition to the cross section information. The more generalized Cooper-Zare model for an LS coupled system can be written as [27]

$$\beta = \frac{l(l-1)R_{l-1}^2 + (l+1)(l+2)R_{l+1}^2 - 6(l+1)R_{l-1}R_{l+1}cos(\delta_{l+1} - \delta_{l-1})}{(2l+1)[lR_{l-1}^2(l+1)R_{l+1}^2]} \quad (2.18)$$

where R are the radial integrals and δ the phase shifts of the respective partial waves [8].

For the photoionization of diatomic molecules Chang *et al.* (1978) [24] predict a classification of the photoionization process according to their degree of parity [59]. They point out that parity unfavored transitions like $\Sigma^{\pm} \rightarrow \Sigma^{\mp}$ lead to a β of -1, whereas the parity favored transitions which are the vast majority lead to higher β-values.

A striking fact arises from this formalism, since the quality of the β data scales linearly with the quality of the σ data which is usually taken from literature as further described in section 3.1.3. Therefore, the need for precise σ- as well as

β-databases is crucial and an essential basis for this work in order to analyze very small angular distribution effects .

The anisotropy parameter β is based on the dipole approximation which is believed to be a valid concept for low kinetic electron energies up to $\sim 1\ keV$ in several references (initial work from [29]). However, several recent articles are dealing with a breakdown of this approximation also for kinetic electron energies in the order of few hundreds or even few tens of eV (e.g. [56, 81, 130] and references therein). The threshold for the need of a multipole consideration in order to describe the photoionization process properly is remaining a topic under discussion in the extensive literature (e.g. Hemmers *et al.* (2004) [56] and references therein). As Hemmers points out in that work, two arguments are crucial for the assumption that the dipole approximation should be valid at least for the UV photon energy range: (a) A neglect of relativistic effects, because the photoelectron kinetic energies are very low compared to the speed of light. (b) A mitigation of higher order effects due to photon wavelengths larger than the electron orbitals. Nevertheless, experiments have observed non-dipole effects even down to 13 eV [86]. Regarding these findings non-dipole effects also play an interesting role concerning the results presented in chapter 4 where mainly the dipole anisotropy parameter β is taken into account. The theoretical work of Toffoli *et al.* (2006) [130] also predicts strong signatures of two center interferences in the photoionization of N_2 for the non-dipole parameters γ and δ, however they were not investigated in the frame of this thesis. Further consequence due to these complementary insights into angular distributions will be discussed in the outlook of this thesis.

The first order non-dipole formalism according to Cooper [28] can be written as

$$\frac{d\sigma(h\nu)}{d\Omega} = \frac{\sigma_(h\nu)}{4\pi}\{1 + \beta(h\nu)P_2(cos\Theta) + [\delta(h\nu) + \gamma(h\nu)cos^2\Theta]sin\Theta cos\Phi\} \quad (2.19)$$

where δ and γ are the new first order non-dipole parameters [56] and Φ is the azimuthal angle relative to the photon propagation axis (see figure 2.10).

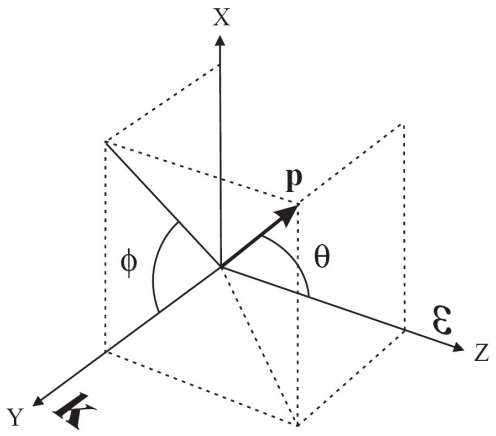

Figure 2.10: The figure and the caption are taken from [56]. It shows the relevant parameters for a non-dipole consideration induced by linearly polarized light. ϵ is the photon polarization vector, p the momentum vector of the photoelectron. The angle between the two is Θ. Φ is the azimuthal angle between the propagation vector k and the projection of p in the x-z plane.

2.5 Molecular Interference and Scattering

In molecular photoionization the electrons have certain possibilities to interact with the neighboring atom's states or with itself due the molecular orbital in terms of scattering and delocalization of the electronic state. The underlying concept is the wave-particle dualism being part of the interpretation of the photoelectrical effect described in section 2.1. The double slit experiment with massive particles gives insight in the most fundamental quantum mechanics and is topic of extensive theoretical and experimental work (initial work by [26, 66]). As pointed out in the introduction, one should be able to achieve a widespread understanding of quantum mechanics just by the implications of this experiment.

In this section the mechanics of these phenomena are briefly introduced, preferably referring to the literature of Rolles (2010) ([108] in [45]) showing a comprehensive overview on this topic.
A young type double slit [150] is based on the assumption that a coherent wave is passing a double (or multi) slit with a slit width in the order of the wavelength. Due to the wave nature of the light which can unambiguously be proven by this experiment, intensity variations due to interference between the different paths can be observed behind the double slit. In a classical treatment this is only possible regarding waves, but since the discovery of the wave-particle dualism it is also reasonable to be valid for particles. The basis for this effect is the indistinguishability of the paths leading to a final state. The original Young experiment can stringently be adapted for particles having a deBroglie wavelength of $\lambda = \frac{h}{p}$. In case of an electron passing through a double slit with equal probability for both slits, one has to sum up both possible wave functions as it was already introduced

in section 2.3. The squared absolute value of this summation is giving the spatial probabilities for a detection and therefore the occurring minima and maxima in intensity.

$$|\Psi^2| = |\Psi_1 + \Psi_2|^2 = |\Psi_1|^2 + |\Psi_2|^2 + \Psi_1^*\Psi_2 + \Psi_1\Psi_2^* \tag{2.20}$$

One striking example for a particle interference is the molecular double slit (see figure 2.12(a)) which is in the simplest form given by a homonuclear diatomic molecule. As described in section 2.3 the formation of molecular orbitals leads to delocalized states of the electrons and in the special case of equal atoms to inversion symmetry of the molecular constituents. The electron can therefore be indistinguishably emitted from one or the other atomic site. Quantum mechanically stringent the electron can be interpreted to do both so its wave functions interfere showing an energy dependent intensity fluctuation given by the equation above. This molecular double slit was investigated in recent works of e.g. [21, 107, 130, 151] and was already predicted to be seen in a modulation of total photoionization cross sections by Cohen and Fano in the year 1966 [26]. Proof for this oscillation can also be found in the angular distribution of the emitted photoelectrons which is symmetric but different for the two cases of the 'gerade' or the 'ungerade' state (figure 2.7). The Cohen-Fano oscillation will be discussed in detail in chapter 4 and is the underlying phenomenon of the main part of this work.

Regarding the case that the electron is emitted from a localized state, according to Heisenberg, no interference should be seen. In this case only scattering processes and orbital momenta are influencing the angular distribution of the electrons. Scattering phenomena occur in various possible ways. Regarding the case illustrated in figure 2.12(b) for the example of nitrogen, the emitted electron has equal probabilities to be ejected pointing away from the molecule or pointing to the neighboring atom. In case the electron is ejected in the direction of the neighboring atom it can be recoiled and afterwards taking the same path of the opposite case (path (1) in figure 2.12). These different paths interfere, unless the timing or the momentum changes can be determined [151]. This would be the case when the deBroglie wavelength becomes shorter than the bond length of the molecule, since the momentum change is big enough to induce localization and therefore loss of coherence [151]. Although with small probability, double scattering can also occur as it is illustrated in figure 2.12(c). Comparing homonuclear and heteronuclear molecules, the two center interference as illustrated in figure

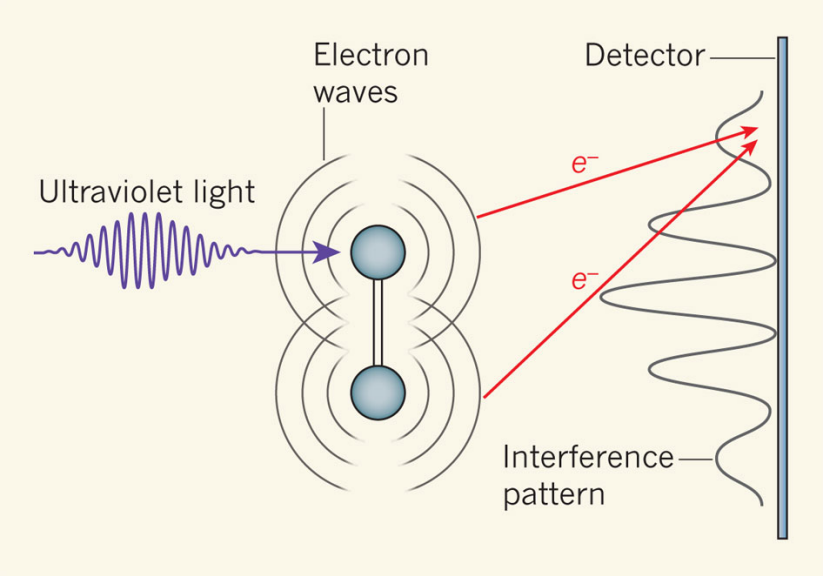

Figure 2.11: The figure is taken from [9] showing the principle of a molecular double slit.

2.12(a) can be switched on and off due to a corresponding on/off condition of electron localization [107]. Therefore, the scattering and non-scattering phenomena can be separately studied e.g. comparing CO and N_2 as it was done for the inner shell ionization by Zimmermann *et al.* (2008) [151]. However, this thesis is dedicated to the valence ionization of homonuclear diatomic molecules where the described scattering phenomena are smaller than in the inner shell ionization due to a stronger delocalization of the MOs. Further examples of coherent emission in molecular photoionization are predictable whenever the ionization conditions are chosen in a way that indistinguishability of probable paths leading to the same final state is given. A more detailed discussion of such effects in the light of this work will be presented in chapter 4.

A highly interesting and extensively debated phenomenon in molecular photoionization is the shape resonance which is important for the presented discussion in chapter 4. Shape resonances are above-threshold continuum resonant processes often described as a resonant process of core electron emission [16, 100, 107]. Indeed, this is the most common type of a shape resonance even though every orbital can be investigated separately in terms of a resonant feature depending on the molecular orbital shape. A detailed overview on the historical development and the different approaches of explanation are given by Piancastelli (1999) [100]. Shape resonances are mostly attributed to an enhanced cross section,

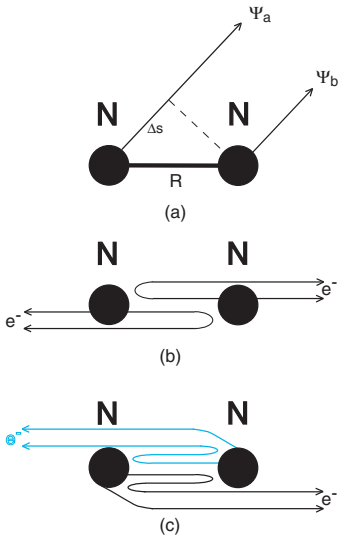

Figure 2.12: The figure is showing the principles of coherent emission from indistinguishable two emitter sites for the example of N_2(a), the single scattering case (b) and the double scattering case (c) also for N_2. The illustration is created in the style of [107, 151].

rapidly changing angular distribution anisotropy or non-Franck-Condon vibrational branching ratios in the process of direct photoionization via a single electron emission into the continuum state [124]. There are different understandings of the nature of a shape resonant enhancement of the cross section. One states the enhancement to occur due to a trapping of an outgoing electron by a potential barrier through which the electron eventually tunnels and emerges in the continuum [100]. The other one relates them to unoccupied molecular orbitals embedded in the continuum [100]. The latter understanding will be adapted for the discussion about shape resonances in the valence ionization of N_2 and O_2 (see section 4.1).

Chapter 3

Experimental Setup

In this chapter a short overview on different techniques for angle resolving photoelectron spectroscopy (ARPES) is given followed by a detailed presentation of the ARPES experimental setup developed during the work on this thesis. The general experimental setup including the applied light sources and beamlines, the data acquisition and processing as well as the relevant setup and data calibration procedures will be introduced. Since the presented spectrometer setup is beside its scientific use dedicated to be an online photon beam diagnostic unit and several beamtimes have been performed in this concern, a separate section will highlight this capability. Furthermore, the applicability of the developed spectrometer setup to (X)FEL photon sources for angle resolving electron studies and beam diagnosis is discussed in a further section of this chapter.

Basically the investigation of atoms and molecules in terms of structural and dynamical properties of the electronic and also the nuclear motion can be performed in various ways. The method applied in this work belongs to *spectroscopy*, especially to spectroscopy with soft X-ray photons in the range from $\sim 15 - 1000\ eV$. Electron emission and photon absorption phenomena due to the interaction of photons with matter in this photon energy regime play a key role for a deeper understanding of atomic and molecular properties. Chemical dynamics, structural insights and most fundamental mechanics of the quantum world like e.g. the two center quantum interferences being main part of this work, can be investigated by photon-matter interaction. Since all constituents of residual gases in an experimental setup using soft X-ray photons have high absorption cross sections, it is basic for all presented experimental techniques below to ensure ultra-high vacuum (UHV) conditions. This is not only crucial for the photon transmission, but also for reducing additional signal of such residual gases to the

signal of interest.
The spectroscopic variety also includes investigations with even lower energy photons. Radiofrequency (RF), microwave, infrared (IR) and ultraviolet (UV) spectroscopy are methods to determine e.g. rotational and vibrational energies of molecules, electron spin properties and electronic excitation [57]. Such investigations are able to excite and resolve very low energy phenomena less important for this thesis. The part of the UV spectroscopy sensitive to vibrational molecular energy levels is an overlapping spectroscopic field, since vibrational excitations will play an essential role in the interpretation of the low photon energy data discussed in chapter 4.

3.1 Angle resolving photoelectron spectroscopy

Photoelectron spectroscopy (PES) is a widely established method used to determine atomic and molecular electronic states and their dynamics. Apart from atomic and molecular physics PES is also an important technique for studies of clusters and solid states [35, 145].
It is particularly suited for the investigation of surfaces limited to few nanometers depth of penetration (depending on the system, incidence angle etc.)(e.g. [71]). The electron movement after the ionization of deeper lying surface atoms suffers from too many scattering processes with neighboring atoms rising a limitation of PES in this respect. Furthermore, it is suitable for the investigation of liquids. A more general description of state-of-the-art use of PES can be found in several text books (e.g.[8, 57, 62, 94]). Parameters like electronic energy-, angular- and spin distributions can be studied using PES [71]. Since its advent in the year 1957 and the Nobel prize for Kai Siegbahn in 1981 for this development [117], the technique and the apparatus of PES studies have been widely established and highly improved.

Investigating free atoms and molecules in the gas phase with PES has the advantage to study the electronic structure that the interaction of electrons with the neighboring atoms can be approximately disregarded for most cases. In this case, electrons and ions can propagate freely in space. However, influencing parameters like the surrounding magnetic field, e.g. the earth's magnetic field if not shielded properly, as well as charged parts of the interaction volume have to be minimized especially in the particular case of this work. One of the possible influences is the *space charge effect*. When the density of ionized matter becomes so big that the

charge of the ionized target cannot be ignored in terms of influencing electron propagation, Coulomb interaction has to be taken into account. In recent PES gas phase experiments these problems occur using extremely short and intense photon pulses of (free-electron-) lasers. Space charge effects and can be neglected for the presented experiments in this work as they are mainly performed at storage ring based synchrotron radiation sources which usually do not create high peak charge densities due to their orders of magnitude lower peak photon flux.

There are various techniques allowing angle resolving studies on photoelectrons. To mention some of the most common techniques, there are hemispherical analyzers, reaction microscopes, velocity map imaging analyzers and time-of-flight (TOF) detectors like the spectrometer setup presented in the following section or magnetic bottle type spectrometers. A brief introduction of these techniques will follow later in this section. All of these analyzers typically use micro channel plates as an initial amplification of the incoming particles. Every angle resolving photo electron spectroscopy technique has its own advantages and disadvantages which shall briefly be characterized. For time-of-flight analyzers it is crucial to work with a pulsed light source. In this concern, it is essential for time-of-flight spectrometer setups that a sufficient photon pulse spacing is ensured so that all relevant kinetic energies can be covered within the individual spectra. Many storage ring facilities offer special 'few-bunch-mode beamtimes' in order to ensure the required photon pulse spacing. Also (free-electron) lasers are intrinscically pulsed light sources. For the special case of electron time-of-flight spectroscopy the pulse period whichs allows an appropriate acquisition time has to be commonly in the order of some hundred ns.

Figure 3.1 shows a general design sketch of a hemispherical detector. The advantages of such an electro-static analyzer are the good commercial availability and its additional applicability to continuous wave light sources such as lab based rare gase UV lamps or X-ray tubes. Usually, this method does not exploit the timing structure of e.g. synchrotron radiation sources. They allow for very high energy and angular resolution. However, size and budget constraints are in turn limiting the detected solid angle which is a big concern especially in low target density applications typical for atomic and molecular (AMO) experiments.

Reaction microscopes and velocity map imaging analyzers can be stated to be a compromise of high transmission with moderate angular distribution capability

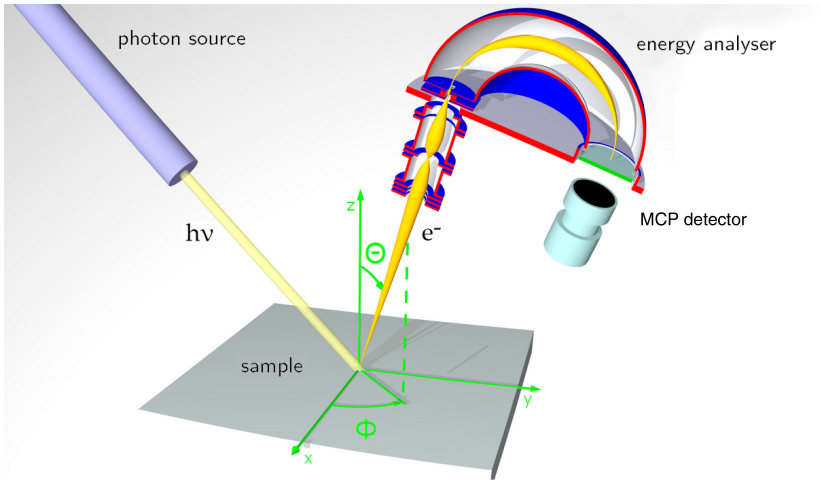

Figure 3.1: The figure shows a typical hemispherical electron spectrometer design as it is used in this showcase for surface PES. The figure is taken from [110].

and they are limited to low kinetic energies of at maximum few hundreds of eV depending on the electric and magnetic field properties. Detailed information on these techniques can be found in Ullrich *et al.* (2003) [131] and Eppink *et al.* (1997) [44] respectively.

The advantage of magnetic bottle type spectrometers, which is a special type of time-of-flight spectrometer, is the high solid angle they are able to acquire in a relatively broad kinetic electron energy range depending on the magnetic field properties of the implemented permanent magnet (see figure 3.2). Angular resolution is typically not available. Also the timing resolution is slightly lower than in the other TOF-techniques due to the inevitable flight time differences of electrons emitted in the direction of the detector and antipodal emitted electrons. A broadening of the electronic peaks in the spectra is therefore observed. Reducing this effect by using innovative magnet setups is part of another PhD thesis carried out in the workgroup of Jens Viefhaus[1]. Nevertheless, this method has the advantage of a very high efficiency also at higher photon energies and therefore many experiments representing high impact sciences, magnetic bottle spectrometers have been enabled, for example Mucke *et al.* (2010) [93] and Eland *et al.* (2003) [43]. A combination of a magnetic bottle type spectrometer with an additional ion

[1]PhD thesis of Sascha Deinert at the P04 Variable Polarization XUV (eXtreme ultraviolet) Beamline at PETRA III (Positron-Elektron-Tandem-Ring-Anlage), DESY in Hamburg (Germany). Beamline scientist in charge: Jens Viefhaus (jens.viefhaus@desy.de)

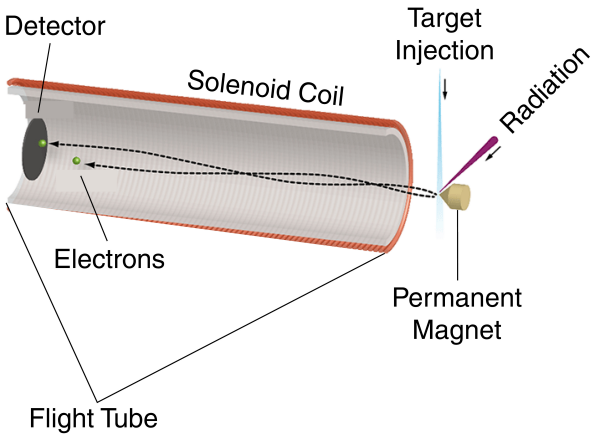

Figure 3.2: The figure shows the basic design of a magnetic bottle type electron spectrometer. A strong permanent magnet in the very near of the interaction region of projectile and target is pushing the ejected electrons in the direction of the detector. A solenoid coil wrapped around the flight tube forms the electron trajectories in order to achieve a maximum transmission and a homogeneous exposure of the active detection area. The figure is adapted from [106].

time-of-flight spectrometer arises the possibility of photoelectron-photoion coincidence spectroscopy (PEPICO). This technique turned out to be very powerful, since it allows both the highly efficient single determination of electrons and ions, as well as coincident event recording of both (e.g. [47, 70] and references therein).

The spectrometer setup chosen to be best suited for this work enables a high angular resolution with a still large solid acceptance angle being able to record spectroscopic AMO data over wide photon energy ranges up to the hard X-ray regime. Due to the exploitation of the synchrotron radiation timing structure in terms of time-of-flight spectroscopy it is possible to record spectra which intrinsically cover all occurring electron kinetic energies. The simultaneous sampling of the whole electron kinetic energy spectrum implies reduced dark counts and noise as well as reduced influence of fluctuations or drifts in the photon flux [8]. As Becker (1996) points out, TOF-spectroscopy is well suited for near threshold spectroscopy which is a basic requirement for several of the presented results in chapter 4. The capability of high voltage retardation of the incoming electrons is also essential for wide photon energy range studies. Figure 3.3 shows such a micro channel plate (MCP) based electron time-of-flight spectrometer, as it is part of the spectrometer setup used for the studies presented in this work. Further

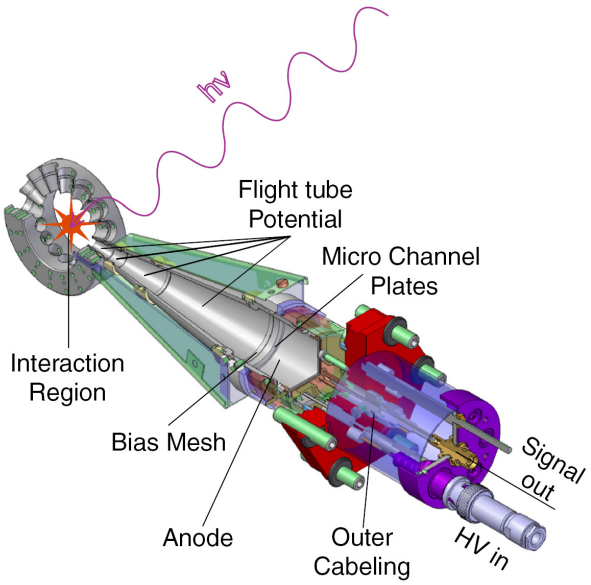

Figure 3.3: Schematic of a single spectrometer as it is applied to the setup introduced below. All relevant parts of the spectrometer as well as the spectrometer holding aluminum ring around the interaction region are labeled.

dedications to angular distribution non-dipole and electron-electron coincidence studies will be discussed in the following chapter.

3.1.1 The newly developed ARPES Spectrometer

The main factors for the development of a new MCP based electron time-of-flight spectrometer setup during the last years were high efficiency and a maximum versatility in terms of beam diagnostics. This also enables the use as a tool for online diagnosis (see chapter 3.1.6) benefiting from the fast acquisition of electron time-of-flight spectra. The newly developed setup allows the recording of very dense data sets of electron angular distributions in broad photon energy ranges even in regions of very small target cross sections in the order of few *kb*. Due to the redundancy of the spectrometers' angle positions in respect to the plane of incident light polarization in combination with the high efficiency of each spectrometer a very accurate determination of electron angular distributions is possible. This efficiency also enables fast electron-electron coincidence measurements as it is discussed later in this section.

High accuracy in combination with a fast data acquisition is not only essential to tackle problems of interest in atomic and molecular photoionization, but also

for improving the quality of existing literature values as they are e.g. important for transmission and energy calibration of the spectrometers (see chapter 3.1.3). They furthermore lay the basis for FEL based PES experiments which aim to study non-linear effects and therefore rely on an accurate reference in order to be able to discriminate the effects of interest.

One concern of AMO photoionization recently studied are Young type two center interferences. Using our newly developed setup we were able to study these interference effects in the valence photoionization of homonuclear diatomic molecules (see chapter 4). Since the partial photoionization cross sections of this work's relevant orbitals decrease rapidly for photon energies hundreds of eV beyond the individual ionization thresholds, it is an experimental challenge to record electron angular distribution data over such wide photon energy ranges with still high statistical certainty. This highlights the fact that the efficiency of the newly developed spectrometer setup is an important basis of this work.

Setup details - The way from electron emission to its detection

In detail the spectrometer setup consists of 16 independently working electron time-of-flight spectrometers aligned perpendicular to the plane of light polarization. The acceptance angle for each spectrometer is about 0.2% of 4π which leads to a total setup acceptance angle of 3.6% of 4π. This configuration was chosen to be the best compromise concerning the transmission in terms of the solid state acceptance angle, the need of a compact size for the beamline implementation as an online diagnosis tool, the achievable energy resolution and recovery and the capability of fast electron-electron coincidence measurements. For the latter use it is crucial to have a high number of spectrometer pairs at different angular positions.

Each spectrometer is mounted in a gold coated aluminum ring which can additionally be set to an independent potential (see figure 3.3). The gold coating was adapted during the development of the spectrometer setup making sure that no artificial charge effects can affect the electronic trajectories. With the independent potential on the inner ring a rejection of attracted ions can be achieved being relevant especially for high voltage retarding.

In the actual status, a single spectrometer consists of a flight tube divided in four independent potential sections, a 'micro channel plate' (MCP) based de-

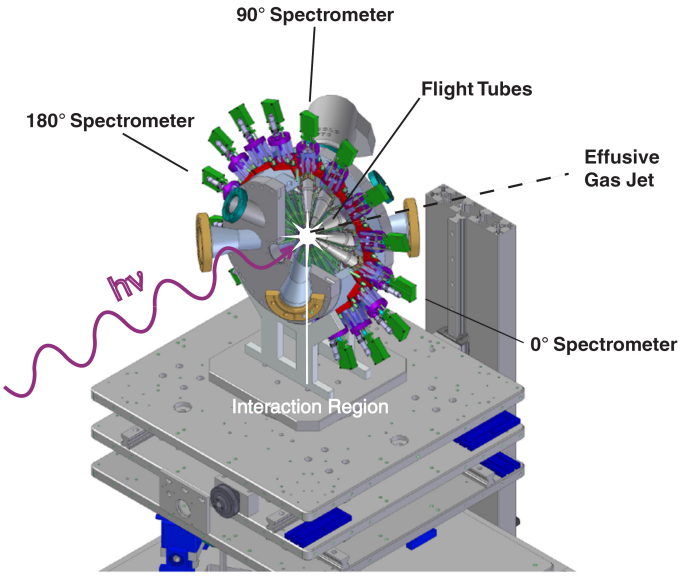

Figure 3.4: Schematic of the ARPES setup including all 16 time-of-flight spectrometers aligned around the dipole plane of the light polarization mounted on the moveable base platform (see itemization below and figure 3.3 for details).

tector and the relevant cabling for applying high voltages and decoupling the electronic signal. The total length from the interaction region to the MCPs is $\sim 140\,mm$. The separate flight tube potentials allow to shape the electron trajectories while decelerating the electrons in order to improve the energy resolution and transmission efficiency for higher kinetic energies. Extensive simulations in 'Simion'[2] have been performed in our workgroup and in collaboration with the diagnostic group of the European XFEL GmbH[3].
Figure 3.5 shows graphics created with Simion illustrating the differences of the electron propagations through the flight tube between a non-optimized and an optimized set of potentials. This visualizes implicitly the great need of a systematic understanding of electron optics using such a spectrometer setup as the presented. Experimental data on the topic of electron optical optimization has been acquired during several beamtimes to validate the simulations and further improve the spectrometers' resolution and efficiency. Due to the multi-parameter problem associated with the optimization, the development is still in progress being also highly relevant for hard X-ray and free-electron-laser adaptability. As

[2]Simion - Charged particle optics simulation software www.simion.com. Used Version 8.0.1.
[3]WP 74 diagnostic group, Jan Grünert. (jan.gruenert@xfel.eu) Adress: Albert-Einstein-Ring 19, 22761 Hamburg (Germany)

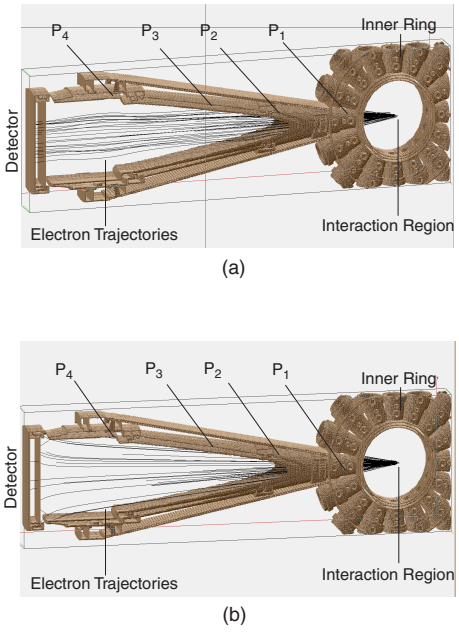

Figure 3.5: Simulated electron trajectories in the actual spectrometer design with an empirically determined flight tube potential optimization for an electron kinetic energy of $E_{kin} = 105\ eV$ and a retarding set of $P_1 = 50\ V$, $P_2 = 65\ V$, $P_3 = 88\ V, P_4 = 100\ V$ (a) and electron trajectories for $E_{kin} = 105\ eV$ without any potentials applied to the the flight tube sections (b).

shown in figure 3.5 one aim of a potential optimization is to form the electron trajectories in a way that they expose the whole active area of the MCPs accompanying the lowest possible time-of-flight differences. Such a widely spread electron exposure of the MCP ensures a low probability for an incoming electron to hit a single pore twice which would cause a lack of transmission. In addition, the charge recovery time can be improved by utilizing 'Extended dynamic range' MCPs. However, the benefit and the need for these special MCPs has to be evaluated in the light of much higher costs especially relevant for multi-spectrometer setups like the presented. This consideration is especially essential for an use of a MCP based spectrometer setup at free-electron-lasers due to the much higher amount of electrons exposing the MCPs within a very short time therefore increasing the probability of such a described 'double hit' of a single pore within the recovery time. Such effects can approximately be neglected for the use at a storage ring based synchrotron radiation source. However, the setup in its use as a diagnostic tool could benefit from longer life times of such special MCPs in comparison to the presently chosen detection quality MCPs.

Having passed the flight tube, the electrons are transmitted through a bias mesh[4] at the same potential as the last section of the flight tube. This ensures that in

[4] Transmission rate typically $> 85\%$

every potential setup the incoming electrons have a certain kinetic energy when they finally hit a z-stack of micro channel plates. The applied detection-quality MCPs have an opening ratio of 60% with a pore size of 12 μm. Detection quality MCPs do not provide further spatial resolution, since this is not essential for the spectrometer setup used here. Each MCP multiplies an incoming electron roughly by a factor of 1000. The applied high voltages at the MCPs are optimized for electronic saturation in the last plate which is depending on the actual charge status and the resistance of the plate.
The electron avalanche created by the MCPs is decoupled by a foil capacitor on a gold coated anode. The typical MCP pulses have a width smaller than $1ns$ (full width at half maximum (FWHM)) with an amplitude ranging from few mV up to 100 mV depending on the individual MCP charge status. Especially for free-electron-laser application it is crucial that the MCP pulses are very sharp in order to measure in analogous mode where the energy resolution is depending on the MCP pulse width (see section 3.1.5).

All cabling for the flight tube and the MCPs were equipped with additional RC-elements to reduce noise and artificial pulse reflections. All parts of each detector were under continuous development during the last years to increase the performance of the spectrometer setup. The peripherals of the setup as well as the whole chamber are carefully selected to be non-magnetic.

The whole ARPES TOF setup includes the following elements:

- A base platform being able to align the chamber in all degrees of freedom via step motors.
- A differential pumping section with an array of capillaries to ensure a pressure decoupling of the chamber from the beamline in the order of one to two pressure magnitudes.
- Two molecular turbo pumps with a pump capacity of 80 l each flange-mounted at the chamber. These pumps ensure the required basic pressure in the UHV. Typically pressures in the order of $10^{-9} hPa$ are reached.
- Three Helmholtz Coils for magnetic field compensation ensuring a homogeneous magnetic field of at least $10 * 10 * 10\ cm^3$ around the interaction region in the center of the chamber.

- A negative length flange ranging close to the interaction region. A magnetometer can be inserted for magnetic field measurements near the interaction region in order to monitor the effect of the Helmholtz correction coils.
- A $\sim 45^{\circ}$ horizontally rotated diode working as a beam dump which prevents light reflections at all photon energies and also allowing a chamber alignment as well as photon intensity monitoring via current measurements at this diode.
- A gas inlet system consisting of an x/y/z movable gas nozzle, a system of pressure regulators and the gases of interest. For the presented data of N_2 and O_2 as well as for the calibration rare gases the gas purity was 99.999% and for CH_4 it was 99.9%.

Non-dipole parameter determination

As already described in the previous chapter, there is a high scientific interest in electron angular distribution non-dipole effects [56, 60, 130]. The spectrometer setup on purpose has no spectrometers aligned off the dipole plane in the presented status, because for its use as a diagnostic tool it is advantageous to limit the required set of parameters to dipole contributions. Recalling equation 2.18 and figure 2.10, this means that all spectrometers in the dipole plane have an azimuthal angle $\Phi = 90^{\circ}$. There are small changes necessary to realize non-dipole adaptability. One possibility is to add some additional spectrometers off the dipole plane at flange angular positions containing non-dipole information. The advantage of such a solution is the minimal impact on its present design, whereas the disadvantage is the relatively low quantity of non-dipole angular information since the presented setup only allows additional mounting of four to six *'off-dipole-plane-spectrometers'*. Especially with the aim of high precision non-dipole spectrometry this solution can only be regarded to be preliminary (see also chapter 6). The other possibility is to rotate the whole chamber by 90° perpendicular to the direction of light propagation, so the number of non-dipole spectrometers is higher. Using this setup rotation for non-dipole investigations includes the removal of the spectrometers at the former angle positions 90° and 270° (see figure 3.4 for angle positions) so the synchrotron light can propagate through these former detector flanges. Both solutions are planned for non-dipole studies in the very near future as it can also be read in the outlook of this work.

Electron-electron coincidence measurements

The spectrometer setup as well as the utilized acquisition software can also be used for studies of electron-electron coincidences. In coincidence studies physical information can be determined, if two detected electrons are originated from the same physical process as it is the case for e.g. double ionization of the gas target. The sum of the electron kinetic energies of one double ionization process is according to the discrete binding energy of the doubly charged state fixed whereas the kinetic energy of the two electrons emitted may be a continuous distribution.The distribution limits are given by the fact that the sum of the two kinetic energies is fixed by the difference of the photon energy minus the binding energy of the doubly charged state. Access to this information provides great opportunities e.g. in double photoionization studies and sub-natural line width investigations. In the context of this work double ionization dynamics of homonuclear diatomic molecules such as N_2 or O_2 should include higher differential information on interference effects like the Cohen-Fano oscillations being main part of this thesis.

Coincidence spectroscopy is essentially dependent on a large solid acceptance angle of the spectrometers in order to achieve reasonable recording times for coincidence spectra. The required high solid acceptance angle is in contrast to a high angular resolution also essential for the use of the spectrometer setup. This experimental issue is solved by the large number of spectrometers implemented in the setup as it has been proposed by Viefhaus (1997) [135]. The large number of individual analyzers as well as the high solid acceptance angle of the presented spectrometer setup are outstandingly advantageous in this concern allowing very fast coincidence data recording.

As the setup utilizes a pulsed photon source anyway, the only additionally needed hardware is a 'time stamp generator' which numerates each acquisition cycle and is triggered by the bunch marker signal. Identifying a coincident electron-electron event can be done by software whenever two (or more) spectrometers detect an event within a given acquisition cycle. This identification is done via the unique 'time stamp'-number. The resulting data point contains the time-of-flight information of both detected electrons in a matrix illustration as it is shown in figure 3.6.

The maps in figure 3.6 show the electron-electron coincidence time-of-flight

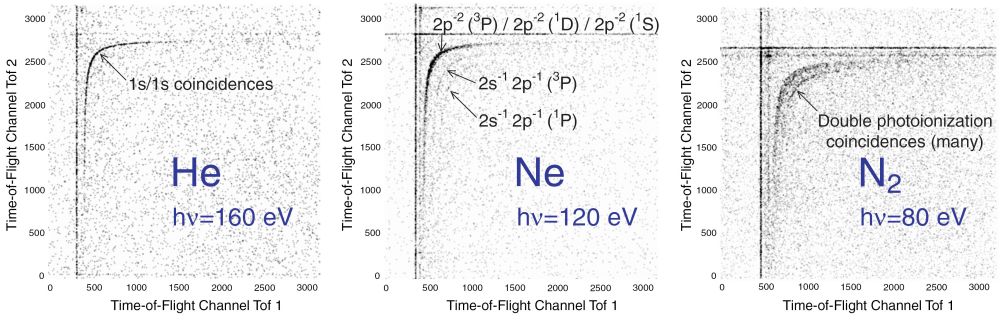

Figure 3.6: Elecion raw data for electron-electron coincidences of helium, neon and nitrogen at different photon energies above the respective double ionization thresholds.

spectra for two different analyzers at certain angle positions and three different targets (He, Ne and N_2). The designation of the resolved lines to the underlying physical process is also given in the figure. Since the helium atom contains only two electrons, there is only one possible double ionization state and its corresponding distribution. For neon the spectrum becomes more complex as it described in detail in figure 3.6 as a showcase. For nitrogen molecule fragmentation has additionally to be considered. Therefore, many possible double ionization channels are resolved in the spectrum. The horizontal and the vertical lines are artificial coincidences at the respective time-of-flights of the non-coincident electron lines due to random coincidences in the corresponding analyzer. The dots all over the matrix are random coincidences due to noise or background signal. The physically interesting signatures are the sickle shaped lines containing the information about the respective double ionization processes. This sickle structure is caused by the kinetic energy distribution of the participating electrons having a hyperbolic shape as the time-of-flight is inversely proportional to the square root of the kinetic energy for both electrons (see figure 3.12 in section 3.1.4). After a time-to-energy conversion for both detectors this sickle shape accordingly becomes a diagonal linear shape. Further detail on this processing can be read in e.g. Viefhaus (1997) [135]. This work only initializes electron-electron coincidence studies with much higher efficiency compared to previously utilized setups and further engagement using the presented spectrometer setup will come up in the near future.

A complementary experiment of the Fritz-Haber-Institut, Berlin

A complementary experiment on the topic of two-center interference effects has been carried out in collaboration with the Fritz-Haber-Institut (FHI) of the Max Planck Society in Berlin at the BESSY II storage ring of the Helmholtz Zentrum Berlin (HZB). The setup of the FHI consists of 22 working time-of-flight detectors also aligned perpendicular to the plane of light polarization. The flight tubes of the detectors are 309 mm long which corresponds to a better energy resolution but also a lower solid acceptance angle in comparison to the above presented spectrometer setup. The data acquisition is similar to the description in section 3.1.2. The most obvious benefit for the work presented in this thesis is an independent experiment with likewise independent analysis allowing a cross check of the data sets' accuracy. Therefore, the FHI experiment serves as a benchmark for this work. One has to bear in mind that the data presented in this thesis being recorded with our setup at DORIS III at DESY in Hamburg are representing a huge quantitative expansion of the acquired electron angular distribution data taken in Berlin at BESSY II.

3.1.2 Data Acquisition

The data acquisition is shown in a figure 3.7 visualizing the signal path beginning from the electron avalanche pulse created in the MCPs to the event file stored on a PC. The data file includes all relevant information namely the spectra recording time, the photon energy and the respective number of counted electrons labeled for each timing channel. In coincidence mode all electron-electron coincidences can be derived from the created binary event file.

Starting from the beginning, the MCP pulse is amplified by a wide band preamplifier with a working range from 0.1 to 1000 MHz and an amplification factor of typically 20. The amplified pulse is then discriminated by a constant fraction discriminator (CFD). Threshold, outgoing NIM-type pulse[5] width and a so called zero-crossing parameter are optimized for a high signal-to-noise level. An appropriate outgoing pulse width in the order of 50 ns is set and a proper edge triggering of the original pulse is accounted for a common NIM pulse height of $\sim 800\ mV$. A typical dark count level ranges in the order from 1 to 10 Hz per detector.

[5]The **N**uclear **I**nstrumentation **M**odule standard is a standard for negative logic signals.

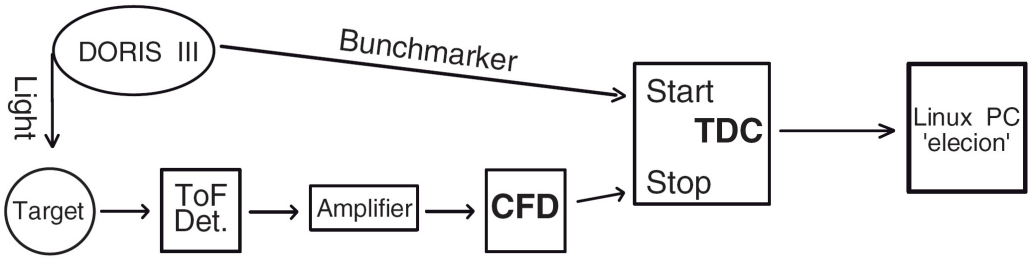

Figure 3.7: The scheme illustrates the signal processing from the target ionization via synchrotron radiation to the resulting photoelectron time-of-flight spectra. The time-to-digital converter (TDC) is triggered by a bunch marker provided by the facility. Then the TDC is assorting the incoming discriminated detector signals to 60 ps timing segments. Finally the acquisition software uses the TDC information for generating histograms in the form event per timing channel.

The next step of processing is a time-to-digital converter (TDC) being in simple words the high precision stop watch responsible for the determination of the time-of-flight and the counting of the incoming pulses. In this case a device with a time resolution of 60 ps is utilized [133]. The essential advantage in comparison to other digitizing hardware like e.g. standard analog-to-digital converter (ADC) is that a TDC has a very short 'dead time' usually limited by the pulse width adjusted at the CFD. This pulse width was usually adjusted to be $\sim$ 50 ns for all detected events during all relevant beamtimes. Compared to Flash ADC or oscilloscopes however, the time resolution of the TDC is superior. It corresponds to 16 $\frac{GS}{s}$ sampling speed which is at present only available for high-end oscilloscopes having - for this multi spectrometer setup utilization - a prohibitive price tag. In non-coincidence mode the TDC measurement is started by a NIM pulse provided by a phase stable timing signal having the same time period as the charged particle bunch circulating in the storage ring (so called bunch marker). Due to technical constraints within the TDC a minimum timing cycle of 1 μs is required. Because of the revolution time at DORIS III (see section 3.2) of 964 ns the TDC is operated using only every second bunch marker as a start signal. This corresponds to a usual timing cycle of about 2 μs which is used for most of the data presented in chapter 4. Therefore, in DORIS III 5 bunch operation mode 10 spectra with $\sim$ 32000 channels, each with the mentioned 60 ps, are plotted in a live histogram while recording the data. The data of the TDC is transmitted to a Linux computer via a parallel interface using SCSI-type connectors.
The acquisition software 'elecion' [143] displays the time-of-flight spectra in real

time where each event represents one count a a given time-of-flight. The binary mode of detection in terms of discrete counting for each event is common for a use of such an gas phase experiment at a storage ring based light source where typically only few or even less than one event is detected per acquisition cycle. This differs from a use of such a spectrometer setup at an FEL since there the amount of incoming electrons is so high that an analogous measurement of the MCPs is necessary (see section 3.1.5).

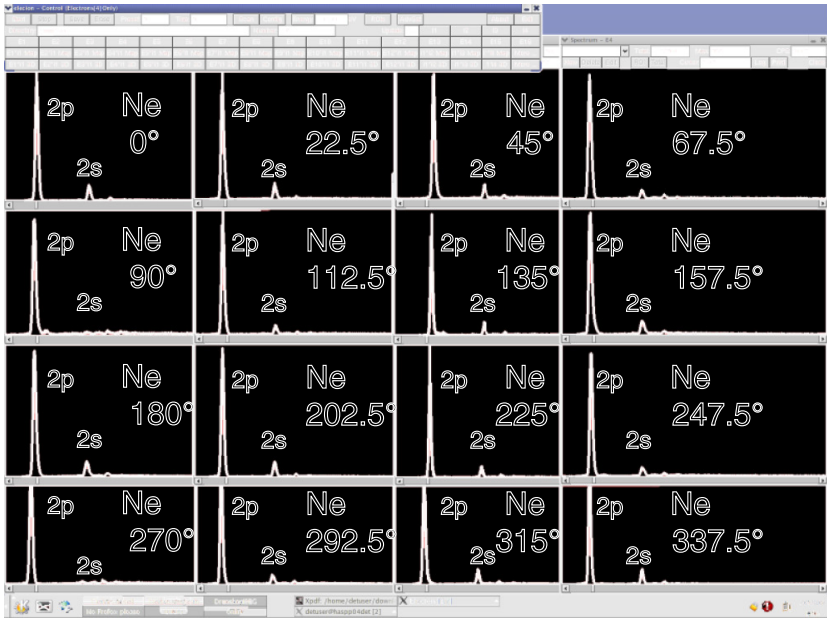

Figure 3.8: Screenshot of the data acquisition software 'elecion' showing time-of-flight spectra for all 16 spectrometers. In this example the histograms show neon time-of-flight spectra at a photon energy of 60 eV. The effect of the angular distribution parameter for the Ne 2s line ($\beta = 2$) can nicely be seen by the virtual absence of signals in the 90° and the 270° spectrometers and a progressively higher signal towards 0° and 180° respectively.

3.1.3 Calibration Properties

Although all detectors are assembled in the same way and all parts are equally manufactured, each of the spectrometers has a slightly different behavior concerning efficiency, transmission and resolution. According to the Legendre polynomial for differential cross sections (section 2.4 equation 2.17) a literature database of a well investigated angular distribution of a calibration target is needed for all determinations of unknown angular distribution parameters β. Having access to

these known angular distributions an intensity normalization of the spectrometers can be performed and then be used for the analysis of unknown angular distributions. For this process it is common to use electrons of the helium $1s$ ([89] and references therein), the argon $3p$ [1, 37, 61, 119] or the neon $2p$ line [68, 76, 119, 148] depending on the photon energy range of interest. For higher photon energies further electron lines of deeper lying orbitals with higher binding energies and accordingly higher cross sections can be taken into account. However, there is much less angular distribution data available for inner shell photoionization over wide photon energy ranges. The establishment of a proper data base is a necessary task which is an ongoing project of the P04 workgroup.

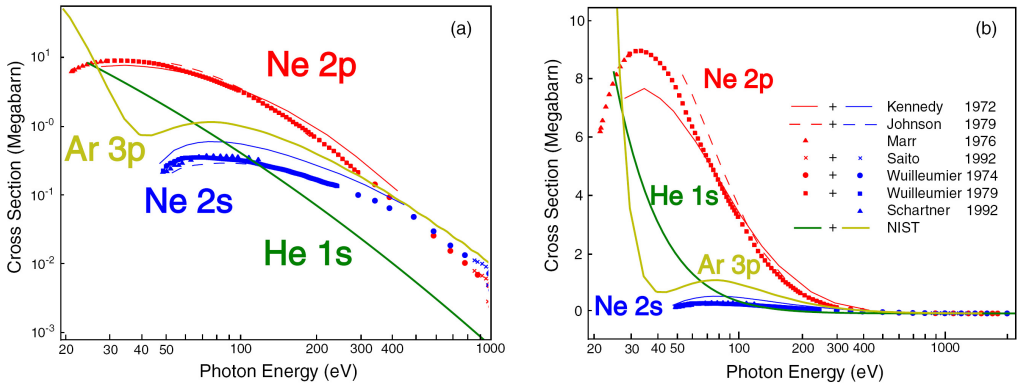

Figure 3.9: Figure (a) shows available partial cross section data (as cited in (b)) for several noble gas electron states in a log-log plot. Figure (b) shows the same data over a broader photon energy range with an allocation of all symbols and lines used for the literature values of Kennedy *et al.* [68], Marr and West [142], Johnson *et al.* [64], Saito, Wuilleumier *et al.* [147, 148] , Schartner *et al.* [114] and NIST [95].

Available cross section data for He $1s$, Ne $2p$, Ne $2s$ and Ar $3p$ is plotted in figure 3.9, since angular distribution as well as partial cross section data for these states is relevant concerning calibration properties in the frame of this work. Figure 3.9(a) shows a log plot in both dimensions to increase the visibility of low photon energy and low cross section regions. The plot on the right side (b) shows the same data with a mapping of the applied literature values. It can be derived from the figure that for investigations over broad photon energy ranges up to $\sim 400\ eV$, neon is most suitable for calibration usage concerning the high cross section.

The basis for a highly precise determination of β is the validity of the calibration data sets of a known angular distribution for gas target orbitals since their quality directly scales to the accuracy of β-investigations. Due to its comparably high cross section and an established theoretical and experimental β-data base over a wide photon energy range, the neon $2p$ electron line is a preferred choice for investigations in the soft X-ray photon energy regime usually better suited than the helium $1s$ or the argon $3p$ lines. Beside this, Ne $2p$ data can intrinsically be cross validated for photon energies > 49 eV by calibrating the Ne $2p$ line with the Ne $2s$ electron line ($\beta = 2$) and furthermore with several well investigated satellite lines [55, 74] of even higher binding energies.
Nevertheless, an advantage of a spectrometer calibration via helium $1s$ electron angular distribution is the well defined β of $+2$ (in case of 100% horizontally polarized photons, as there is neither theoretical nor experimental observations available which deviates from this value [89]). Especially for He $1s$ the influence of scattering on other electron orbitals can approximately be neglected. A disadvantage is the vanishing signal of the He $1s$ line in spectrometers aligned perpendicular to the plane of light polarization and a resulting loss of accuracy in spectrometers close to this angle. Furthermore, helium has a rapidly decreasing cross section (see figure 3.9) causing a comparably unefficient calibration for higher photon energies ≥ 200 eV.

Argon $3p$ electrons have an angular distribution unequal to 2 and its cross section is higher in comparison to helium 1s but still lower than the cross section for the neon $2p$ photoionization which is shown in figure 3.9. Beside a higher photoionization cross section compared to helium 1s, an intrinsic cross check due to a more complex spectrum with additional main quantum states can be performed as it was the case for neon. The most important fact is that well established literature values for the angular distribution of Ar $3p$ is available as it is the case for Ne $2p$ ([8] and references therein as e.g. [1, 37, 61, 119]).
An increase of accuracy for β-investigations can be afforded by using these independent calibration targets. The disadvantage of such a redundant calibration is a much higher time effort being in contradiction to the short beamtime periods available. Another apparent possibility of gaining accuracy in this respect is a quality increase of the existing β-datasets in terms of the available photon energy range, the data accuracy and a more dense photon energy step width. The latter parameter is especially important, since many resonance features can affect the

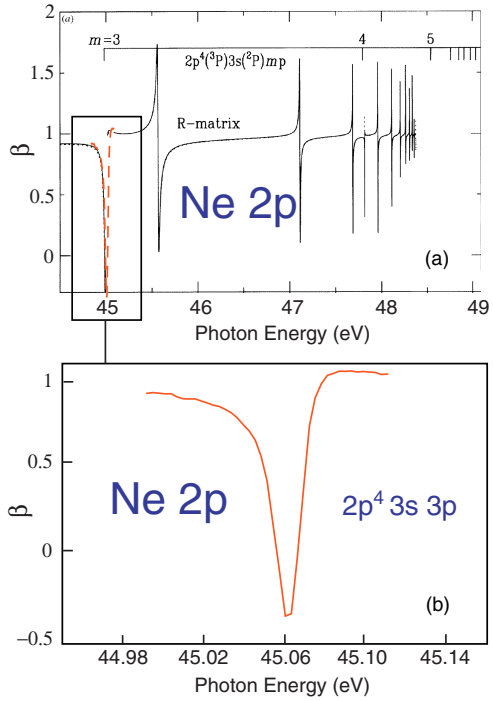

Figure 3.10: Figure (a) is adapted from Langer *et al.* (1997) [76] showing theoretical calculations for neon $2s \rightarrow 2p$ autoionization resonances of the angular distribution parameter β below the Ne $2s$ threshold. The red dashed line at the $2p^4$ $3s$ $3p$ resonance shows the experimental data of this thesis. Figure (b) shows a zoom in this experimental data of the $2p^4$ $3s$ $3p$ resonance.

angular distribution sometimes even massively within very small photon energy ranges in the order of meV. One example of such a resonance influence is shown in figure 3.10. This autoionization resonance is not included in the common calibration data and may affect β-investigations significantly around the photon energy range of its occurrence at 45 eV. As it can also be seen in figure 3.10, much more resonances are to be taken into account in that particular photon energy range of neon. Resonance features are often occurring due to autoionization below the threshold of main quantum states and other transition channel openings. The situation is common to most gas phase targets as it is shown by similar features are discussed in chapter 4 for the angular distribution of N_2 and O_2.

Beside such resonant signatures which are not taken into account in the common calibration data for e.g. Ne $2p$, the literature values still show persisting discrepancies between experimental and theoretical data (see figure 3.11). Precise studies of small electron angular distribution effects requiring small errorbars (< 0.05 β) as it is the case for this work therefore raise the need of remedying these discrepancies in order to minimize the calibration induced uncertainties and in turn open up the possibility to study such effects for the first time.

Therefore, highly accurate and more dense experimental β-datasets than available

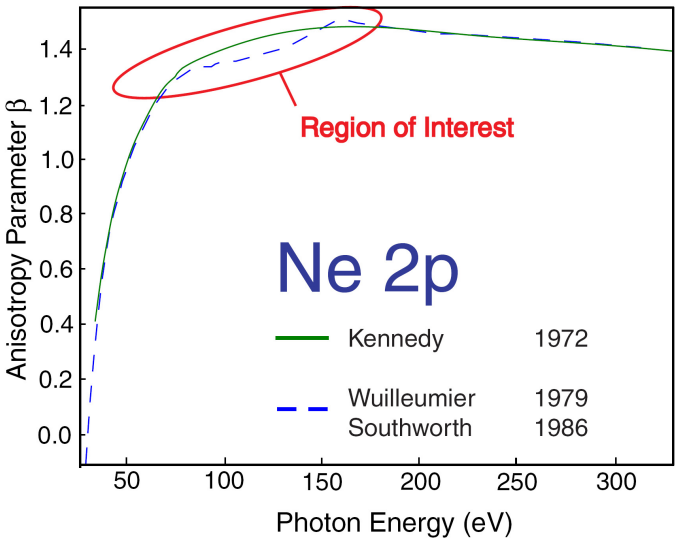

Figure 3.11: The figure illustrates the still persisting discrepancy of common experimental (Southworth *et al.* (1986) [119] and Wuilleumier *et al.* (1979) [148] and theoretical (Kennedy *et al.* (1972) [68]) data available for the angular distribution anisotropy parameter β of Ne $2p$ in the photon energy range from $\sim$ 70 to 210 eV.

are necessary. In order to achieve this aim, highly precise β-data for the Ne $2p$ line in the photon energy range from threshold up to 600 eV were recorded. The theoretical data of Kennedy (1972) [68] is widely supported by these new results not showing the depicted discrepancy as it is plotted in figure 3.11.

3.1.4 Data Processing

The data processing includes a stacking of the multiple spectra recorded with the TDC, a time to energy conversion of the spectra and an integration of the counts for all relevant electronic states. It is crucial to disentangle the actual photoelectron signal from the background. The background is not necessarily only noise, but can also be real electronic signal from comparable fast electrons like e.g. Auger or scattered electrons. For this reason, the resolution of the detector as well as a precise data analysis is important to determine accurate β-data.

As it can be derived from figure 3.12 to each channel a corresponding kinetic energy can be determined since the binding energy of the neon $2p$ electrons is well known. This can be illustrated in the simple calculation for each time-of-flight channel

$$E_{kin} = E_{h\nu} - E_{Binding\ Ne2p} \tag{3.1}$$

Every electron signature (usually using the center of mass of this signature) in a spectrum of interest after the calibration can then be determined to have a binding energy of

$$E_{Binding\ (channel)} = E_{h\nu} - E_{kin} \tag{3.2}$$

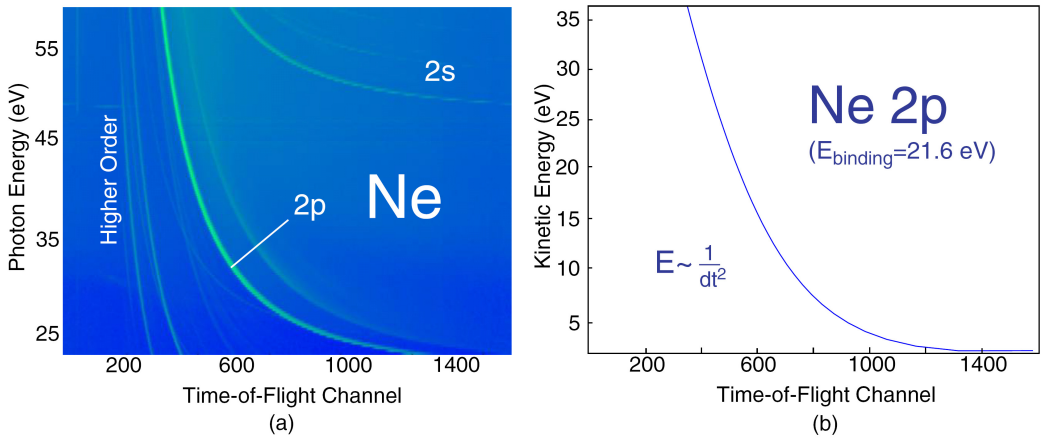

Figure 3.12: The false color plot (a) shows the variation of the time-of-flight of the electrons from 25 to 60 eV. The fit curve in figure (b) shows the channel position of the neon 2p electron line for certain electron kinetic energies.

This procedure is done prior and after every photon energy scan for a certain target in order to ensure proper calibration data with no artificial position changes or intensity fluctuations. As it can be seen in figure 3.12, the development of the channel position for an electron line over the photon energy is not linear. The development and therefore the conversion fit is based on the proportionality

$$E \sim \frac{1}{dt^2}. \tag{3.3}$$

and is applied to the spectrometric data to be converted.

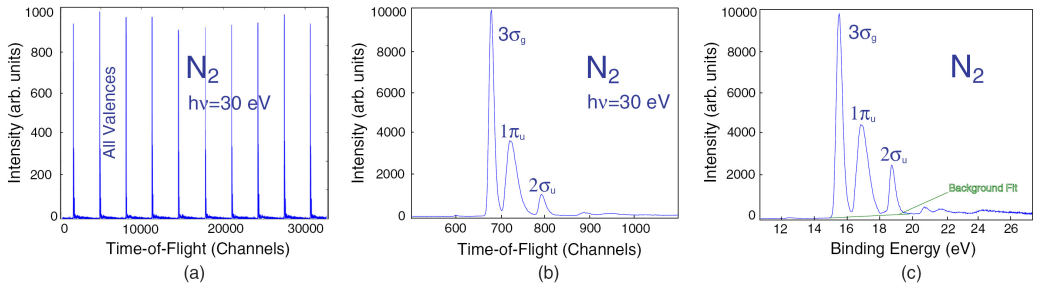

Figure 3.13: The figure shows (a) a raw electron time-of-flight spectrum as it was acquired by 'elecion' in DORIS III 5 bunch mode, (b) a stacked spectrum including all 10 spectra of (a) and (c) the stacked spectrum with converted energy information (time-to-energy-conversion) and background determination via linear fit.

Since the measured data for the target under study and also the calibration

targets is quantitatively very voluminous, the written code[6] is automatized in terms of calibration of the data, finding the relevant peaks in the spectra and analyzing them with the final output of a β-value. It can be chosen how many files should be analyzed, what kind of background fitting should be used and what calibration literature values are to be taken. This automatized processing raises the possibility of analyzing thousands of β-values in a broad energy range within a moderate time ($\sim$ 100 β-values per hour for 16 spectrometers and clearly resolved electron lines). As a future application, it is possible to adapt the code for an online processing of electron angular distribution data which allows to use the spectrometer setup for online diagnostics (see section 3.1.6).

3.1.5 Free-Electron-Laser Adaptability

The introduced spectrometer setup is not only suitable for synchrotron radiation experiments at storage rings, but also applicable to free-electron-lasers. Although the injected gas targets are very dilute, FEL pulses are that intense that even one single shot can be sufficient for the determination of an adequate electron time-of-flight spectrum. Integration over many shots is also possible and depending on the scientific topic expedient. The method allows e.g. the investigation of non-linear processes in the photoionization of atoms and molecules. An overview on this scientifically highly interesting topic can be found in e.g. Doumy *et al.* (2011) [41], Berrah *et al.* (2010) [12], Sorokin *et al.* (2007) [118] and references therein. As it will be pointed out in the following section, the scientifically relevant studies on electron angular distributions are additionally complemented by diagnostic scopes even for single shot analysis (see section 3.1.6). Beamtimes at the vacuum ultraviolet (VUV) FEL FLASH (Freie-Elektronen-Laser in Hamburg) at DESY have been carried out on the topic of non-linear processes in the photoionization of noble gases and small molecules in collaboration with the Fritz-Haber-Institute, using the long spectrometer setup briefly described in section 3.1.1. The corresponding results are not part of this work, but they clearly corroborate the fact that such a system is rather useful at FELs.

The use of MCP based time-of-flight spectrometers at FELs is different from the use at a storage ring based synchrotron radiation source. To recall, at a storage ring like DORIS III, roughly 5 million photon pulses are generated per second and the individual spectrometers are only measuring few events per pulse or less (see

[6] Programming language: 'Python' Version 2.5

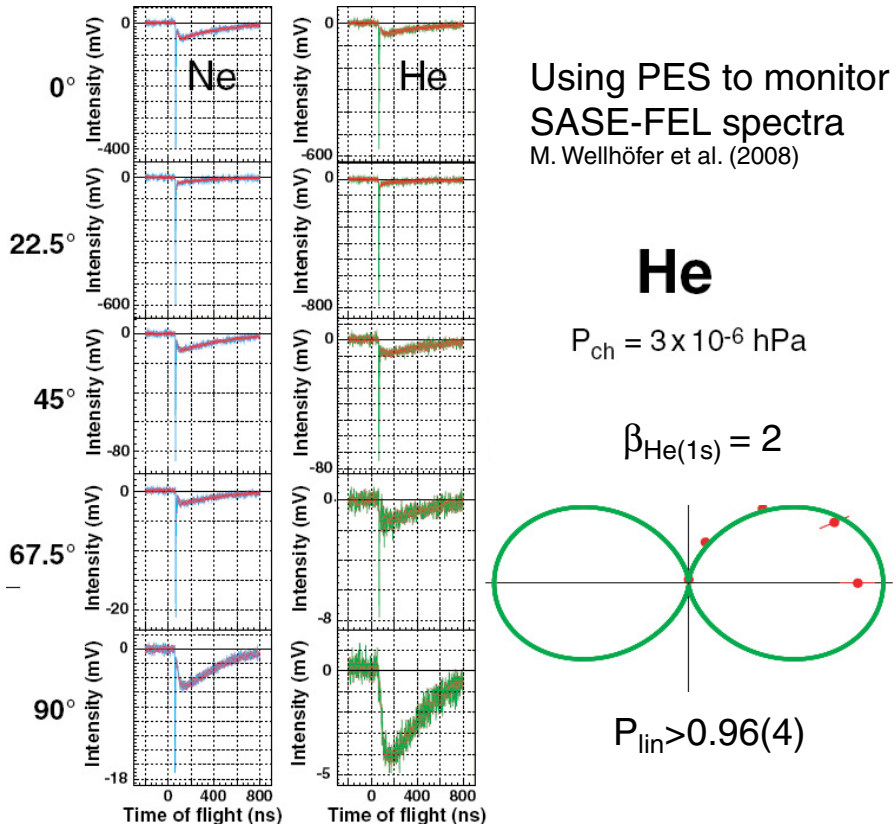

Figure 3.14: Single shot spectra for various spectrometer angle positions from 0° to 90° for neon and helium photoionization with free-electron-laser pulses of FLASH according to [140]. The inset on the right side of the figure shows the expected and the real angular distribution for the He $1s$ line indicating a photon polarization of $\geq 96\%$.

section 3.1.2). Regarding an FEL like FLASH, one can assume that one single pulse in the order of hundred femtoseconds or less contains the same amount of photons generated in one second at DORIS III[7]. Due to the massive amount of electrons created by the interaction of such an FEL pulse with the gaseous target, it becomes feasible to measure the current through the MCPs analogous using a fast digitizer with respect to the electron time-of-flight[8]. Since a MCP has a certain recovery time for their charge in the capillaries, one has to accurately tune the applied high voltage in order to ensure linear response also for following pulses.

The peaks in the spectra of figure 3.14 illustrate the angle dependent electron intensities at $h\nu = 47\ eV$ recorded with an early prototype of the present setup of this thesis. As it can be expected from literature, the helium $1s$ line shows a strong angular distribution anisotropy close to $\beta = 2$, whereas the neon $2p$ line indicates an electron angular distribution below $\beta = 2$. These spectra highlight the applicability of the presented method to FEL research on various topics [140].

A further test of the spectrometer principle was done in combination with an experiment at the Linac Coherent Light Source (LCLS) at SLAC in Stanford, California. The aim of the particular beamtime 'L333' under supervision of the 'Advanced Study Group' of the 'Center for Free-Electron Laser Science' (CFEL) in Hamburg was the investigation of surface dynamics of a CdTe crystal, using a pump-probe experiment at the XPP beamline of the LCLS. One of the three techniques applied for the investigations of the CdTe electron dynamics was a single electron time-of-flight spectrometer responsible for analyzing Auger electron energy shifts induced by the optical pump laser. A preparatory measurement of a CdTe crystal has been carried out at the P09 beamline of PETRA III in Hamburg with the experimental setup presented in section 3.1.1. It was the first time this spectrometer setup was used for solid state measurements. The principle benefit of a preparatory storage ring based investigation prior an FEL experiment is that an estimate of the expected spectra can be generated under very stable conditions.

In summary, MCP based time-of-flight detectors are applicable to FELs, being able to collect integrated or single shot spectra. Further engagement on this topic will follow in the near future.

[7] Due to the much lower pulse repetition rate the average amount of photons is similar.

[8] For our measurements we used 8 GS 'Acqiris' hardware (DC 282) from Agilent Technologies [127].

3.1.6 Online Diagnosis

Originally the described spectrometer was developed for beam diagnostics at the P04 beamline at PETRA III at DESY in Hamburg. This is a coexisting use beside the scientific assignment of high precision angle resolving photoelectron spectroscopy. In this section an overview on the diagnostic relevancies will be given to underline the versatility of the spectrometer and to motivate further engagements in hard X-ray spectroscopy and FEL diagnosis.

The spectrometer is capable of determining several essential photon beam parameters online. That means due to the very dilute gas target in the order of $10^{-5}\ hPa - 10^{-7}\ hPa$ the photon beam is almost unaffected by passing through this gas target. Despite the low target density the photoionization rate of the gas target is sufficient for a very fast analysis of electron angular distributions.

The accessible photon beam parameters are

- Photon beam position (Accuracy $\leq 10\mu m$),
- Photon energy (Calibration should be $\frac{dE}{E} \leq \frac{1}{10000}$),
- Photon flux (Accuracy $\leq 1\%$ absolute, $\leq 0.1\%$ relative),
- Degree of polarization (Accuracy $\leq 1\%$).

The beam position can be determined most accurately analyzing a low kinetic energy electron peak. If the beam position changes e.g. in a horizontal direction, the measured time-of-flight of the electrons changes most significantly in the horizontally aligned detectors. One of them measures a shorter and the opposite one a longer time-of-flight. Explicitly, this means that the channel position of the peak is changing respectively. Applying a sophisticated analysis for the center of gravity of the relevant peak, it is possible to determine beam positioning changes way below $10\mu m$. The large number of independent spectrometers result in a high accuracy due to redundantly collected data on different angle positions. First tests moving the chamber with respect to the beam position turned out to be very promising (see figure 3.15).

The photon energy can be determined in a quite similar way, again analyzing the channel position of the relevant electron peak in the time-of-flight spectra. Varying the photon energy shifts the peak to lower or higher channel numbers

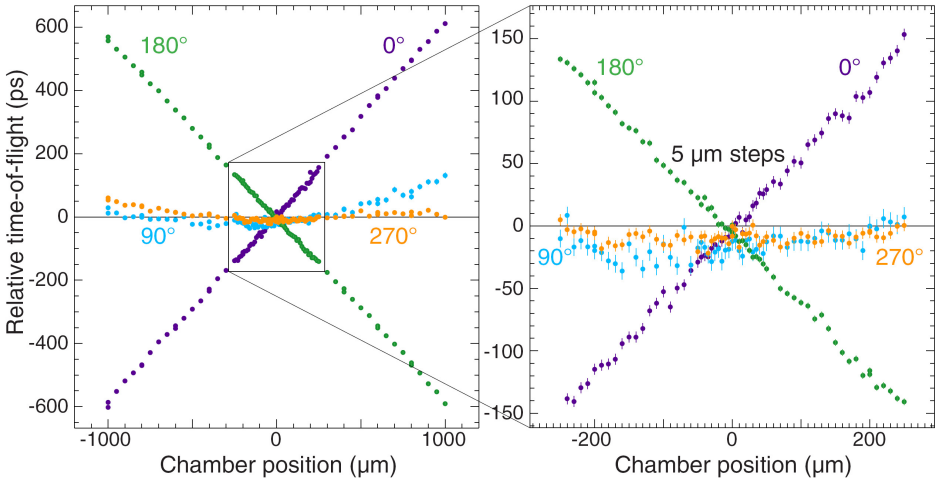

Figure 3.15: The figures provided by [136] show the relative time-of-flight of Ne $2p$ electrons at $h\nu = 25\ eV$ for the horizontally (0° and 180°) and the vertically (90° and 270°) aligned spectrometers of the experimental setup. On the left side a chamber movement of 2 mm with an outer step width of 50 μm is shown whereas on the left side a zoom in the inner positioning range of 0.5 mm is shown with a step width of 5 μm. The changes of the relative time-of-flight in the vertically aligned detectors are probably caused by a parasitic movement of the chamber.

respectively.

The photon flux can be determined relatively, using the count rate of the spectrometers normalized by tabulated cross sections and afterwards generating an absolute scale using a diode as well as a photoionization cell.

The photon polarization analysis is using the angle dependent intensities detected by all of the spectrometers together with a tabulated angular distribution to determine the degree of photon polarization. In photon energy ranges where a single s-orbital signature can be used for such a determination, this procedure is straight forward. At the vertical positions with respect to the plane of polarization no signal would be measured for the case of 100% linearly polarized light. Changes in the plane of polarization also shifts the maxima and the minima of the angular distribution as it is illustrated in figure 3.16. During the work on this thesis an algorithm was written which enables to automatically find the relevant electron lines, analyze their intensity and determine changes in the photon polarization. An example of such an analyzis can be seen in the figure 3.16. Although absolute polarization values can only be determined for the case where the angular distri-

bution is known, it is possible to determine relative changes for any electron line including the information on the angular position of the polarization plane. This is especially useful for photon energy regions where no literature data is available.

The P04 beamline at PETRA III at DESY in Hamburg uses an APPLE II undulator (Advanced Planar Polarized Light Emitter) capable of producing linearly polarized light in all planes around the photon beam direction as well as circularly polarized light in the photon energy range from $200-3000\ eV$. The circular polarization mode is realized by longitudinal shifts of parts of the undulator's magnetic structure. Therefore, the diagnostic need of a polarization analysis to monitor the actual state and degree of polarization is obvious. There is one other beamline at PETRA III capable of polarization shifts namely the P09 beamline. The P09 beamline was one of the first working beamlines at PETRA III and already during the commissioning phase several beamtimes have been carried out to validate the online diagnostic abilities of the experimental setup in terms of polarization analysis. In the frame of a German-Russian collaboration a diagnostic unit, equal to the one described, will be implemented in this beamline adapted to the requirements of a higher photon energy range from $3-20\ keV$. The polarization shift at the P09 beamline is realized by two diamond phase plates being able to shift linearly as well as creating circularly polarized light. This setup was commissioned using our online diagnostic unit and a high precision diffractometer. Cross checking these values allowed a 'proof-of-principle' showcase for our spectrometer and also for the quarter wave plate setup at the P09 beamline[9].

The showcase in figure 3.16 illustrates the relative intensity development of $Xe\ 2s$ electron lines ($E_{binding} = 5453\ eV$) for all spectrometer angle positions for several shifted degrees of polarization 3.16. The relative intensity data for each spectrometer was fitted by using a sine function. Since the intensity distribution changes with a changing degree of light polarization the phase shift of this sine function directly indicates the angular position of the polarization plane. In this particular case a single s-orbital line was used with an implicit knowledge of the angular distribution. The agreement of the time-of-flight data and the data taken with a diffractometer is remarkably good underlining the accuracy of such an online diagnosis (See 'DESY Photon Science Highlights 2009' page 86.).
Regarding more complex cases and the polarization analysis for photon energy ranges of several keV it is anyway necessary to have access to well established

[9]P09 beamline scientist in charge: Jörg Strempfer jörg.strempfer@desy.de

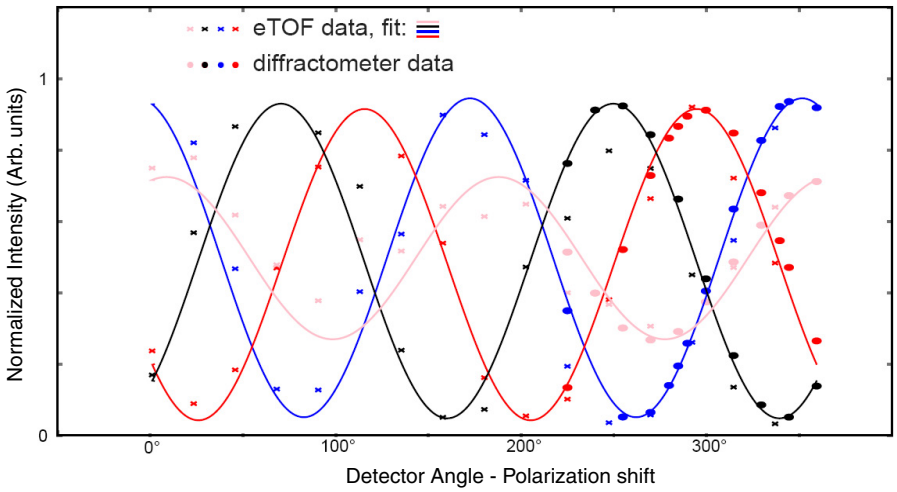

Figure 3.16: The figure shows relative $Xe\ 2s$ intensities at $h\nu = 5600\ eV$ for all working electron time-of-flight spectrometers of the presented experimental setup (crosses) and sine fits through the associated data points. Each fit represents a shifted degree of photon beam polarization. The full circles show data recorded with a diffractometer analyzing Bragg peaks of a crystal target over 140° provided by the P09 workgroup.

databases for different target's angular distributions in order to ensure the determinability of absolute degrees of light polarization. The task of creating appropriate β-databases including all relevant angular distribution informations for several atomic and molecular gas targets in a photon energy range from 250 to 3000 eV will be realized during the next years at the P04 beamline. In order to achieve these aimed databases the retarding potentials of the spectrometers have to work properly up to 3000 V to ensure a sufficient energy resolution recovery over the whole working range of the beamline. The first proof of principle experiment employing retardation up to 3000 V was accomplished during a beamtime at the P09 beamline in August 2011. This stimulated interest for an adaptation of such a spectrometer setup, not only for the P09 beamline, but also for the European XFEL GmbH (WP 74 see contact above).

During the beamtimes at the P09 beamline we were able to show the general usefulness of the applied method to the hard X-ray regime up to $\sim 15\ keV$ as it is shown in figure 3.17. This preliminary upper limit was caused by the beamline performance at the time of the investigations so the method is promising for even higher photon energies. These data and the data presented above were the very first 'proves-of-principle' for an applicability of such a spectrometer setup in the

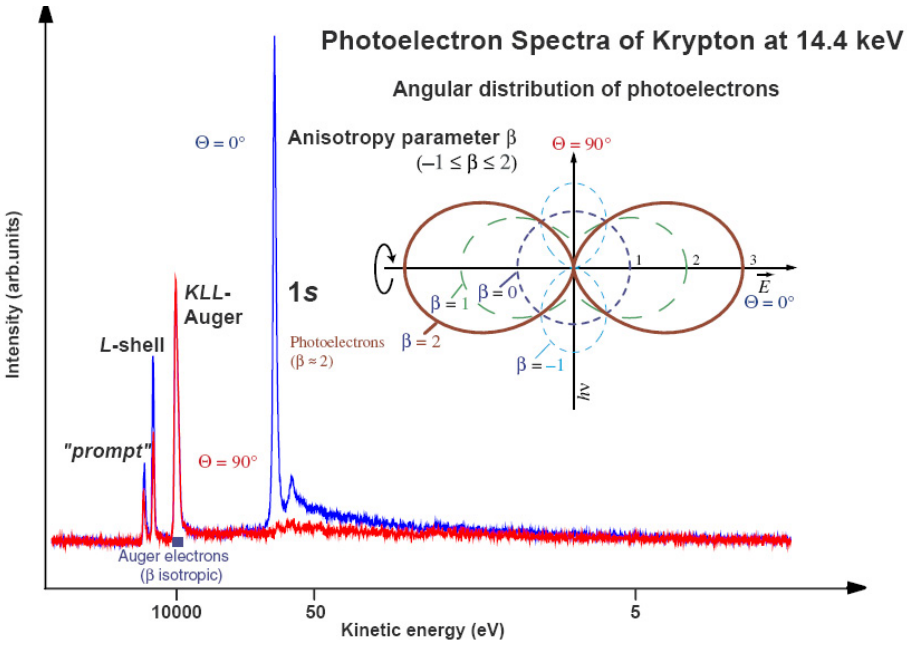

Figure 3.17: Photoelectron time-of-flight spectra for Krypton photoionization at 14.4 keV for the 0° (blue line) and the 90° (red line) spectrometer. The spectra include the fluorescence photons ('prompt'), L-shell electrons, several KLL-Auger electrons and the Kr 1s electrons ($E_{binding\ 1s} = 14326\ eV$). The inset illustrates the corresponding electron angular distribution.

hard X-ray regime, being therefore essentially interesting also for synchrotron radiation and free-electron-laser hard X-ray beamlines.

Apart from polarization analysis, the other capabilities of the online diagnosis tool are also interesting for photon beam property analysis of free-electron-lasers both in the soft- as well as in the hard X-ray regime. The accessible parameters are the same as they have been presented above. The determination of photon energy, beam position and intensity, but also - especially interesting for SASE (self amplification by stimulated emission) type FELs - its energy spectrum are feasible. The diagnostics group of FLASH at DESY as well as the WP 74 diagnostic group of the European XFEL GmbH in Hamburg are collaborators on the topic of online diagnosis via electron (and ion) time-of-flight spectroscopy. Outside the scope of this thesis, a paper on the topic of photon energy measurements using ion time-of-flight spectrometry was published in collaboration with the workgroup of Kai Tiedke[10] [67].

[10]FLASH diagnostic group kai.tiedke@desy.de

3.2 The Light Sources and Beamlines

The radiation required for the investigations presented in this thesis needs to include an appropriate accessible photon energy range, high photon flux, a high degree of horizontal photon polarization and a pulsed structure for the time-of-flight determination of the emitted electrons. Therefore and as a brief introduction to this section the functionality of undulators will be introduced, since these insertion devices are best suited for such studies and all of the presented data in this thesis is measured at undulator based beamlines.
Undulators are 'third generation' synchrotron radiation light emitters for freely tunable photon energies within certain limits whereas bending magnets are the first and wigglers are the second generation. Undulators for the use at free-electron-lasers are based on the 'self amplification by stimulated emission' (SASE) principle commonly accounted to the fourth generation [73].
Basically synchrotron radiation is emitted by relativistic charged particles deflected by a magnetic field [116] which can basically be written as

$$\frac{d\vec{p}}{dt} = e\vec{v} \times \vec{B}. \tag{3.4}$$

A deflection of charged particles propagating almost at the speed of light through periodic magnetic structures with changing polarity leads to a stacking of the emitted light pulses. This principle is applied in a wiggler setup. If the magnetic periodic length of such a device is a multiple of the emission photon wavelength, constructive interference leads to distinct energy minima and maxima in the emitted light spectrum. This circumstance is exploited for undulators. The so called undulator parameter is given by

$$K = \frac{eB\lambda_m}{2\pi\beta_u m_e c} \tag{3.5}$$

where e is the electron (or positron) charge, B the magnetic field, λ is the magnetic field period, β_u is the ratio of actual velocity and the speed of light (c) and m_e is the electron mass. If $K \ll 1$ distinct minima and maxima are produced and the device can be characterized to be an undulator, whereas $K \gg 1$ results in a continuum emission spectrum as it is the case for a wiggler.

The BW3 beamline at DORIS III

Most of the data discussed in this thesis were collected at the BW3 beamline[11] at the DORIS III storage ring at DESY in Hamburg (Germany). The complementary experiment together with the FHI was carried out at the UE 56/2 PGM 1 beamline at BESSY II (HZB) in Berlin (Germany). As an outlook a short overview on the P04 beamline at PETRA III, also located at DESY in Hamburg, will be given.

The DORIS III storage ring was usually working in 5 bunch mode during most of the numerous beamtimes. The initial particle beam current was 140 mA decreasing during the injection cycle of commonly 6-8 hours to $\sim$ 80 mA. The positron beam energy of DORIS III is 4.45 GeV still allowing very low photon energy studies down to few eV at certain beamlines. In order to increase the lifetime and the stability of the charged particles in the storage ring DORIS III uses positrons instead of electrons. According to the circumference of close to 300 m and the positrons moving approximately at the speed of light the bunch spacing is roughly 200 ns in 5 bunch mode so the pulse repetition rate is $\sim$ 5 MHz. These machine properties, especially an appropriate positron bunch spacing in order to be able to record all electrons of one dedicated light pulse, were essential for carrying out the experiments presented in this work.

Since the investigations presented in this work are mainly dealing with soft X-ray studies covering wide photon energy ranges, the BW3 beamline at DORIS III was most suitable for this intent. The BW3 beamline is a state-of-the-art beamline covering the photon energy range from 15 to 1500 eV [34, 77, 91, 105]. Despite the long time ($\sim$ 20 years) it has already been working, the BW3 beamline is still highly competitive providing high photon flux over this comparably very broad photon energy range. The relevant parameters for this work are:

- A revolver type undulator with two interchangeable magnetic structures using different periods (21 and 44 periods) providing high photon flux in the order of $10^{12} \frac{photons}{s}$ over this wide photon energy range with the first undulator harmonic.
- An SX 700 plane grating monochromator with two exchangeable gratings.

[11] BW=**B**ypass **W**iggler. Note that despite this generic name the light source of this beamline is an undulator.

Grating 1 with 1200 $\frac{lines}{mm}$, grating 2 with 366 $\frac{lines}{mm}$. Both are gold coated. The photon energy resolution is given by $\Delta E[eV] = 2.16 * 10^{-4} * E * 1.5 * s$ where s is the slit width in mm [105].

- A photon beam spot size at the beamline focus of $100 * 200\ \mu m^2$ (with exit slit settings $< 100 \mu m$).
- An exit slit with an adjustable slit width ranging from few μm to 800 μm and
- Horizontally and vertically adjustable baffles for beam size and halo optimization.

For low energy investigations below the accessible photon energy of $\sim 20\ eV$ of grating 1, grating 2 can be inserted manually. This has been done for the threshold spectroscopy part of this work, since grating 2 allows to go down to a photon energy of $\sim 15\ eV$ with a reasonable photon flux. However, this grating has a comparably large contamination with higher orders of this grating.

An energy calibration of the undulator and the monochromator has been done prior every beamtime using several noble gas resonances. Details on these resonances are shown in table 3.1.

Target	**Resonance**	**Resonance Energy (eV)**	**Reference**
Helium	$1s \rightarrow (n=2)^2$	60.147	Domke *et al.* 1996
Xenon	$4d_{\frac{5}{2}} \rightarrow 6p$	65.11	King *et al.* 1977
Krypton	$3d_{\frac{5}{2}} \rightarrow 5p$	91.2	King *et al.* 1977
Argon	$2p_{\frac{3}{2}} \rightarrow 4s$	244.39	King *et al.* 1977
Neon	$1s \rightarrow 3p$	867.12	Coreno *et al.* 1999

Table 3.1: Resonances for beamline energy calibration [30, 40, 69].

Usually this calibration cross check is showing only very small discrepancies in the order of $< 100\ meV$ for almost the whole energy range. But in the discussion of the results on near threshold phenomena of N_2, O_2 and CH_4 this calibration is crucial, since some of the observed features have a FWHM in the order of this discrepancy. The beamline is operating very stable and despite its long scientific

use for about 20 years it is still highly competitive for soft X-ray research.

The polarization determination of the provided light was done prior and redundantly during every beamtime by analyzing several s-orbital electrons preferably of helium since their β is strictly 2 and every signature indication in the vertically aligned detectors would imply a lack of full horizontal linear polarization.

The beamline control for the undulator and monochromator setting and alignment can be done directly at the beamline computer or via remote commands of an external computer system. The data acquisition software utilizes remote commands in order to record data in automated photon energy scans.

The P04 beamline at PETRA III

A new beamline for soft X-ray science, namely the *P04 Variable Polarization XUV Beamline*, came up to work very recently at the PETRA III storage ring also located at DESY in Hamburg. Since this beamline was built in parallel to this thesis its opportunities for science will be briefly summarized. The low emittance storage ring PETRA III was inaugurated in November 2009 and is in the present status one of the most brilliant storage ring based synchrotron radiation light sources in the world [5]. The outstanding performance of PETRA III as diffraction limited synchrotron radiation source in the XUV photon energy regime raises the possibility of setting up an exceptional beamline in terms of photon flux, energy resolution and small focal spot size.

The *P04 Variable Polarization XUV Beamline* provides high photon flux $> 10^{12} \frac{photons}{s}$ at an energy resolution > 10000 over the full accessible photon energy range from 250 to 3000 eV. Two similar beamline branches are set up in order to ensure an efficient use. At the present status (01/2012) a preliminary 'dummy' mirror of low optical quality is implemented in the plane grating monochromator. Therefore, this setup can only be used to allow and verify a proper alignment of the beamline but the energy resolution is presently just in the order of ~ 1000. Once the designed premirror is available the energy resolution will be improved to the specified performance. The five meter long APPLE II undulator provides linearly polarized light with a variable polarization plane as well as circularly polarized light by longitudinally adjustable magnetic structures. The schematic layout is shown in figure 3.18.

The properties of the P04 beamline will extend the possibilities of experiments such as the presented in this thesis in an essential way. Although the near threshold photon energy region for valence states of small molecules as they were part of this work is not accessible, the high photon flux and the high energy resolution will allow investigations on processes with even lower cross sections than those accessible with e.g. the BW3 beamline. This means that detailed studies of subtle effects like e.g. the two center interferences in the photoionization of homonuclear diatomic molecules could be expanded to even larger photon energies with high statistical accuracy. The presented ARPES spectrometer setup (see section 3.1.1) is implemented in both branches of the P04 beamline as an online diagnosis tool providing all relevant beam parameters for the users (see section 3.1.6).

Summarizing this chapter, the newly developed highly efficient angle resolving photoelectron spectrometer setup was introduced as the basis of the studies presented the following chapter. Furthermore, the beam diagnostic capabilities of the spectrometer were highlighted to be an essential improvement of diagnostics for storage ring as well as free-electron-laser based synchrotron radiation sources. Embedded in these sections were first hard X-ray as well as free-electron-laser investigations showing the versatile adaptability of the setup. Closing this chapter with a short presentation of the upcoming P04 beamline at PETRA III in turn opens the view on wide spread new opportunities for soft X-ray science.

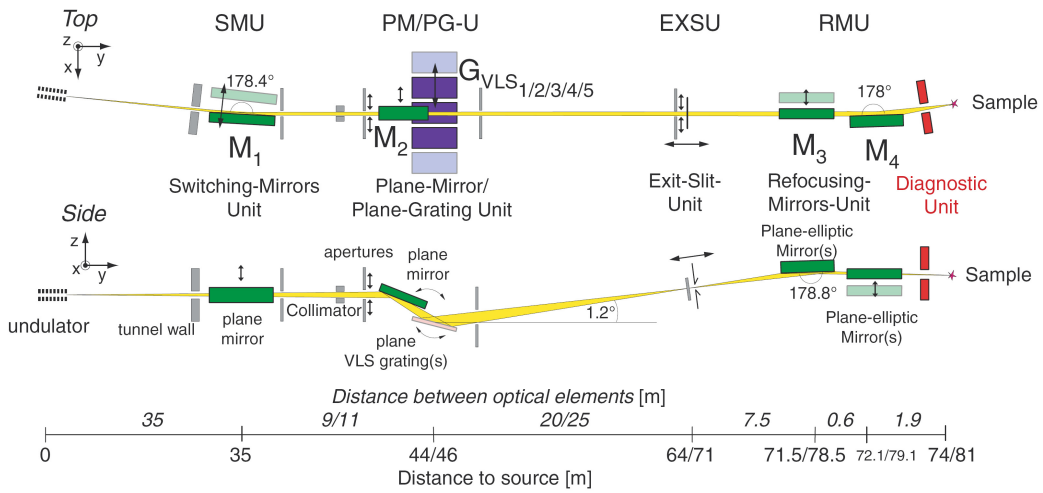

Figure 3.18: Conceptual design of the P04 Variable Polarization XUV Beamline at PETRA III at DESY in Hamburg.

Chapter 4

Molecular Photoionization Effects

In this chapter, the angle resolving photoelectron investigations on small molecules will be presented and discussed. The first section highlights near threshold phenomena in the angular distribution of outer valence electrons of N_2 and O_2. Shape resonant behavior as well as interchannel coupling and vibrational states are crucial for discussing the near threshold data up to 50 eV.
The next section represents the main work of this thesis, namely the first observations of molecular two center interference effects in the angular distribution parameter of valence electrons from N_2 and O_2 in a broad photon energy range from threshold up to 600 eV. The theoretical work of Toffoli *et al.* (2006) [130] on two center interference based electron angular distribution effects in the valence ionization of N_2 was initially predicting β-data in the frame of the Cohen-Fano formalism on interference effects in the molecular photoionization [26]. Proving these theoretical findings and highlighting the relation to the originally discussed interference in the paper of Cohen and Fano in 1966 [26] for N_2 and O_2 were the task of several beamtimes. These Cohen-Fano type oscillations will be discussed in comparison to additionally observed dynamical photoionization effects as well as prior performed experiments on inner shell electron orbitals of homonuclear diatomic molecules [151]. As a step toward more complex systems, angular distribution dynamics will then be discussed for the polyatomic heteronuclear molecule CH_4 in order to initialize first considerations of a molecular multi-slit experiment.

4.1 Near Threshold Phenomena of N_2 and O_2

As extensively discussed in the previous chapters, angle resolving photoelectron spectroscopy is a well-established method to get insight into the electronic structure of atoms and molecules. In order to obtain fundamental understanding and to test an extrapolation of basic models to more complex systems the most prominent targets are small molecules like e.g. N_2 and O_2.

During the investigations of homonuclear diatomic molecules in a broad energy range it was essential to compare the experimental data to existing literature values for angular distributions on these targets. One obvious reason is the classification and validation of the experimental accuracy in comparison to other experiments, but the investigation was especially triggered by the fact that a large scatter for the literature β-values in the photon energy range from threshold to 50 eV was found to be well beyond the stated accuracy of the literature data.

Almost all available β-data for N_2 and O_2 deal with investigations in this low photon energy regime however, a study of the electron angular distribution has never been done with a sufficiently small photon energy step width in order to resolve e.g. Rydberg enhanced doubly excited resonance features. In the following section the angular distribution of the outer valence electrons of N_2 namely $3\sigma_g$, $1\pi_u$, $2\sigma_u$ are discussed, continuing with the $1\pi_g$ HOMO of O_2.

4.1.1 Near Threshold Phenomena of N_2

N_2 is principally one of the most simple molecular systems leading to an extensive effort in both experimental and theoretical studies of this target's angular distribution properties since decades. Even though experiment and theory are agreeing on several basic effects in the photoionization of N_2 outer valence shells, persisting discrepancies are to be solved in the photon energy region close to threshold.
Angle resolved photoelectron data for the ionization of all N_2 outer valence shells, namely the $3\sigma_g$, $1\pi_u$ and $2\sigma_u$ states, in the photon energy region from 19 to 50 eV with an energy step width of 20 meV is presented in this section. Hitherto experimentally unresolved Rydberg states exhibiting Fano-like profiles of down to $\sim$ 100 meV (Full Width at Half Maximum - FWHM) in the angular distribution anisotropy parameter β of electrons emitted from the $3\sigma_g$ state are observed. They are discussed in the light of recent calculations. A further broader feature in the β-parameter of the $3\sigma_g^{-1}$ state at 29 eV is unambiguously determined. Experimental evidence for theoretically predicted narrow resonance signatures [126] due to interchannel coupling in the electron angular distribution of $1\pi_u^{-1}$ is found.

To get an overview of the photoionization processes expected to influence the electron angular distribution in the near threshold photon energy range it is very useful to refer to existing cross section studies. Since absolute cross section data is usually available in much denser data sets as it is the case for higher differential angle resolved data, initial insight in several underlying processes can be derived and compared to the new angle resolved experimental results presented below.
Experimental findings on the cross sectional behavior of N_2 valence electrons concerning Rydberg enhanced fluctuations (Gürtler *et al.* (1977) [53], Peatman *et al.* (1978) [99], Berg *et al.* (1991) [10]) have never been studied in comparable accuracy for the photoelectron angular distribution. Figure 4.1(a) shows the different photoionization cross sections for the outer valence states of N_2 allowing to derive the expectable intensity distributions for the recorded photoelectron spectra. The cross section data in figure 4.1 was chosen for this illustration giving a very basic and still valid picture on the relative intensity to be expected in the respective photoelectron spectra. The integral intensities of the respective photoelectron lines show a very nice agreement with these predicted Hartree-Fock calculations (solid line) of Lucchese *et al.* (1982) [82]. Recalling figure 2.8, the binding energies for the shown orbitals are $E_{3\sigma_g} = 15.56\ eV$, $E_{1\pi_u} = 17.16\ eV$ and $E_{2\sigma_u} = 18.75\ eV$. These values are differing within several hundreds of meV

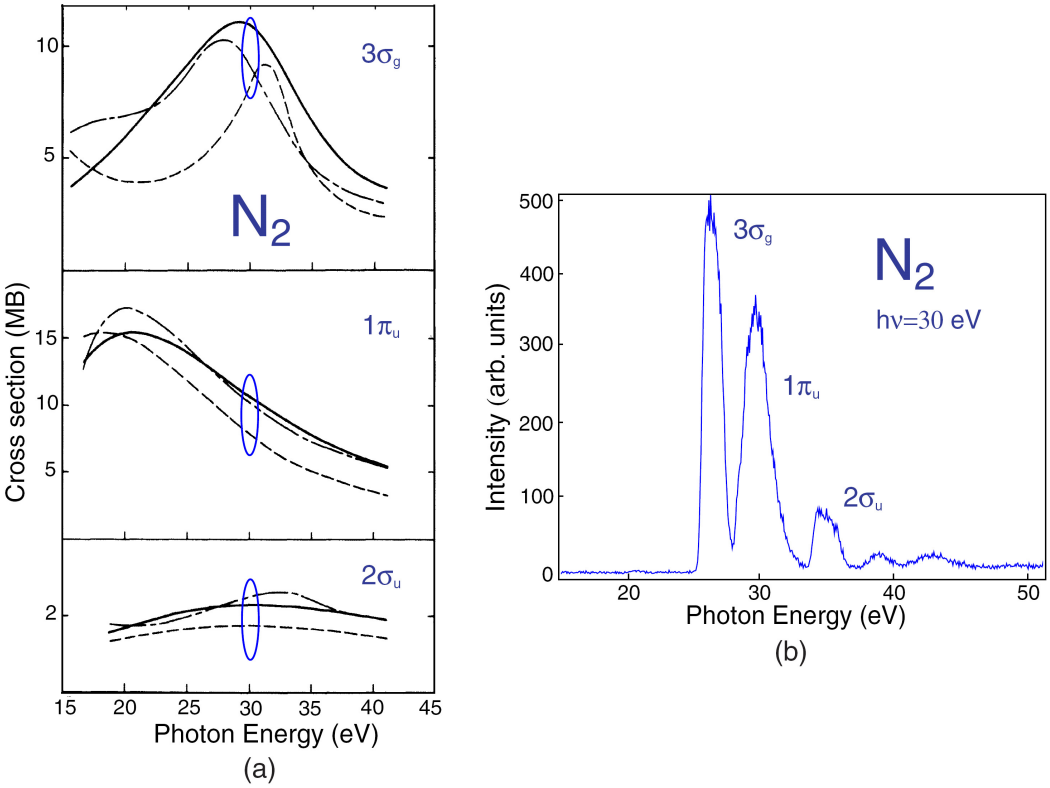

Figure 4.1: Figure (a) shows several theoretical cross section data for all outer valence orbitals of N_2 according to Lucchese *et al.* (1982) and references therein [82]. The blue ellipses mark this 30 eV photon energy position for an easy comparison. Figure (b) shows a typical electron photoelectron spectrum at $h\nu = 30\ eV$. The data is averaged over all spectrometers around the magic angle so it reflects approximately the cross section without angular distribution anisotropy influence.

between the different literature sources as it is e.g. shown in [124].

Comparing *highly energetically resolved cross section data* for N_2 (Gürtler *et al.* (1977) [53], Peatman *et al.* (1978) [99], Berg *et al.* (1991) [10]) in the relevant energy range as well as fluorescence data (Wu *et al.* (1984) [146]) even more information on photoionization effects in this photon energy range can be derived. To give an example in this concern, figure 4.2 shows highly resolved partial ion yield data of N_2 according to Berg *et al.* (1991) [10] designating many resonance features in the relevant photon energy region from ~ 22.5 to $\sim 26.5\ eV$.

Berg *et al.* (1991) [10] argue that these data undoubtedly originates from autoionization of the doubly excited N_2 states [10]. In detail the two depicted

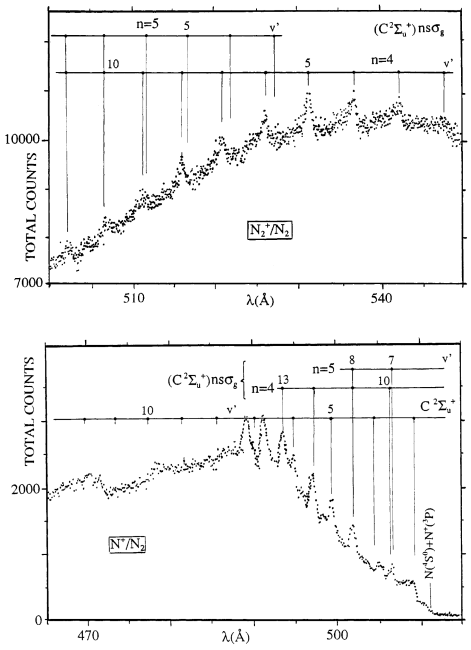

Figure 4.2: The figure shows highly resolved partial ion yield data for N_2 according to Berg *et al.* (1991) [10] labeling two predicted Rydberg series yielding two vibrational progressions for $n = 4$ and $n = 5$.

Rydberg states converging for higher n to the N_2^+ $C^2\Sigma_u^+$ promote one electron from the $1\pi_u$ and one from the $3\sigma_g$ to the orbitals $1\pi_g$ and $ns\sigma_g$ [10]. Although this data is integrating over all involved electron states, a comparison to the electron angular distribution data suggests that most of this resonance structure is related to the $3\sigma_g$ ionization.

Coming to the available angle resolved data for the outer valences of N_2, experimental studies have been performed by e.g. Marr *et al.* (1979) [85], Southworth *et al.* (1986) [120] and Iga *et al.* (1989) [63].
Theory on this topic is available from Stratmann *et al.* (1995) [124], Tashiro (2010) [126] and further authors ranging from Hartree-Fock approaches (Lucchese *et al.* (1982,1991) [82, 83]) over random phase approximation (RPA) (Cacelli *et al.* (1998) [20]) to density functional theory (DFT) (Toffoli *et al.* (2006) [130]) and time dependent density functional theory (TDDFT) (Decleva (2011) [36]). Detailed references and comprehensive introduction to the available theoretical models on this topic can be found in Cacelli *et al.* (1998) [20].

Based on the experimental and theoretical results available for the cross section as well as for the angular distribution, it can be concluded that many interesting effects are expected to occur for N_2 in the threshold photon energy region. The

effects discussed in the energy range from 19 to 50 eV are on the one hand the predicted shape resonances (Piancastelli (1999) for a general overview on shape resonances [100]) for the $3\sigma_g^{-1}$ and the $2\sigma_u^{-1}$ (Southworth (1986) [120]) and on the other hand Rydberg enhanced resonances and interchannel coupling (IC) for all outer valence ionization channels. This ensemble of effects will be fully covered by the presented data. Therefore, the new measurements made in the frame of this thesis comprise highly dense data sets of the angular distribution anisotropy parameter β for all outer valence shells of N_2. All β-data is vibrationally averaged, not taking vibrationally induced energy splitting of the corresponding orbitals into account.

Angular Distribution Effects in N_2 $3\sigma_g^{-1}$

Figure 4.3 shows the available data for the electron angular distribution parameter β of N_2 $3\sigma_g$ ionization. The theoretical curves are taken from Decleva (2011) [36] and Tashiro (2010) [126]. In the experimental data (citations in the caption of figure 4.3) one can clearly see a dip in the energy region from 20 to 23 eV. The reason is under discussion to be originated either by Rydberg enhanced coupling to the $C\ ^2\Sigma_u^+$ state (Codling (1966) [25]) or by doubly excited valence-like states (Wendin (1979) [141]). Following the arguments of Southworth *et al.* (1986) [120] the latter interpretation of Wendin (1979) [141] is reasonable, because of the short lifetimes of doubly excited valence-like states explaining the broad width of the discussed dip in β. Compared to doubly excited valence-like states, Rydberg enhanced coupling should lead to narrower features due to their longer lifetime. Cross section or partial ion yield data of e.g. Berg *et al.* (1991) ([10] and references therein) however indicate Rydberg enhanced resonances in the photon energy region around 23 eV. According to figure 4.2, these resonances are observed as a superimposed signature on a broader feature. Comparing the relevant literature for β-data in this photon energy region with ion yield data of Berg *et al.* (1991), the observed broad feature at $\sim$ 22 eV could be originated by doubly excited valence-like states, whereas the Rydberg resonances predicted by the ion yield data have no observed correspondence in the available electron angular distribution data.

Signatures of the shape resonance in the β of the $3\sigma_g^{-1}$ electrons should be spread over more than 5 eV and give rise to small changes observable mainly in vibrationally resolved data [120]. Therefore, even smaller influence on the vibrationally

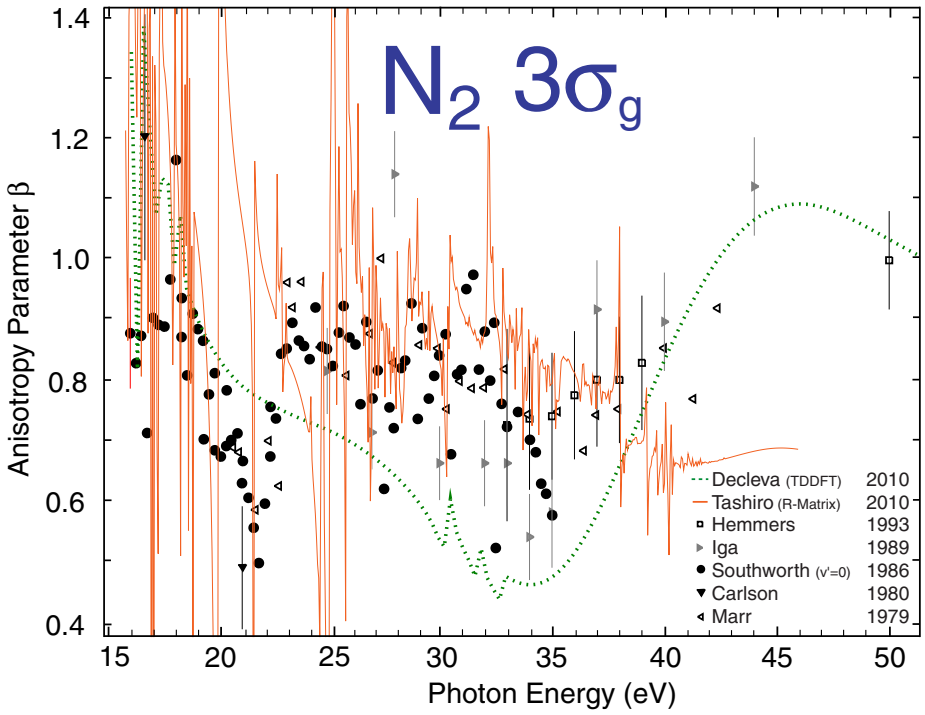

Figure 4.3: Photoelectron anisotropy parameter β of the $3\sigma_g^{-1}$ state of N_2. A large scatter of the available data is the energy region from threshold to 50 eV is observed. Theoretical data of Tashiro (2010) [126] and Decleva (2011) [36] and experimental data of Hemmers (1993) [55], Iga *et al.* (1989) [63], Southworth *et al.* (1986) [120], Carlson *et al.* (1980) [23] and Marr *et al.* (1979) [85] is shown. Error bars are only partially included for a clearer overview.

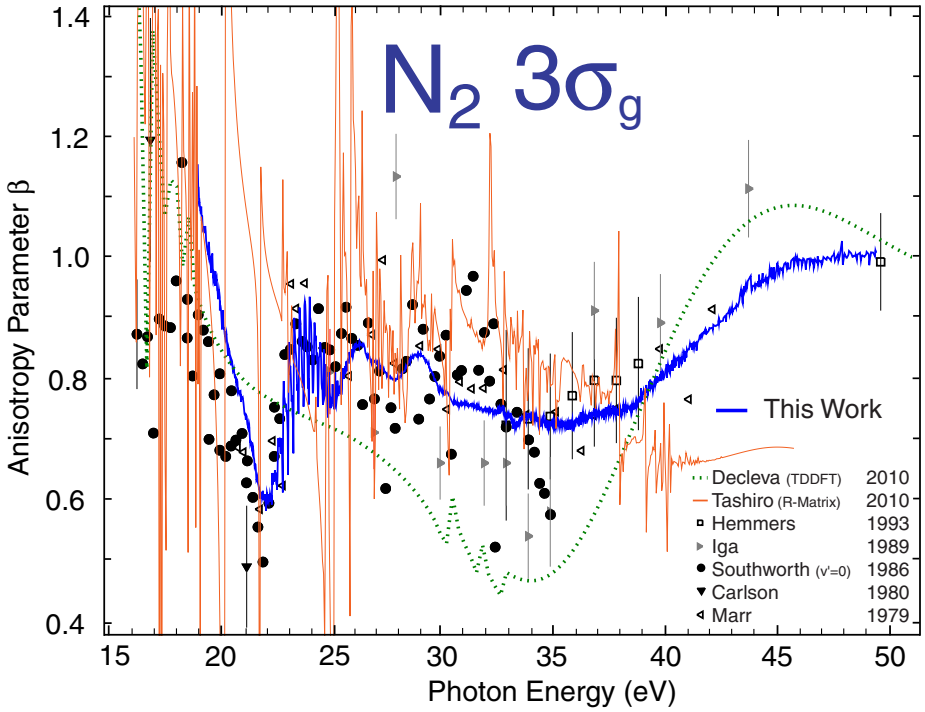

Figure 4.4: β-data of this work up to 50 eV in comparison to previous experimental and theoretical data as they are cited in figure 4.3. The uncertainties of this work's data are discussed in the text.

averaged β-parameter (Carlson *et al.* (1980) [23], Dehmer *et al.* (1979) [38]) is expected.

Figure 4.4 shows the development of the angular distribution data of this work over the photon energy. The dip at $h\nu = 22\ eV$ already discussed earlier is clearly verified with the new experimental data. It is in principal agreement with former experiments, but more structures can be seen. These resonance structures shown in figure 4.4 are occurring in the same photon energy range as it is the case for the absorption cross section data. The intensity progression is also in qualitative agreement. Regarding the cross section and ion yield data of Gürtler *et al.* (1977) [53] and Berg *et al.* (1991) [10], the sharp structures observed in their work are superimposed on a broad bump as it can accordingly be derived from the β-data shown in figure 4.5. Despite the fact that the angle resolved theory of Stratmann *et al.* (1995) [124] and Tashiro (2010) [126] is only in qualitative agreement with the new β-data, it is the only data indicating the deep dip around

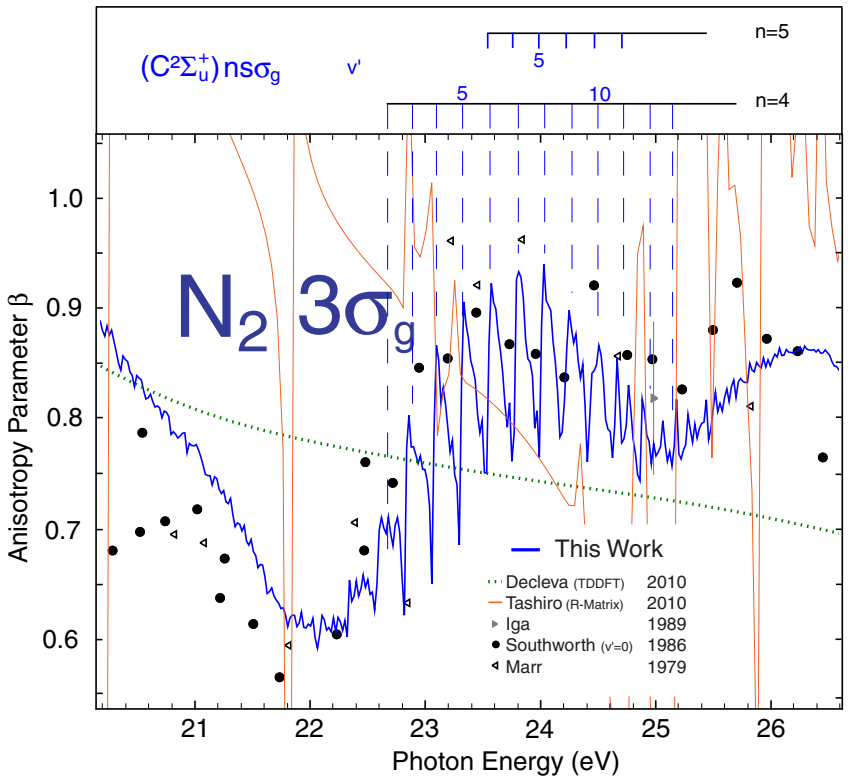

Figure 4.5: Enlarged view on the resonance features between 22 - 26 eV including all relevant experimental and theoretical data as they are cited in figure 4.3. The scale above the figure depicts the Rydberg series according to Berg *et al.* (1991) [10] (see figure 4.2).

22 eV with additional sharp features superimposed at energies $>$ 22 eV in line with the presented observations. Since the data of Tashiro (2010) [126] indicates similar features in comparison to Stratmann *et al.* (1995) [124] and furthermore expands the predicted resonance structures by far, the calculations of Stratmann *et al.* (1995) [124] are not implemented in the figures of this section to ensure a clearer view on the voluminous data.

A zoom in the region of the rising edge of the structure at around 22 eV is shown in figure 4.5. It unravels clearly defined resonances showing close similarities to Fano profiles within $\sim$ 200 meV down to less than 100 meV. These features start directly at the bottom of the rising edge of the dip at 22 eV and fade out to 26 eV. Due to its narrow and decreasing width this structure could be a signature of the widely discussed Rydberg enhanced autoionization states converging to the $C\ ^2\Sigma_u^+$ state (e.g. Berg *et al.* (1991) [10] and Codling (1966)

[25]), also present in respective fluorescence data of Wu *et al.* (1984) [146]. The positions of the different v' states in both n-series according to the ion yield data of Berg *et al.* (1991) [10] as they are depicted in figure 4.5 are in good agreement with the observed features in the β-data of this work. Especially the resonance structures in the β-data between 23 and 24 eV show very small and narrow additional peaks at the bottom of the respective falling edge. These additional structures might be originated by the $n = 5$ series as it is also depicted in figure 4.5. However, they are close to the relative uncertainty of the β-data of this work in that photon energy region.

Additional hitherto unobserved features can be seen in figure 4.4 at 26.5 and 29 eV. The latter is placed on the center of the shape resonance according to theory (e.g. Stephens *et al.* (1985)). Bearing in mind the interpretations of Dehmer *et al.* (1979) [38] and Carlson *et al.* (1980) [23] pointing to a width of the shape resonance of larger than 5 eV a direct correspondence in these features with the shape resonant origin is unlikely because of their smaller width of $\sim$ 1 eV. More likely these features are originated by doubly excited valence like states as it was probably the case for the dip at 22 eV.

Two findings are hitherto unobserved for the electron angular distribution of the N_2 $3\sigma_g$ state in this photon energy region: (a) Sharp Rydberg enhanced Fano-like profiles superimposed on the well discussed dip at 22 eV and (b) clearly pronounced features at 26.5 and 29 eV whose origin has to be revealed in future theoretical work.

Angular Distribution Effects in N_2 $1\pi_u^{-1}$

For the angular distribution of the electrons emitted from the $1\pi_u$ state less theories and experimental data are available. Calculations of Stratmann *et al.* (1995) [124] and Tashiro (2010) [126] gave rise to a search for sharp fluctuation features in this ionization channel. The electron angular distribution of $1\pi_u$ ionization leading to the $A\ ^2\Pi_u^+$ state is shown in figure 4.6. The experimental data of Hemmers (1993) [55] and Marr *et al.* (1979) [85] are in agreement with the gross shape of the new β-data over the photon energy. A formerly discussed peak in the experimental data of Marr *et al.* (1979) [85] at around 38 eV interpreted to be originated by Rydberg series converging to the $2\sigma_g$ state (Lucchese *et al.* (1991) [83], Cacelli *et al.* (1998) [20]) cannot be approved by the results of this

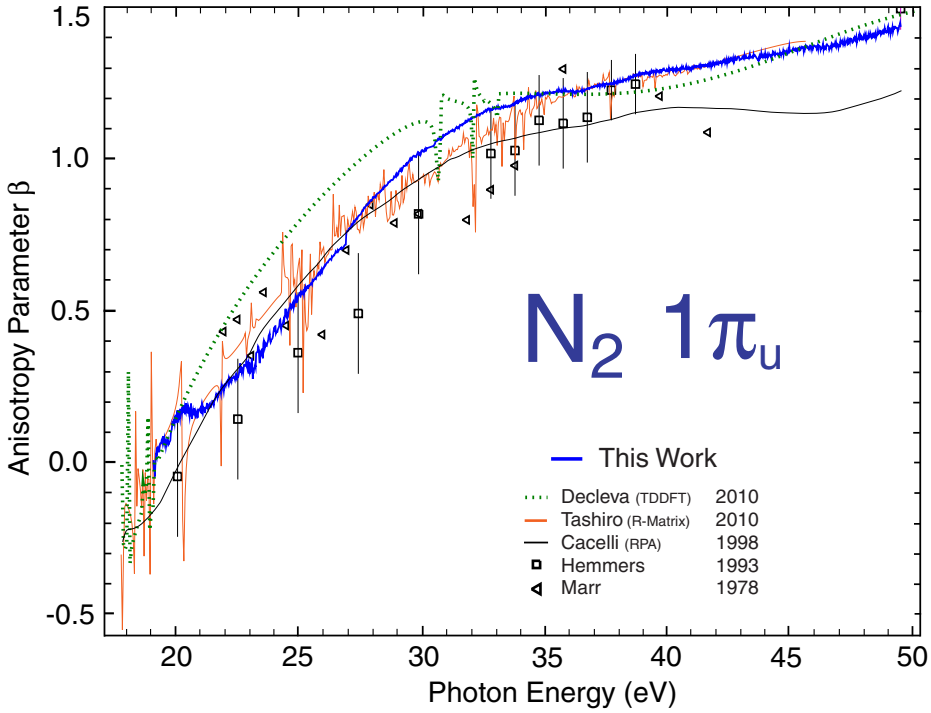

Figure 4.6: Photoelectron anisotropy parameter β of the $1\pi_u^{-1}$ state of N_2 including the data of this thesis. Theoretical data of Tashiro (2010) [126], Decleva (2011) [36] and Cacelli *et al.* (1998) [20] as well as experimental data of Hemmers (1993) [55] and Marr *et al.* (1979) [85] is shown. The uncertainties of this work's data are discussed in the text.

thesis. The general agreement of the new data with the theoretical β-data of the $1\pi_u^{-1}$ of Cacelli *et al.* (1998) [20], Decleva (2011) [36] and Tashiro (2010) [126] is remarkable. The results of Cacelli *et al.* (1998) [20] suggest that inter channel coupling is not very important here, except for the near threshold photon energy region. However, their single channel results (SC) (as they are implemented in figure 4.6) seem to be even closer to the new data in that photon energy range. Major discrepancies are found in a predicted resonance feature between 20 and 21 eV by Stratmann *et al.* (1995) [124] and Tashiro (2010) [126] which is not evident in the new data. The calculated narrow fluctuations in the β-parameter

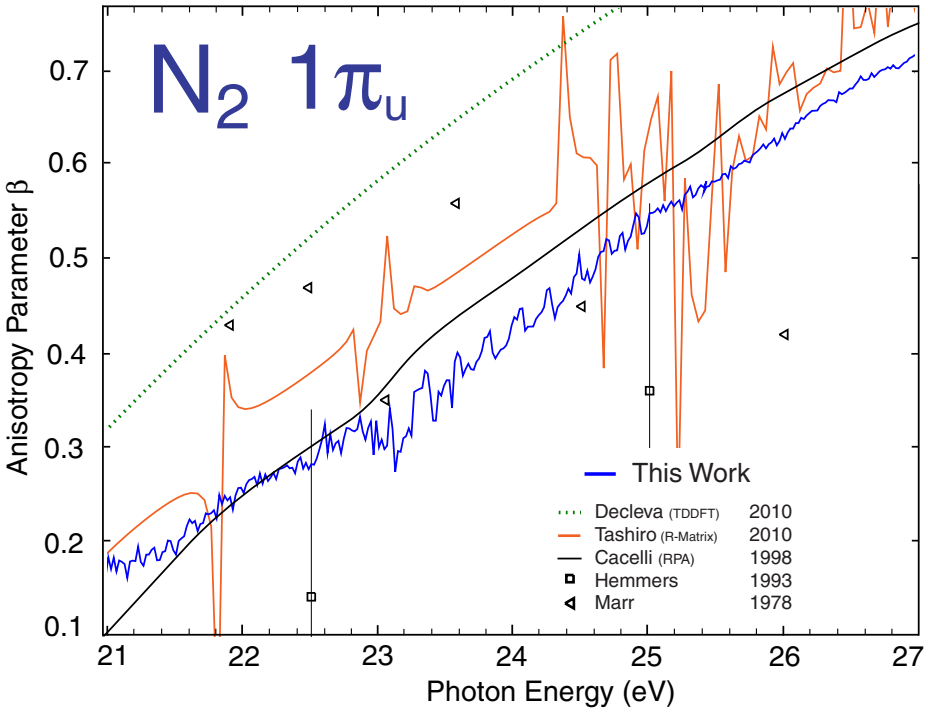

Figure 4.7: Enlarged view on the resonance features between 23 - 25 eV including all relevant experimental and theoretical data as they are cited in figure 4.6.

between 25 and 35 eV predicted by Tashiro (2010) [126] are not in full agreement with the new data, but resonance structures of comparable width have been measured in the range between 22 and 26 eV (figure 4.7). These structures are damped in comparison to the discussed resonance structures occurring in the β of the $3\sigma_g^{-1}$ state but most likely originated by Rydberg enhanced coupling. Further theoretical progress is needed to acccurately describe this experimental data.

Angular Distribution Effects in N_2 $2\sigma_u^{-1}$

Coming to the third orbital, the N_2 $2\sigma_u^{-1}$, it can be expected from theory of Tashiro (2010) [126] that sharp resonance structures are evident in β-data. Furthermore and in principal agreement with the calculations of Cacelli *et al.* (1998) [20] a plateau from 25 to 35 eV with two superimposed broad peaks is predicted (see figure 4.8).

According to Southworth *et al.* (1986) [120], not only a plateau is observed at that photon energy position, but a very pronounced broad dip (see figure 4.8). They interpret this deep dip to be of shape resonance origin due to a coupling of $(2\sigma_u^{-1})(\epsilon\sigma_g)$ $^1\Sigma_u^+$ and $(3\sigma_g^{-1})(\epsilon\sigma_u)^1\Sigma_u^+$ in line with the theoretical interpretations of Stephens *et al.* (1985) [121]. The theory of Stephens *et al.* (1985) [121], including the relevant coupling of the X $^2\Sigma_g^+$ and B $^2\Sigma_u^+$ channels, predicts a similar feature however, only in very qualitative agreement. This β-feature in the energy range from 27 eV to 32 eV is discussed controversial e.g. by Tashiro (2010) [126] because it is not reproduced by the several other authors (cited in figure 4.8). As Southworth *et al.* (1986) [120] suggest, this discrepancy between the existing β-data could be originated by a high influence of resonances to the angular distribution of electrons from the individual vibrational states. The data of Southworth *et al.* (1986) [120] is exclusively analyzed for the $v' = 0$ states of the respective orbitals, whereas the other data sets are vibrationally averaged. The difference between vibrationally averaged and $v' = 0$ β-data is usually very low since the Franck-Condon factor is very high for $v' = 0$. Nevertheless, non Franck-Condon behavior might be evident especially for resonance energies possibly explaining the discrepancy in β-data.

The electron angular distribution of the $2\sigma_u$ ionization leading to the B $^2\Sigma_u^+$ state is shown up to photon energies of 50 eV in figure 4.8. The statistical uncertainty in this data is higher than for the $1\pi_u$ and for the $3\sigma_g$ but still in the order of ± 0.05 β-units.

Experimental data of Southworth *et al.* (1986) [120] and of Marr *et al.* (1979) [85] are in disagreement with the new data up to 25 eV. The data of this work indicate a narrow peak at 23 eV which is in qualitative agreement with the data of Tashiro (2010) [126]. It is the only data predicting a similar feature at that

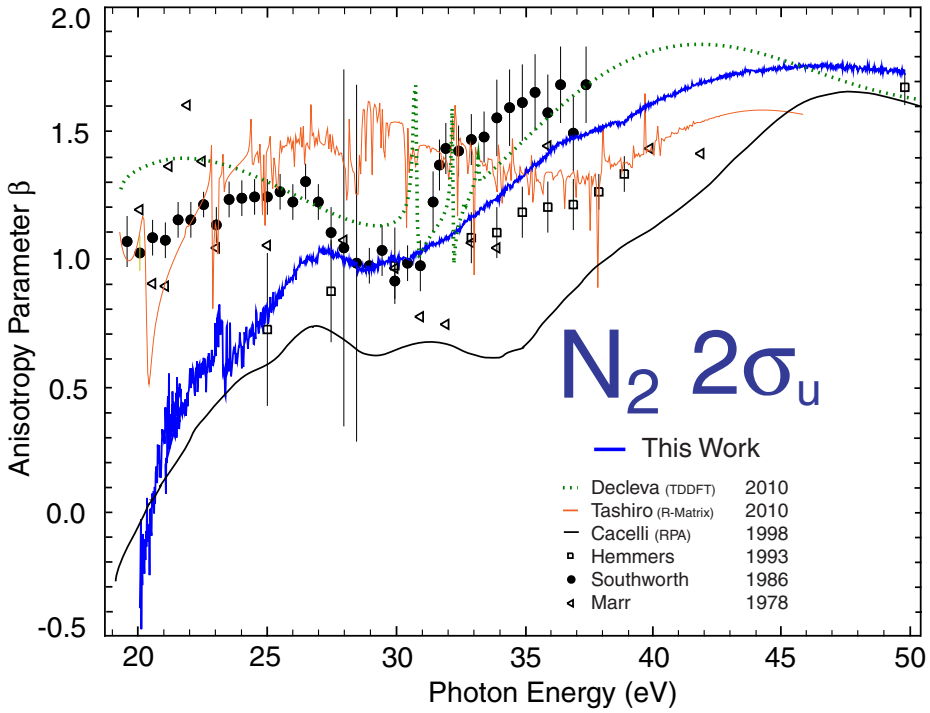

Figure 4.8: Photoelectron anisotropy parameter β of the $2\sigma_u$ ionization of N_2. Theoretical data of Tashiro (2010) [126], Decleva (2011) [36] and Cacelli *et al.* (1998) [20] as well as experimental data of Hemmers (1993) [55], Southworth *et al.* (1986) [120] and Marr *et al.* (1979) [85] is shown. The uncertainties of this work's data are discussed in the text.

photon energy and its origin has to be revealed in future interpretation. The data of Hemmers (1993) [55] is consistently too low in this energy range most likely due to a systematic calibration error as he suggests in his work.

Interchannel coupling including calculations of Cacelli *et al.* (1998) [20] show a plateau between 26 and 35 eV in the β-parameter absent in the calculations of Stratmann *et al.* (1995) [124] but consistent with the new data, even though the absolute β-value is differing. This plateau is located in the same photon energy range as the observed shape resonance feature in the data of Southworth *et al.* (1986) [120]. Regarding the discussion about resonance induced non Franck-Condon behavior above, it is reasonable that the plateau has the same origin as the dip in the data of Southworth *et al.* (1986) [120], namely the σ_u shape resonance. If this is the case, the comparison of the vibrationally averaged data

of this work with the $v' = 0$ data of Southworth *et al.* (1986) [120] can initially provide insight in shape resonance induced non-Franck-Condon behavior for the electron angular distribution.

Cacelli's (1998) [20] calculations show a substructure of two broad peaks superimposed on the mentioned plateau. Both are indicated by the experimental data of this thesis, even though the second peak to a lesser extend. According to the interpretation of similar structures for the N_2 $3\sigma_g^{-1}$ as described earlier, these peaks might be originated by valence-like doubly excited autoionization states. The strong β-increase in the calculations of Cacelli *et al.* (1998) [20] after the plateau is not in agreement with the new data but the absolute β values do converge above 45 eV.

In the $2\sigma_u^{-1}$ the situation for the theoretical description is similar to the other two outer valence states. There is some general agreement however, a description of the details observed by the presented experiment (see section 3.1.1) is still lacking. On the experimental side in particular, the threshold region of the $2\sigma_u^{-1}$ state should be covered with emphasis on much better statistical accuracy. This would probably better be studied at a dedicated low photon energy source equipped with a normal incidence monochromator, providing much higher photon flux in the photon energy range below 30 eV compared to the grazing incidence monochromator used for this work.

Summarizing the results for the low photon energy studies of the N_2 outer valence shells, resonance structures have been observed in the electron angular distribution in accordance to available cross section data. Also completely unexplored features are indicated by the experimental data of this thesis. The hitherto unseen effects in the electron angular distribution can now be discussed on the basis of a much denser and more accurate bulk of angle resolved data. E.g. for the $3\sigma_g$ state sharp fluctuations on the rising edge of the dip at 22 eV with a FWHM in the order of 200 meV are clearly shown. Furthermore, previously unobserved features at $h\nu = 26.5$ eV $h\nu = 29$ eV are clearly evident in the ionization of this orbital. Their relation to the shape resonance of N_2 is not clear yet and theoretical effort in this concern is desirable. For the $1\pi_u^{-1}$ electron angular distribution the new data show also very sharp β-fluctuations being initially predicted by Tashiro (2010) [126], but shifted in energy compared to the recent measurements. For the $2\sigma_u^{-1}$ broad peaks, probably due to doubly excited valence-like states, were

observed in agreement with recent theory. The $2\sigma_u^{-1}$ shape resonance relation of this work's data with $v' = 0$ resolved data has also to be interpreted in future theoretical work.
These effects in particular but also the new highly accurate β-data sets for all outer valence shells of N_2 should encourage theoreticians to improve their calculation accuracy to be able to better describe photoionization dynamics of N_2 valence states close to the ionization thresholds.

4.1.2 Near Threshold Phenomena of O_2

The experimental investigations presented in this work on the O_2 photoionization are limited to the outermost valence shell, namely the $1\pi_g$, in order to compare general effects with the ionization of the N_2 valences. Angle resolved photoelectron data for the ionization of this HOMO of O_2 is presented in an photon energy range from 20 to 50 eV. In order to resolve the theoretically predicted Rydberg type autoionization states in the electron angular distribution, a photon energy step width of 5 meV is applied for the energy regions where these resonance features are observed. Two separated photon energy regions from 19 to 21 eV and from 22.5 to 24.5 eV are determined to show such resonantly enhanced fluctuations of the electron angular distribution. In comparison to the N_2 angular distribution data these spikes are found to be even sharper with comparably larger changes of up to 0.5 β-values.

In contradiction to the closed shell molecule N_2, O_2 is a more complex open shell molecule. The ground state configuration is

$$(1\sigma_g)^2\ (1\sigma_u)^2\ (2\sigma_g)^2\ (2\sigma_u)^2\ (1\pi_u)^4\ (3\sigma_g)^2\ (1\pi_g)^2 \tag{4.1}$$

and the ground state symmetry is $^3\Sigma_g^{-1}$ having 2 unpaired electrons. Photoionization of the valence states of O_2 is leading to several possible ionic states with partly very similar ionization energies. Further complexity is induced by Rydberg enhanced autoionization states [80] as it was the case for N_2. An overview of the vertical and adiabatic ionization potentials can be found in an article of Lin *et al.* (2002) [80] comparing theoretical results with experimental findings of Baltzer *et al.* (1992) [6].

Figure 4.9 shows the manifold possible final ionic states for the photoionization of O_2 valence states. Various literature values for the respective binding energies of the valence electron states can be derived from the table. Some of the electron final states are overlapping in the measured photoelectron spectra which is shown in figure 4.10(b). This figure shows a typical electron time-of-flight spectrum of O_2 at a photon energy of 30 eV. It is averaged, as it was done for N_2, over all angles around the magic angle so angular distribution anisotropy can be neglected and a comparison to the partial cross sections shown in figure 4.10(a) becomes feasible.

As it is the case for N_2, high resolution absolute cross section data is avail-

State	Principal configuration	CASCI (Vertical)	MRCI (Vertical)	MRCI (Adiabatic)	Experiment (Vertical)[a]	Experiment (Adiabatic)[a]
$X\,^2\Pi_g$	$1\pi_g^{-1}$	12.169[b,c]	12.147	11.942	12.307	12.074
$a\,^4\Pi_u$	$1\pi_u^{-1}$	16.758[b,c]	16.724	15.820	16.703	16.101
$A\,^2\Pi_u$	$1\pi_u^{-1}$	17.839[b,c]	17.796	16.779	17.643	17.045
$b\,^4\Sigma_g^-$	$3\sigma_g^{-1}$	18.851[b,c]	18.156	17.949	18.171	18.171
$1\,^2\Phi_u$	$1\pi_u^{-1}$	19.264[b]	19.175	18.276	19.1[d]	⋯
$1\,^2\Delta_g$	$3\sigma_g^{-1}$	20.523[b]	19.949	19.591	19.90[d]	⋯
$B\,^2\Sigma_g^-$	$3\sigma_g^{-1}$	21.032[b,c]	20.404	20.122	20.296	20.296
$2\,^2\Pi_u$	$1\pi_u^{-1}$	20.317[b]	20.499	19.417	⋯	⋯
$1\,^2\Sigma_g^+$	$3\sigma_g^{-1}$	21.053[b]	20.670	20.145	⋯	⋯
$3\,^2\Pi_u$	$1\pi_u^{-1}$	24.251[b,c]	23.983	21.228	23.9	21.32
$c\,^4\Sigma_u^-$	$2\sigma_u^{-1}$	25.147[c]	24.462	24.383	24.564	24.564
$2\,^2\Sigma_u^-$	$2\sigma_u^{-1}$	28.653	⋯	⋯	27.3	⋯
$3\,^2\Sigma_u^-$	$2\sigma_u^{-1}$	34.835				
$5\,^4\Sigma_g^-$	$2\sigma_g^{-1}$	42.558				39.6
$6\,^2\Sigma_g^-$	$2\sigma_g^{-1}$	42.471				41.6
$11\,^2\Sigma_g^-$	$2\sigma_g^{-1}$	51.182				

Figure 4.9: Table taken from [80] and references therein, comparing theoretical results of ionization potentials with experimental data [6, 65]. The data is underlining the widespread possible transition channels with similar principal configurations and different ionic states.

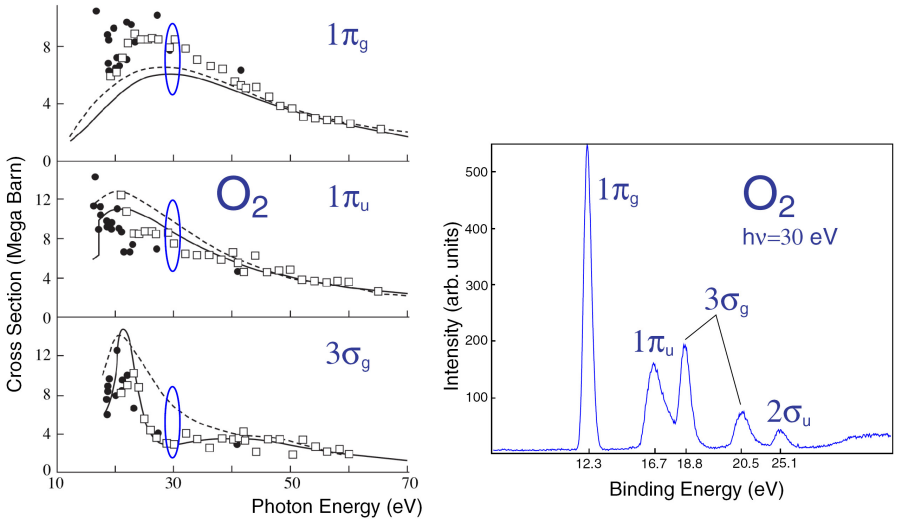

Figure 4.10: Figure (a) shows partial cross sections of the outer valence states O_2 according to Demekhin *et al.* (2007) [39] and references therein. (b) shows the corresponding photoelectron spectrum of O_2 at $h\nu = 30\ eV$.

able for the relevant photon energy region including an identification of several autoionization states. This data is shown in figure 4.11. Beside the designated

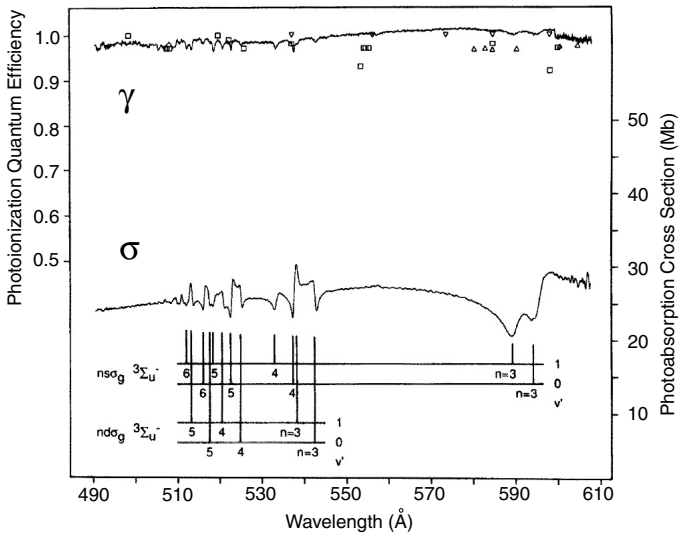

Figure 4.11: Absolute photoionization cross section data for O_2 taken from Holland *et al.* (1993) [58] labeling all occurring ionization features in the photon energy range from 20.3 to 25.3 eV.

features, Holland *et al.* (1993) [58] point out the weak structures superimposed on the broad feature ranging from 21 to 22.7 eV. Since the absolute photoionization cross section does not differentiate the various open ionization channels, overlapping effects could partly 'wash out' the resonance structures.

According to the available literature the general effects expected in the photoionization of the O_2 $1\pi_g$ state leading to the $X\ ^2\Pi_g$ ionic state are autoionization states from threshold to 20 eV according to Stratmann *et al.* (1995) [123]. As presented in the theoretical work of Lin *et al.* (2002) [80] including up to 10 different transition channels in the calculations, Rydberg enhanced autoionization states are predicted to occur up to 26 eV. Furthermore, a shape resonance related feature is stated to occur for ionization of the O_2 $1\pi_g$ in the $k\sigma_u$ channel very close to threshold at around 13 eV [80]. The comparability to closed shell linear molecules like e.g. N_2 in terms of the typical shape resonance due to a σ^* coupling is lacking (Braunstein *et al.* (1989) [17]). This is caused by the fact that this antibonding σ^* resonance is below the ionization threshold for O_2 for equilibrium bond length [123]. Lin *et al.* (2002) [80] argue that this shape resonance should be hardly measurable because of its weak intensity and an overlap with several strong autoionization states. However, due to the limits of the monochromator the photon energy of ~ 12 eV was inaccessible for our studies.

Furthermore, a broad cross section feature attributed to the $l = 3$ partial wave component leading to an enhancement in the $1\pi_u \rightarrow k\pi_u$ component at ~ 28 eV [80] is observed between 20 and 40 eV. This feature should also influence the

angular distribution gross shape in an essential extent in the same broad photon energy region. It is not predicted to lead to superimposed narrow resonance structures.

Experimental angular distribution studies on O_2 have been performed by e.g. McCoy *et al.* (1978) [87] and Holmes *et al.* (1980) [59]. Further β-data points at few photon energies can be found in Carlson *et al.* (1971) [22] and Hancock *et al.* (1976) [54]. Figure 4.12 shows the relevant experimental data in comparison to selected theoretical calculations. Several of the predicted Rydberg

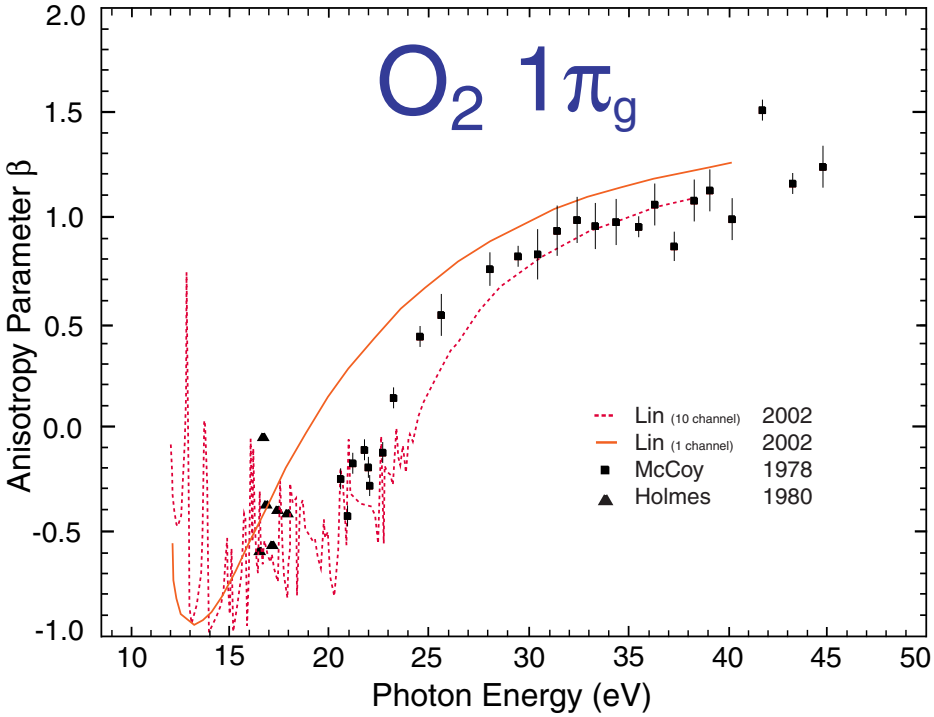

Figure 4.12: Available experimental and theoretical data for the ionization of O_2 $1\pi_g$ leading to the $X\ ^2\Pi_g$ ionic state. The theoretical data is calculated by Lin *et al.* (2002) [80], whereas the experimental data is taken from McCoy *et al.* (1978) [87] and Holmes *et al.* (1980) [59].

enhanced autoionization states can be derived from theoretical literature values (e.g. [80, 128]), whereas the experimental data is showing only little indication for resonance structures [59, 87]. In the photon energy region around 21 eV McCoy *et al.* (1978) [87] argue that a negative β-parameter in that photon energy region should occur due to a domination by parity unfavored transitions but as already

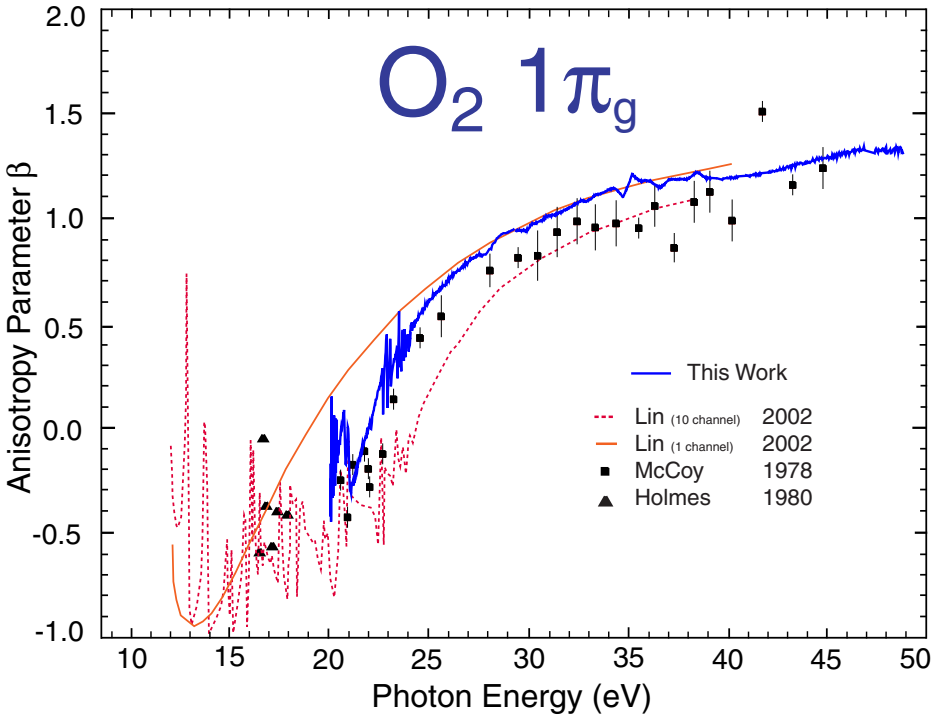

Figure 4.13: Photoelectron angular distribution data as a function of photon energy. The blue line is our data and the theoretical calculations as well as the experimental data included are the same as in figure 4.12.

mentioned no resonance features are discussed in their work.

Figure 4.13 shows our experimental data for the ionization of the O_2 $1\pi_u$ HOMO. Two regions of strong β-spikes can be seen from 19 to 21 eV and from 22.5 to 24.5 eV which is zoomed in in figure 4.14. The theory of Lin (2002) [80] is also included in the figure in order to provide a comparison. The data set is in good principal agreement with former experimental data and with recent theory. The sharp structures observed in our data are the very first indication of these resonances in angle resolved photoelectron spectroscopy.

Regarding the findings in the experimental data of this thesis and the corresponding signatures in the absolute cross section data of Holland *et al.* (1993) [58], the β-resonances are even better observable than the cross section data indicates, showing nicely the increased insight into these dynamics by higher differential

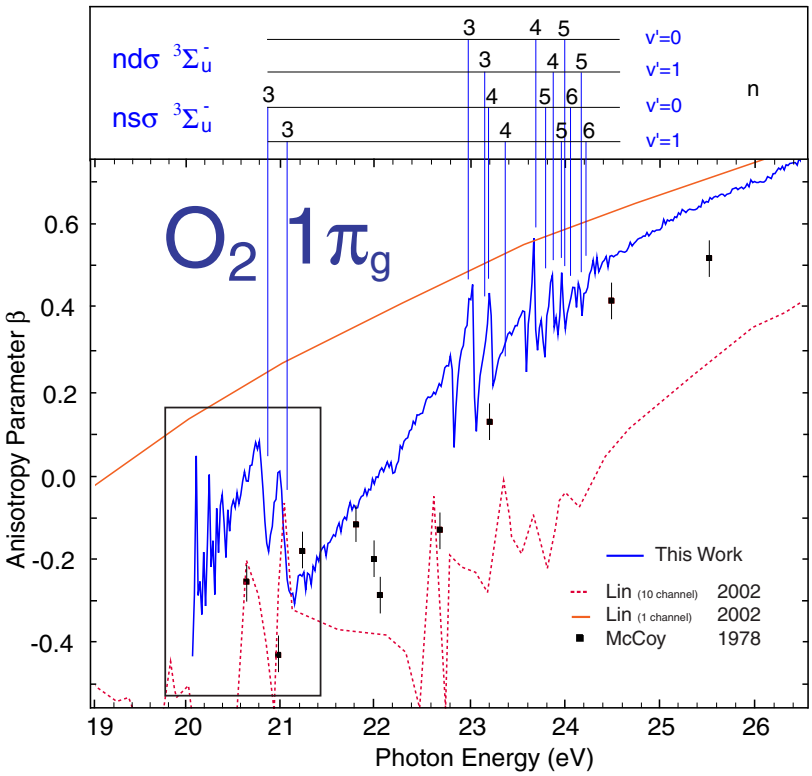

Figure 4.14: Photon energy region where both sets of sharp β-resonances are observed. The inset is enlarged in figure 4.15. The included literature is the same as cited above. All Rydberg series of this photon energy region are depicted according to Holland (1993) [58].

measurements. As it was the case for the N_2 $3\sigma_g$, the observed sharp features can most likely be attributed to the different Rydberg enhanced resonances. The sharp features' photon energy positions are in good agreement in comparison to the cross section data of Holland (1993) [58] (see data of figure 4.11 included in figure 4.14) and therefore it is reasonable to assume a common origin. The depicted series are the $ns\sigma_g$ $^3\Sigma_u^-$ and the $nd\sigma_g$ $^3\Sigma_u^-$, as it is shown in detail in figure 4.14. A clear attribution of the individual vibrational progressions to the observed sharp features in the β-data cannot be done as clear as it was possible for the N_2 $3\sigma_g$, since much more features are included in this work's data. Nevertheless, the situation for O_2 must be similar to N_2 in this concern, so the principal attribution of the observed features to the Rydberg resonances at this photon energy seems to be unambiguous.

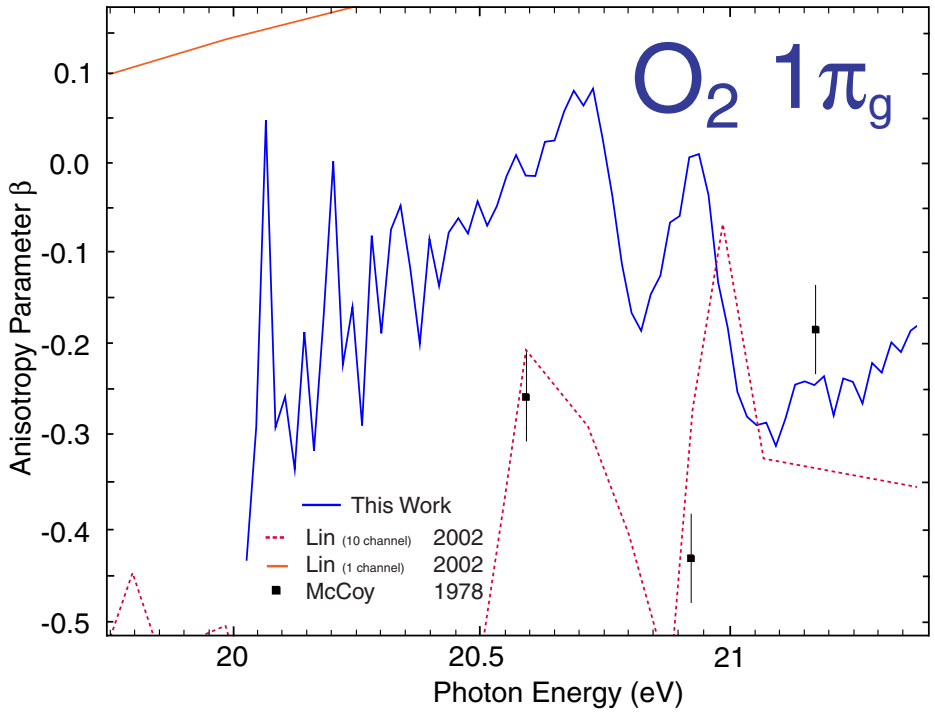

Figure 4.15: Enlarged view on the inset region of figure 4.15. The included literature is the same as cited above.

Summarizing the results for the electron angular distribution of the O_2 $1\pi_g^{-1}$, the experimental data of this thesis found evidence for narrow structures in two separated photon energy regions probably due to Rydberg enhanced autoionization. The presented experimental data find no evidence for broader features, e.g. due to doubly excited valence-like states, as it was the case for N_2 $3\sigma_g$ and N_2 $2\sigma_u$.

4.2 Coherence Effects in Photoionization Processes

Coherence effects of quantum particles like electrons in photoionization processes play a key role in the understanding of quantum mechanical principles. It is not only important to understand the behavior of quantum particles in order to lay the foundation for studies of more complex targets, but it is also essential for the establishment of new experimental techniques like time-resolved measurements with e.g. free-electron-lasers.

Since the variety of coherence effects of quantum particles is far too voluminous to give an absolute overview, some basic examples for coherence in the photoionization of atoms and molecules will be presented here.
In general terms it can be stated that coherent electron emission is evident when two or more indistinguishable transition channels lead to the same final state. Autoionization due to doubly excited states as it was crucial for the discussion in the previous section is one striking example of coherent electron emission in atomic as well as in molecular photoionization. In that particular case one of the electrons is emitted due to the relaxation of the other excited electron in a lower orbital. The resulting final state is the same as it would be for the direct single ionization resulting in the same kinetic energy of the emitted electron. Accordingly, the indistinguishability of both paths leads to a coherent electron emission. The signature of this coherence is indicated by Fano profiles in the intensity distribution of the emitted electrons [46]. At present time (02/2012) this article of Fano (1961) is cited almost 6200 times[1], underlining the immense relevance of this interference interpretation. As shown in the previous section, Fano-like profiles are also observed for the β-parameter implying evidence for similar interference effects. However, the interpretation for angular distribution pattern is more complex than for cross section data.

Another example for coherent electron emission and resulting interference observance is the atomic ionization with ultrashort laser pulses. Pabst *et al.* (2011) [96] presented calculations on interchannel coupling leading to a coherence perturbation in the superposition of created hole states. An ultrashort laser pulse with a spectral bandwidth covering two electronic hole states is usually predicted to lead to a coherent electron emission within this bandwidth. The implied coherence assumption should be true as the uncertainty concerning the ionized

[1] According to Web of Knowledge [134].

orbital is evident. However, Pabst stated the interchannel 'communication' via Coulomb interaction to be that strong that a 'which-way-information' consideration becomes essential. This is especially the case for low kinetic electron energies allowing a longer interaction time with the created hole state fading out to higher kinetic electron energies. Pabst *et al.* (2011) assumes this enhanced entanglement between emitted electron and parent ion to affect future attosecond experiments essentially. These calculations shall be expanded to molecular targets in the near future, since it is interesting to check their relevance for more complex systems. This is one example of a fundamental coherence process which is essential to understand for ultrafast time resolved investigations.

In molecular photoionization additional coherence effects can occur due to persisting partial delocalization of electrons in the molecular orbitals, shape resonances and electron scattering on neighboring atoms. The latter case is also a widely studied field in surface science since these effects are essentially influencing photoelectron spectroscopy studies on solid states (e.g. [145]).

One of the most fundamental coherence effects is the molecular double slit experiment which will be discussed in detail in the following section. Here, coherent emission of photoelectrons due to an indistinguishability of the two (or more) emitter sites is possible [26]. A superposition of the two center interference with one center interference signature is e.g. discussed by Zimmermann *et al.* (2008) [151]. The one center self interference is based on scattering of an electron at the neighboring atom wherefore it can interfere with the non-scattered electron. This scattering process induces a slight momentum change for the ejected electron and therefore induces partial decoherence.

4.2.1 Two Center Interferences

In this section interferences due to a coherent electron emission from two emitter sites will be examined. Recalling the basic explanations of chapter 2, Young type interference is expected to occur due to the indistinguishability and therefore non-locality of these sites as it is the case for homonuclear diatomic molecules [26]. As it was illustrated in a 'Nature News' article by Becker in 2011 [9], the matter-wave interference is strictly based on the Heisenberg uncertainty principle. For the observation of an interference pattern the momentum has to be defined precisely in order to 'generate' a sufficient uncertainty for the locality of the electron. 'Sufficient' in this concern is the coherence assumption meaning

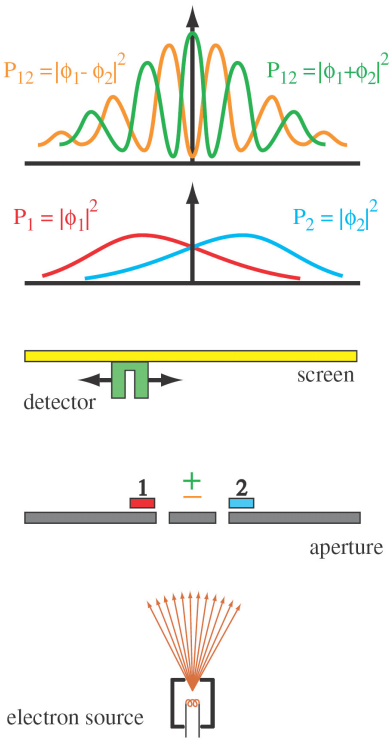

Figure 4.16: The figure adapted from [11] and provided by M. Braune shows a general Young type double slit experiment as it was done by Jönsson in 1961 [66].

that the uncertainty has to be larger than the slit width or the bond length of the molecule respectively. If this coherence is evident, non-locality leads to a coherent superposition of both possible outgoing electron wave functions and interference between these two can be observed. The electron emission can be 'in' or 'out' of phase concerning the gerade and ungerade MO states. Electrons emitted from a gerade state are 'in' phase corresponding to a simple Young type double slit with coherent wave fronts. If the electrons are emitted from an ungerade state, a phase shift of π between both possible wave functions is observed [151]. In the latter case the analogon for a Young type double slit is a tilted wave or as Zimmermann *et al.* (2008) argue it can be interpreted to be an entanglement of the slits through the polarization of the photons.

To highlight the principle of a Young type double slit experiment with quantum particles figure 4.16 is illustrating the formation of corresponding interference pattern. This experiment initially proved the particle-wave dualism which was predicted by de Broglie already in 1924 [33], using an electron source which exposes a double slit setup with electrons. The detection on a screen behind the double slit shows up interference fringes as it is the case for the original experiment of Young and therefore strikingly proving the quantum nature of matter.

In an article of 'Physics World' in 2002 by Robert P. Crease [31], referring to a poll of readers, this experiment of double slit electron diffraction was voted to be

'the most beautiful physical experiment of all times'.

As mentioned earlier, the analogon to this experiment in the molecular case is the electron emission from a gerade state of a homonuclear diatomic molecule since the wave functions of the emitted electrons are 'in phase' or recalling the MO formation $\Psi = \Psi_1 + \Psi_2$. This case is shown in figure 4.16 as the green line in the resulting interference pattern. The maximum here is in the middle of the screen in correspondence to the findings of Jönsson (1961) [66].

Concerning the projection of an ungerade electron emission with $\Psi = \Psi_1 - \Psi_2$ to this basic double slit experiment, one would see antifringes in the interference pattern having a minimum in the middle of the screen. This is, as stated above, by reason of the π phase shift of the electron wave functions.

The Cohen-Fano Formalism from 1966

Cohen and Fano [26] derived their idea of interference effects in molecular photoionization in the light of a molecular double slit for homonuclear diatomic molecules referring to experimental data on N_2 and O_2 photoabsorption cross sections. The presented theoretical approach is, however, calculated for the showcase of H_2. These findings are based on the Born approximation leading to the famous equation for the total absorption cross section [26]

$$\sigma = \Sigma\sigma_l = \frac{\sigma_H(Z^*)}{1+S}[1 + sin(kR)] \tag{4.2}$$

where σ_l are the possible partial ionization cross sections for different angular momentum quantum numbers, σ_H is the total photoionization cross section, Z^* is the atomic number (for hydrogen-like atoms), S is the overlap integral arising from the normalization of the initial wave function [101] and R is the internuclear distance between the two atoms. $[1 + sin(kR)]$ indicates the oscillatory intensity behavior which can be expected to occur in the total photoionization cross section. As already pointed out, this oscillatory behavior is also predicted for the electron angular distribution anisotropy of homonuclear diatomic molecules [130].

Although Cohen and Fano compare their calculations to the experimental data

of Samson *et al.* (1965) [111], they stress the experimental evidence of the predicted oscillations in the photoabsorption cross sections to be 'little'. Further experimental effort done to prove such oscillations at the actual status at 2011 is mainly dedicated to inner shell ionization and the original assumption of Cohen and Fano has not been studied with regard to their chosen examples so far.
Quantum mechanics was omnipresent in physical debate at that time (as it still is) and huge effort was done to develop satisfying explanations on this new physical world's view. It seems to be interesting that the real impact of the Cohen-Fano paper from 1966 was delayed by more than 30 years. Regarding the close relation of this molecular double slit interpretation with the initial quantum particle double slit experiment by Jönsson *et al.* (1961) [66] described above, it is even more astounding that the idea of Cohen and Fano gained its reputation quite recently. Just as a short side note to the development of the paper's relevance, figure 4.17 is illustrating that during the first 10 years the paper was cited frequently, but it did not receive a huge impact as it could be expected. This situation changed dramatically in recent years, the paper's citations increased massively[2], because first experiments proving Cohen-Fano oscillations in inner shells were technically made possible.

It is of fundamental importance for this work to compare the originally predicted data of Cohen and Fano with recent experiments and principal prove of their formalism. As shown for the inner shell ionization of N_2 [151] or as indicated in the vibrational branching ratio data for the N_2 outer valences [21], the studied two center interference pattern have a period length in the order of $> 100\ eV$. Looking at the first figure of the 1966 Cohen-Fano paper, one can see that the presented energy range is way not sufficient to cover even a single period of real two center interferences. Figure 4.18 according to Cohen and Fano (1966) should show oscillations in the total absorption cross section with increasing photon energy due to two center interferences. The 'shoulders' in the data of Samson *et al.* (1965) are thought as experimental evidence, even though Cohen and Fano redundantly state their formalism to be a preliminary construct and not a proved factum. Plotting now recent theoretical cross section data of Toffoli *et al.* (2006) [129] over the experimental data of Samson *et al.* (1965), as it is done in figure 4.19, it is obvious that this experimental data is **no** indication for a molecular double slit behavior of homonuclear diatomic molecules at all. Such oscillations in the total, as well as in the partial cross sections shown in figure 4.19, should range

[2] According to Web of Knowledge [134].

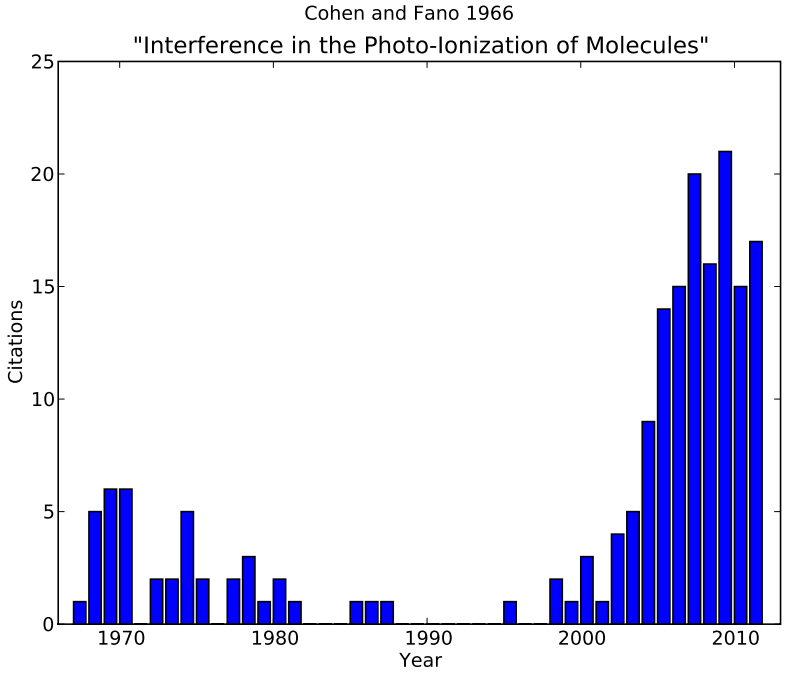

Figure 4.17: The figure shows the quantity of citations of the paper of Cohen and Fano on 'Interference in the Photo-Ionization of Molecules' from 1966 [26] according to 'Web of Knowledge' underlining the actual relevance in scientific interest on related topics.

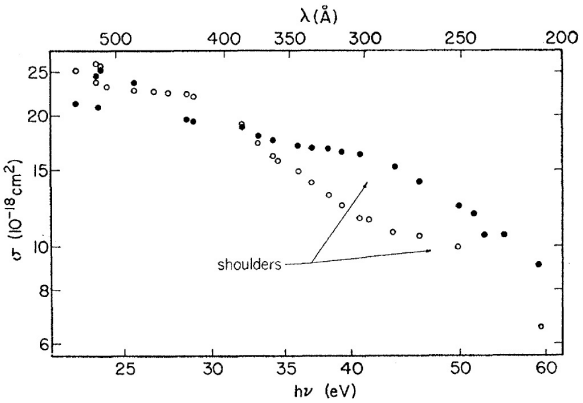

FIG. 1. Logarithmic plot of experimental photoabsorption cross sections (Ref. 1). ● O_2; ○ N_2.

Figure 4.18: Original figure from Cohen and Fano in 1966 [26] showing the cross section data of Samson and Cairns [111].

over several hundreds of eV or referring to the figure over several k (R^{-1}). The wave number k in this respect gives more intuitive insight on the oscillation pat-

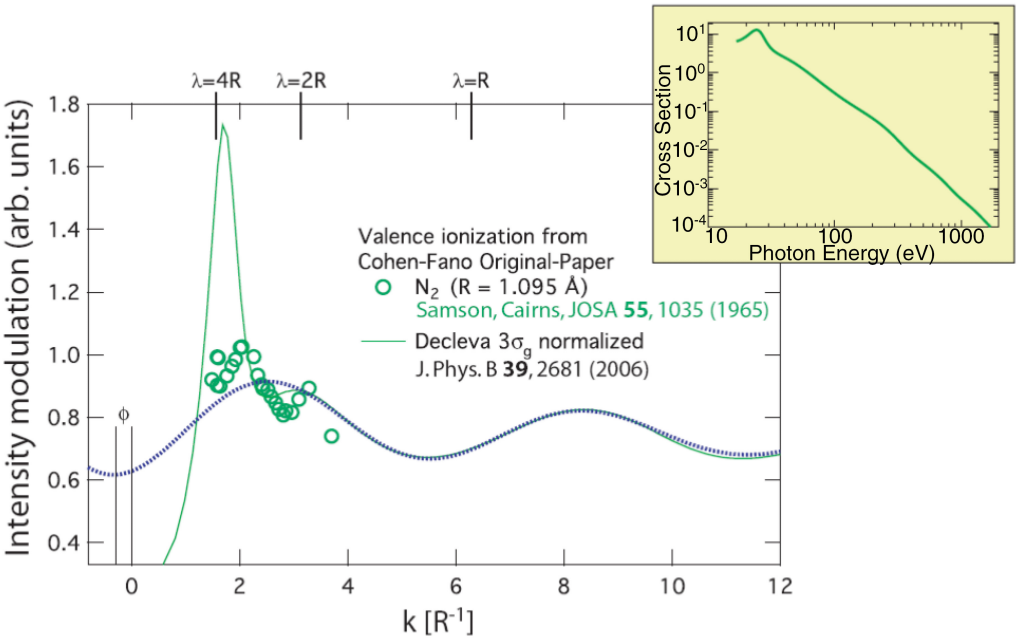

Figure 4.19: Theoretical cross section data of Toffoli *et al.* (2006) [129] and experimental data as it is cited in the Cohen-Fano paper (1966) [111] subtracted from the decreasing cross section trend. Inset: Cross section data of N_2 $3\sigma_g$ without correction. The figure is provided by [75].

tern since the bond length dependence is a sine function according to equation 4.4.

In the figure 4.19 edited by Langer [75], the general shape of the rapidly decreasing cross section (figure's inset upper right) is subtracted to highlight the oscillations. The dotted line is an extrapolation fit of the higher photon energy oscillations to lower energies therefore ignoring shape resonance influences. As already stressed in section 4.1, the experimental data of Samson *et al.* (1965) can accordingly be accounted to the shape resonance of N_2 instead of a real two center interference due to indistinguishable two emitter sites.

Two Center Interference Effects in Inner Shell Ionization Processes

First investigations proving Cohen-Fano oscillations for N_2 have been carried out on the inner shell ionization by Zimmermann *et al.* [151]. Using an electron-ion coincidence spectrometer capable of resolving the g/u splitting of the LCAO of the N $1s$ shells, it was initially shown that the photoionization of gerade and ungerade states shows interference pattern in the measured electron intensities

and that both orbital ionizations do have the predicted phase shift of π. Beside these findings, it is argued that not only two center interference due to undisturbed electron emission, but also one center self interferences are evident. These one center interferences are dominantly influencing the electron angular distribution in the photon energy range below the corresponding de Broglie wavelength. Zimmermann *et al.* (2008) [151] are also presenting such investigations for the heteronuclear CO molecule in correspondence to a double slit including a 'which way information'. A two center interference according to the Cohen-Fano model cannot occur in this case because of a strong localization of the electrons to the C $1s$ and O $1s$ states. This illustrates the gain of delocalization from inner to outer molecular orbitals comparing the results of Canton *et al.* (2011) for the valence ionization of CO.

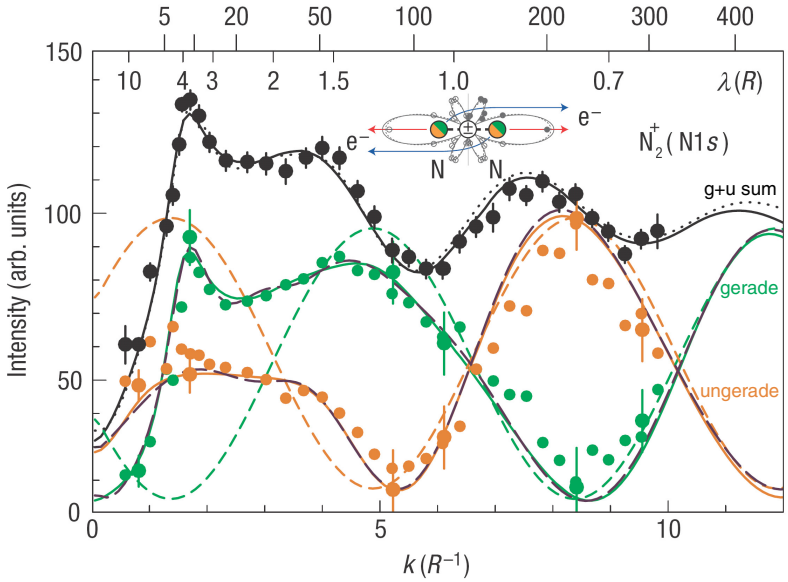

Figure 4.20: The figure is taken from [151] showing the photoelectron diffraction intensities versus electron kinetic energy for electron emission along the direction of the molecular axis of N_2.

Figure 4.20 shows the overlapping effects of electron scattering and two center interference for the inner shell photoionization of N_2 (experimental data points and respective fits). The dashed lines represent the undisturbed two center interference oscillation for the gerade (green), the ungerade (yellow) states. The phase shift of the oscillation between the gerade and ungerade state is π as it is expected from the previously introduced LCAO and double slit considerations.

For the following discussion on such effects for the valence ionization of N_2 and O_2, it is essential that the observed exact phase shift of π of Zimmermann *et al.* (2008) [151][3] can only be expected for inner shell ionization due to the more clearly defined molecular potential. For the valence ionization molecular potential deviations between the respective states are much higher, leading to overlapping phase shifts. The inset of figure 4.20 shows a scheme of the two center electron emission and the resulting superposition of the electron wave functions. It is clearly indicated that electron de Broglie wavelengths below the molecular bond length lead to a domination of the single scattering process. This process includes an electron momentum change larger than the inverse bond length of the N_2 molecule and therefore localization at one atomic site [151]. This process of one center single scattering and the resulting decoherence can be seen in figure 4.20 in the electron kinetic energy region below 100 eV. The two center interference related parts in the intensity distribution are shown by the green and the yellow dashed line for gerade and ungerade states respectively. Regarding higher kinetic energies, the single scattering process decreases in relevance and two center interference gains importance what can be seen by the converging development of the scattered lines and the data points in figure 4.20.

The strong influence of one center single scattering interference is in particular relevant for an inner shell ionization. As it is indicated by our data presented for the photon energy range from 19 to 50 eV for the targets N_2 and O_2, no such strong influence can be observed. The general β-development in the low photon energy range is therefore mainly dominated by Rydberg enhanced resonances and doubly excited valence like states, not by molecular scattering (see also the discussion in the previous section). This difference to the presented inner shell data in figure 4.20 is an interesting fact in order to compare Cohen-Fano oscillations with and without the overlapping signature of induced partial decoherence pattern by the 'extended X-ray absorption fine structure' (EXAFS) scattering.

As figure 4.21 is illustrating, an electron emitted from a homonuclear diatomic molecule like N_2 cannot be said to be localized at a particular atom. This is also true for an inner-shell ionization as e.g. Rolles *et al.* have shown in 2005 [107]. Although an inner shell is not forming a molecular orbital in a comparable way to the valence orbitals, a coherent electron emission from a highly localized inner

[3] As it is also predicted by plane wave approximation calculations.

shell orbital is taking place due to inversion symmetry of the N_2 molecule, i.e. it is not possible to say from which $1s$ orbital the electron is emitted.

The showcase of a comparison of N_2 and CO to clarify the differences of locality is discussed very recently by Canton *et al.* (2011) [21]. As figure 4.21 shows, a localization of an observed electron after emission from the molecule could be attributed to the C-atom or the O-atom due to the differing binding energies of the individual atomic states. This localization of the electron is weak for the molecular valence shells and becomes stronger with increasing binding energies. Partial localization has to be considered. The very unexpected fact of Canton's results was the prove of real two center interference effects, namely Cohen-Fano oscillations for the valence ionization of CO [9]. This means implicitly that the delocalization of the CO valence orbital with respect to the definition of the momentum was sufficient for a coherent electron emission. Therefore, CO as a heteronuclear diatomic molecule was not predicted to show real two center interferences according to the Cohen-Fano formalism before. This observation for a heteronuclear molecule encourages a new view on localization properties and the underlying quantum limitations to interference effects.

Another interesting comparison to the results of Zimmermann *et al.* (2008) [151]

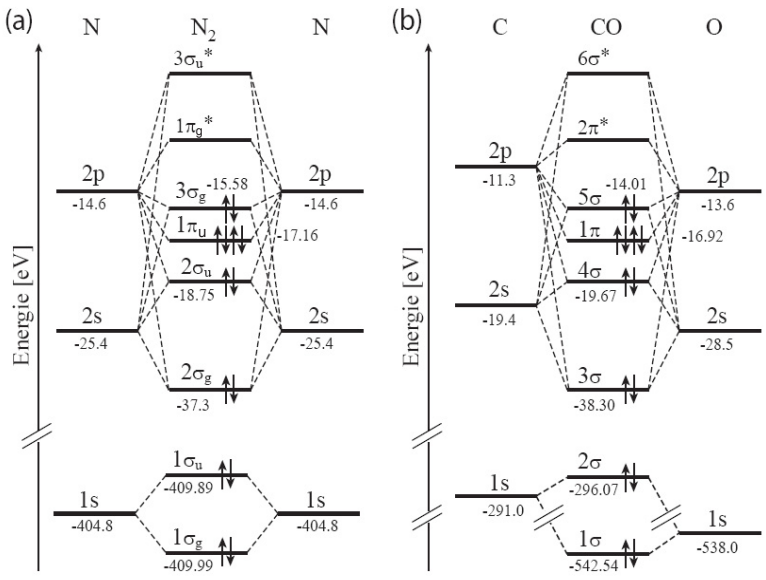

Figure 4.21: Formation of molecular orbitals using LCAO with a notation of the corresponding MOs for N_2 and CO. The figure is taken from [107].

and the very recent data of Canton *et al.* (2011) [21] can be done regarding the differences of CO (inner and valence shell ionization respectively) with the data presented in this chapter on two center interferences of O_2, since only one constituent is changed. Cohen-Fano type interference processes of CO and O_2 can therefore be compared with respect to an 'on/off' delocalization especially in the inner shell photoionization.

In the last sections on low photon energy investigations mainly interchannel coupling and shape resonance effects for the homonuclear diatomic molecules N_2 and O_2 were discussed, presenting highly dense β-data sets. In the photon energy region up to 50 eV, the cross section for the valences of N_2 and O_2 were relatively high. Short acquisition times in the order of less than a minute per data point allowed the realization of such an approach. Analyzing the same valence states for photon energies up to 600 eV is an experimental issue due to both the rapidly decreasing cross section as well as a challenging energy resolution which must still allow to resolve the relevant electron lines. It was therefore not possible to acquire data covering the whole photon energy range presented by Toffoli *et al.* (2006), but it was achievable to record data over more than one full period of the predicted Cohen-Fano oscillation. This initial experimental prove was task of several beamtimes with the two independent experimental setups at DESY in Hamburg and HZB (BESSY II) in Berlin together with the work group of Uwe Becker (Fritz-Haber-Institute of the Max-Planck-Society, Berlin).
The basics of data acquisition and analysis were also presented in chapter 3 and in the first sections of this chapter respectively. The low cross section, the energy resolution recovery with retarding voltages > 500 V and a rising artificial background caused by ions attracted by the negative retarding potentials are inherent difficulties to face for performing such measurements.

4.2.2 Photoelectron angular distributions of N_2 $3\sigma_g^{-1}$

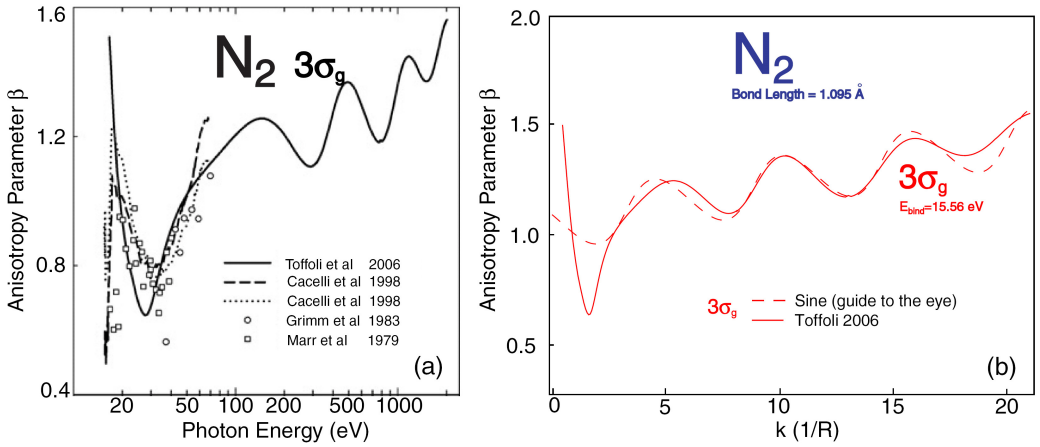

Figure 4.22: (a) Photoelectron angular distribution data for the N_2 $3\sigma_g$ ionization as it is presented in [130]. Figure (b) shows the same DFT-data over the wave number k (R^{-1}) to allow an easy comparison to the sine dependence of the Cohen-Fano oscillation given by equation 4.4.

The photoelectron angular distribution data plotted in figure 4.22(a) shows the calculated β-development over the photon energy. RPA based theoretical data of Cacelli *et al.* (1998) [20] and the experimental data sets of Marr *et al.* (1979) [85] and Grimm *et al.* (1983) [51] cited by Toffoli *et al.* (2006) [130] are included. As discussed before in section 4.1, several interchannel coupling and Rydberg enhanced resonance effects as well as a shape resonance influence lead to discrepancies of Toffoli's (2006) data in comparison to other authors for the low energy range up to $\sim$ 100 eV. The first DFT-calculated maximum of the two center interference pattern lies at $\sim$ 150 eV, the first minimum at $\sim$ 300 eV and the second maximum at $\sim$ 500 eV. The period length of this oscillation increases to higher photon energies in eV, since it is a bond length dependent oscillation. A conversion of this data from photon energy in eV to the wave number k (inverse bond length of N_2) shows that the oscillation pattern indeed is a sine function in this regard as it is predicted by the Cohen-Fano formalism. The amplitude of the shown Cohen-Fano oscillation is in the order of 0.1 β-units for the first period decreasing to higher photon energies.

Bearing in mind that the experimental data acquisition is increasingly difficult for higher photon energies it should again be pointed out that some available experimental β-data even in the low energy regime < 50 eV have larger uncertainties

than the whole effect of Cohen-Fano oscillations in the photoelectron angular distribution of N_2 $3\sigma_g^{-1}$. Acquiring data with high accuracy over such a large photon energy range is therefore a challenge.

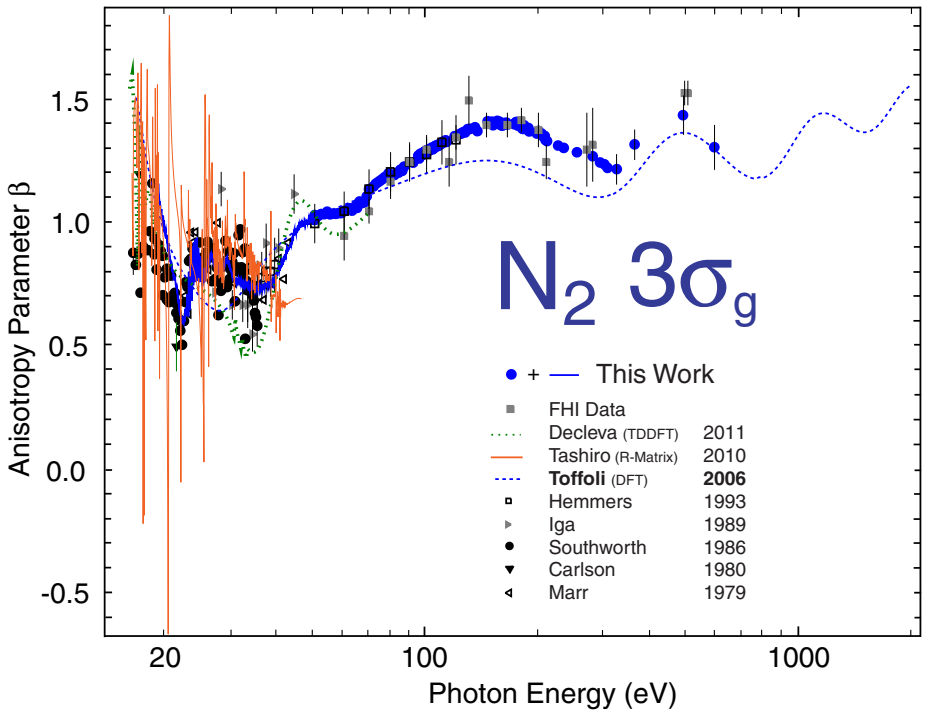

Figure 4.23: Photoelectron angular distribution data for the N_2 $3\sigma_g$ ionization. The experimental and theoretical data in the low energy regime is the same as presented in section 4.1 [23, 36, 55, 63, 85, 120, 126]. The data of this work is plotted as a lineplot in this photon energy region. In the photon energy regime $> 50\ eV$ experimental data of Hemmers (1993) [55] as well as new experimental data from this work (including FHI data) is shown (blue full circles and gray full squares). The theoretical data (dashed blue line) are DFT calculations from Toffoli *et al.* (2006) [130].

The already discussed experimental data available from other authors (cited in the caption of figure 4.23) is plotted in figure 4.23, but they do not substantially contribute to a two center interference discussion. However, a principal comparison of data agreement can be derived which is argued in section 4.1. The data of Hemmers (1993) [55] includes β-data from 20 up to 120 eV which is the broadest photon energy range measured up to now. This dataset is in very good agreement

for higher photon energies $> 40\ eV$ which is reasonable regarding the fact that Hemmers (1993) discusses a consistent β-discrepancy for all the results presented in his work possibly due to a systematic calibration error [55].

The general trend of the experimental data of this thesis, including the data recorded with the complementary experiment of the FHI[4] (see section 3.1.1), agrees well with the calculations of Toffoli *et al.* (2006) [130]. The maxima and minima are in remarkable agreement with respect to their calculated photon energy position, even though the absolute values differ. The data of this thesis as well as data from Hemmers (1993) [55] agrees with the DFT data of Toffoli *et al.* (2006) [130] from ~ 40 to $70\ eV$. Above $70\ eV$ Hemmers' as well as the data from the FHI experiment supports the increase of β overcoming the predicted calculations of Toffoli *et al.* (2006) also indicated by the results of this thesis. The first maximum of the Cohen-Fano oscillation is found at $\sim 150\ eV$. According to the experimental results of this work, the absolute β-value for the first maximum is 1.45 which is a large deviation from the calculated results of Toffoli *et al.* (2006) [130] indicating a maximum to be $\beta = 1.26$. This is also in full agreement with the additional FHI data. With respect to the estimated uncertainty in this photon energy region of about ± 0.02 β-units and the relatively broad maximum feature, one can estimate the photon energy position of the first maximum to be located between 144 and 147 eV in the experimental data. The calculated position is located at $145.6\ eV$ [130] which is in excellent agreement with the data of this thesis.

The absolute offset of ~ 0.2 β-units is consistent up to $\sim 300\ eV$. Furthermore, the experimental data indicates the first minimum to be at $\sim 300\ eV$ not comparably clear in the FHI data. According to the calculations [130], this minimum is located at $289.6\ eV$. Taking into account that the photon energy step width in that energy regime around $300\ eV$ is increased to $1\ eV$ due to the reduced cross section of N_2 and with respect to the larger uncertainties this agreement is still very good. Concerning the absolute β-values, the difference between experiment and theory further decreases to less than 0.1 β-units going up to $h\nu \sim 500\ eV$. At $486\ eV$ and $\beta = 1.37$ the calculations of Toffoli *et al.* (2006) [130] predict the second maximum of the Cohen-Fano oscillation which again is in good agreement with the experimental findings of all analyzed data sets. Since the photon energy

[4] All depicted data points of the complementary FHI experiment also for the following orbitals were analyzed by M. Braune (FHI member at that time) and are provided via private communication.

step width had to be further increased at that high energies, the measurement for this thesis was done at the predicted maximum ($h\nu_{experiment} = 490\,eV$) supporting this to be the right position. The position uncertainty of this second maximum is about $\pm 20\,eV$ due to a step width of 20 eV and an again increased statistical uncertainty. The experimental absolute β at that maximum is found to be 1.45. The additional FHI data points at 490 and 510 eV are observed at $\beta = 1.53$. They exhibit an even larger discrepancy to the theoretical data. Regarding the averaged experimental findings of both experiments at that position, the DFT calculation is giving an absolute β-value unambiguously below the experimental data. Taking into account that the recording of one single β-point at photon energies around 500 eV takes about ten hours of beamtime, despite the fact that the presented experimental setup is highly efficient, an influence of systematical errors might be larger than predicted. To improve the statistical, as well as the systematic reliability, the high photon energy points were measured redundantly at different beamtimes. The results shown in figure 4.23 can therefore be stated to unambiguously prove a larger β-value in comparison to the calculations of Toffoli *et al.* (2006) [130] also for the second maximum of the Cohen-Fano oscillation in the N_2 $3\sigma_g$ ionization.
To clearly prove that the β-values around 500 eV are a distinct maximum, one further point at $h\nu = 600\,eV$ was recorded which should show a β well below that at $\sim 500\,eV$. Indeed this is the case, since the β-value is found to be decreased to 1.3 clearly indicating the beginning of the next oscillation period. Both utilized beamlines ('BW3' at DORIS III and 'UE 56/2 PGM 1' at BESSY II) do not allow reasonable access to valence state electron angular distributions for photon energies far above 600 eV, because the respective cross sections become too small. The upcoming P04 beamline at PETRA III (DESY) will highly increase the available performance and therefore allowing angular distribution studies at even higher photon energies.

In brief conclusion for the data interpretation of the N_2 $3\sigma_g^{-1}$ it can be stated that real two center interference pattern in the photoelectron angular distribution were unambiguously determined in good principal agreement with theory of Toffoli *et al.* (2006) [130] and in very good agreement concerning the extreme positions.

4.2.3 Photoelectron angular distributions of N_2 $1\pi_u^{-1}$

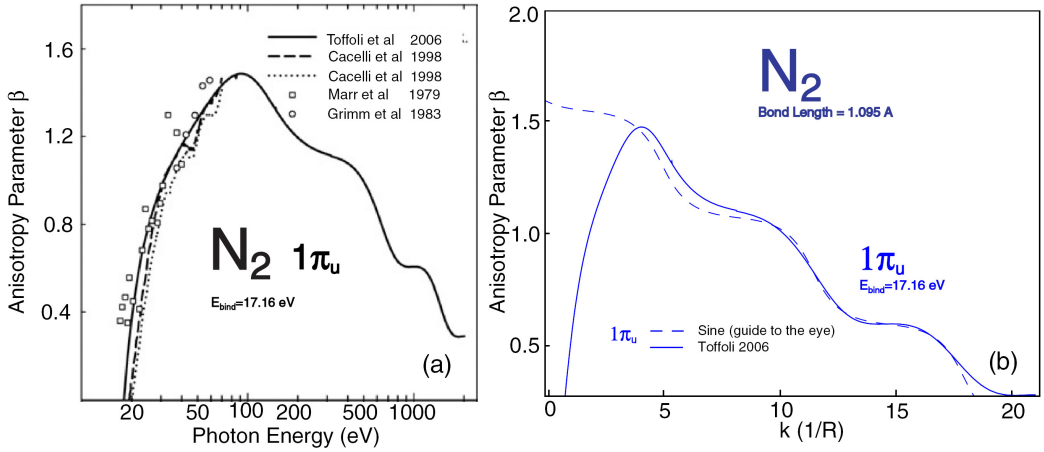

Figure 4.24: (a) Photoelectron angular distribution data for the N_2 $1\pi_u$ ionization taken from [130]. Figure (b) shows the same DFT data as in (a) over $k[R^{-1}]$ again to alleviate the comparison to the underlying sine function.

Figure 4.24(a) shows the original figure taken from Toffoli *et al.* (2006) [130]. The included reference theoretical data from Cacelli *et al.* (1998) [20] is in good agreement with the DFT data, even though DFT neglects interchannel coupling causing a smoother curve without reproducing the features discussed in section 4.1. As it was the case for the $3\sigma_g^{-1}$ state, no additional β-data is available for the $1\pi_u^{-1}$ state above a photon energy of 70 eV with the single exception of Hemmers (1993) [55] where experimental β-data up to 120 eV can be found also for the ionization of this valence orbital (see figure 4.25). In accordance to figure 4.24(a), the experimental data of Marr *et al.* (1979) [85] and Grimm *et al.* (1983) [51], as well as the theoretical data of Cacelli *et al.* (1998) [20] do not show any indication of a two center interference pattern. The decreasing general β-trend beyond ~ 100 eV approaching isotropic angular distribution for very high photon energies can be accounted to the orbital's π shape in the N_2 HOMO-1 regime and the corresponding momentum and scattering properties after photoionization. The superimposed oscillation due to a two center interference is predicted to be even less pronounced than in the $3\sigma_g$ ionization. A measurement of the Cohen-Fano oscillation for the $1\pi_u$ state is therefore even more challenging.
The DFT data predicts the first Cohen-Fano oscillation maximum at $h\nu \sim 90$ eV, being also the maximum of the general trend of the curve. The second maximum is stated to be at $h\nu \sim 450$ eV and the third at $h\nu \sim 1100$ eV. The first minimum

is stated to be at $h\nu \sim 250\ eV$ and the second at $h\nu \sim 800\ eV$ which is also off the experimental access of this work. The maximum amplitude of the oscillation pattern is ~ 0.03 β-units and therefore within our error bars at the relevant high photon energies.

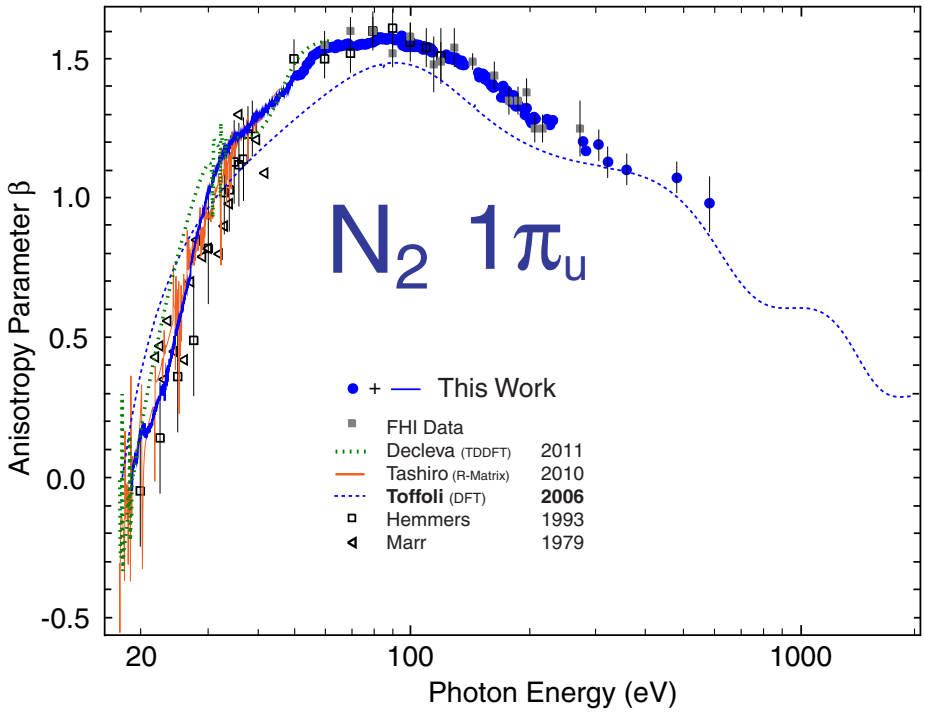

Figure 4.25: Photoelectron angular distribution data for the N_2 $1\pi_u$ ionization. The available experimental and theoretical data in the low photon energy regime is similar to section 4.1 [36, 55, 85, 126]. In the photon energy regime $> 50\ eV$ experimental data of Hemmers (1993) [55] as well as new experimental data from this work (including FHI data) is shown (blue full circles and gray full squares). The theoretical data (dashed blue line) are DFT calculations from Toffoli *et al.* (2006) [130].

Figure 4.25 shows the experimental data of this thesis including the analyzed FHI data for the N_2 $1\pi_u^{-1}$ electrons in comparison to the findings of Toffoli *et al.* (2006) [130], including the relevant experimental data as it is discussed in section 4.1. The additional experimental data of Hemmers (1993) [55] is in good agreement for photon energies between 50 and 120 eV also indicating a slight β-decrease starting at $h\nu \sim 90\ eV$. Even though Hemmers' data is the very first

indication of a distinct maximum in the angular distribution of N_2 $1\pi_u^{-1}$ electrons Hemmers does not discuss this circumstance in his work [55].
As it was the case for the $3\sigma_g$ investigation the first Cohen-Fano oscillation maximum of the $1\pi_u^{-1}$ can be clearly resolved with a high certainty and in remarkable agreement with the theoretical data of Toffoli *et al.* (2006) [130]. With respect to the uncertainty at that photon energy being ± 0.02 β-units, the experimental data of this work finds this maximum between 89 and 91 eV, whereas the calculated position is at $h\nu \sim 91$ eV. Hemmers data (1993) [55] supports this observation, whereas the FHI data shows a small deviation to a lower β-value at 90 eV. In contrast to the large absolute β-offset discussed for the first maximum of the $3\sigma_g^{-1}$ interference pattern, the deviation between theoretical and experimental data at $h\nu = 90$ eV is much smaller for the angular distribution of $1\pi_u^{-1}$ electrons close to the experimental uncertainty of this work. As it was the case for $3\sigma_g$, a β-offset becomes evident, but in the case of the $1\pi_u$ ionization it already starts above ~ 30 eV, persisting up to high photon energies. However, the maximum discrepancy for the $1\pi_u$ electrons is observed to be in the order of 0.1 β-unit.
The first minimum of the predicted Cohen-Fano oscillation for the ionization of the $1\pi_u$ state is difficult to derive accurately from our data. A slightly decreased slope is visible in the experimental data at a reasonable photon energy position ($h\nu \sim 200$ eV). Although the experimental prove of real two center interference pattern for the $1\pi_u^{-1}$ state is less pronounced than in the $3\sigma_g^{-1}$ case, it is visible. This is furthermore corroborated by the fact that the relative intensity ratios of the $3\sigma_g$ and the $1\pi_u^{-1}$ electron line intensities show a distinct oscillation with a significant gerade/ungerade phase shift of the emitted electron wave functions as it will be discussed later in this section.
In conclusion it can be stated that the general agreement of the DFT data [130] and the experimental data of this work (including the FHI data) is very good and even better than for the $3\sigma_g$ angular distribution. However, a prove of Cohen-Fano oscillations in the $1\pi_u$ ionization can be assumed, being not as strong as for the $3\sigma_g$ β due to the very narrow oscillation amplitude superimposed on a strongly changing general trend.

4.2.4 Photoelectron angular distributions of N_2 $2\sigma_u^{-1}$

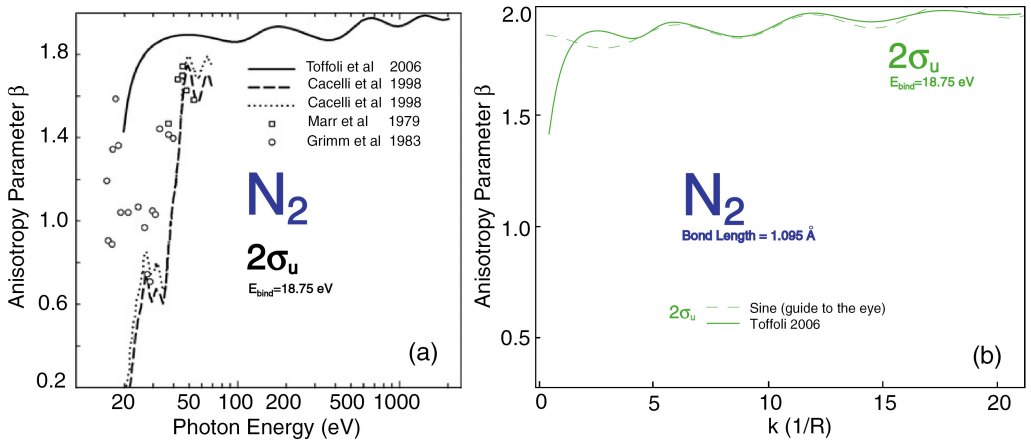

Figure 4.26: (a) Photoelectron angular distribution data for the N_2 $2\sigma_u$ ionization taken from [130]. According to the previous plots figure (b) shows the sine-correspondence of the Cohen-Fano oscillation over $k[R^{-1}]$.

Coming to the third valence state of N_2, namely the $2\sigma_u$, figure 4.26 shows the DFT calculations of Toffoli *et al.* (2006) [130] for the N_2 $2\sigma_u^{-1}$ photoelectrons in comparison to previously available experimental data of [51, 85] and the theoretical data [20] as it was the case for the formerly presented orbitals. A very steep increase of the angular distribution anisotropy parameter β is predicted by both theories and part of the experimental data. The RPA calculations of Cacelli *et al.* (1998) [20] are again essentially differing from the DFT calculations. A remarkable disagreement of the theories and the experimental data cited by Toffoli *et al.* (2006) is evident below $h\nu = 40\ eV$ as it it is discussed in detail in section 4.1. Briefly recalling this section, these discrepancies occur due to a strong impact of interchannel couplings in this photon energy region with a strong influence on the angular distribution of $2\sigma_u$ ionization not included in the DFT calculations. However, the cited data in figure 4.26 can again not contribute to the prove of two center interference pattern in the electron angular distribution. They indicate an even more essential disagreement in the low photon energy range with respect to the theoretical findings of Toffoli *et al.* (2006) than it was the case for the previously discussed orbitals.

As figure 4.26 shows, the first maximum of the predicted Cohen-Fano oscillation is located at $h\nu \sim 49\ eV$ which is in a photon energy range also covered by the calculations of Cacelli *et al.* (1998) [20]. However, these RPA calculations

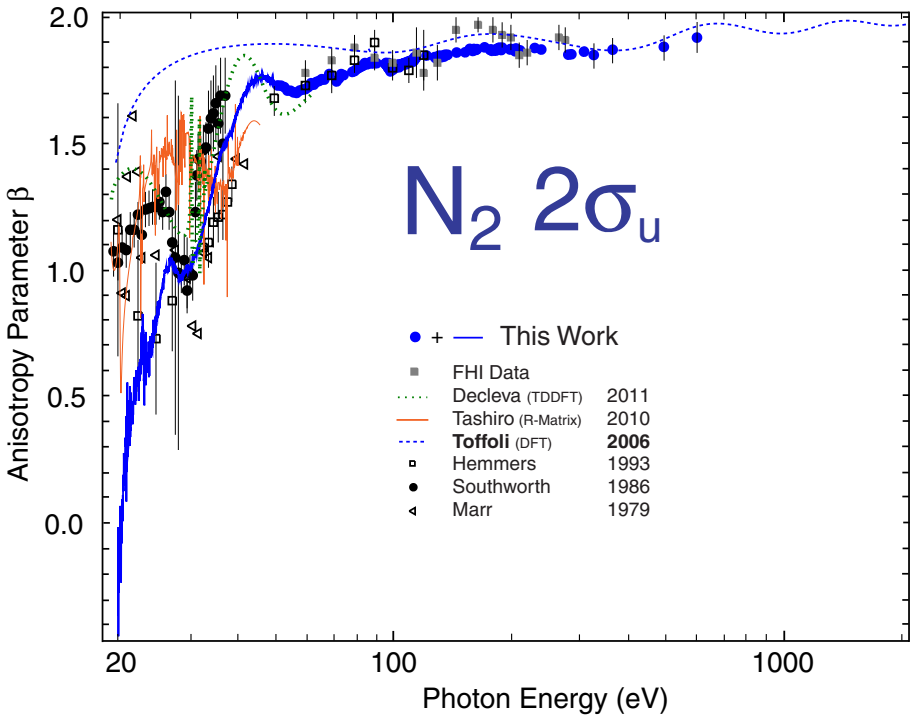

Figure 4.27: Photoelectron angular distribution data for the N_2 $2\sigma_u$ ionization. The available experimental and theoretical data in the low photon energy regime is similar to section 4.1 [36, 55, 85, 120, 126]. In the photon energy regime $> 50\ eV$ experimental data of Hemmers (1993) [55] as well as new experimental data from this work (including FHI data) is shown (blue full circles and gray full squares). The theoretical data (dashed blue line) are DFT calculations from Toffoli *et al.* (2006) [130].

do not indicate a broad maximum as it is the case for the DFT data. The second maximum according to the results of Toffoli *et al.* (2006) [130] is located at $h\nu \sim 178\ eV$, the third at $h\nu \sim 670\ eV$ and a fourth maximum occurring within a photon energy range up to 2 keV for the $2\sigma_u^{-1}$ electrons at $h\nu \sim 1440\ eV$. The respective mimima are located at $h\nu \sim 96\ eV$, $h\nu \sim 370\ eV$ and $h\nu \sim 970\ eV$.

Figure 4.27 shows the experimental data of this work for the angular distribution of $2\sigma_u^{-1}$ electrons in comparison to available experimental and theoretical data according to the discussion in section 4.1. Experimental data of Hemmers (1993) [55] as well as FHI data is additionally included for higher photon energies than 50 eV. Regarding already existing data especially the experimental data of

Hemmers (1993) is very interesting concerning the fact that it contains an undiscussed β-minimum at $h\nu = 90\ eV$ which in the light of the Cohen-Fano formalism and the predictions of Toffoli *et al.* (2006) [130] is very likely to be originated by two center interference. The absolute β-values of this work are lower than the referenced data up to $h\nu \sim 80\ eV$ then converging to the very high absolute β-values of the DFT calculation. Regarding the discussion of Toffoli *et al.* (2006) [130] this is reasonable, since they argue that the used density functional Kohn-Sham Hamiltonian[5] overestimates the cross section for the $2\sigma_u^{-1}$ and neglects electron correlation as it is also the case for the other N_2 valence orbitals. This is most likely also affecting the low photon energy photoionization dynamics of the $2\sigma_u^{-1}$. A better agreement of the experimental data of this work in that photon energy region is observed with the time dependent DFT calculations provided by Decleva (2011) [36] also implemented in figure 4.27 and discussed in section 4.1. These calculations as well as the calculations of Cacelli *et al.* (1998) [20] predict an additional oscillation feature in the β-data between 40 and 70 eV which was neither discussed in the last section nor is it relevant for the topic on two center interferences of this section. It shall anyway be announced that this feature is qualitatively corroborated by our data but not further discussed in literature. Clarifying the origin of this feature will be a task for future interpretation.

As it is the case for the angular distribution of $1\pi_u^{-1}$ electrons, the superimposed Cohen-Fano oscillation on the general β-development of the $2\sigma_u$ ionization is very narrow with an maximum amplitude of ~ 0.03 β-units. Especially for the $2\sigma_u$ this is critical because of the higher statistical uncertainty being ± 0.05 β-units at the photon energy of the first minimum at $h\nu = 90\ eV$. Hemmer's data (1993) [55] as well as the data of this work (including FHI data) supports the theoretical results of Toffoli *et al.* (2006) [130] in terms of extreme positions and absolute β-values but the scatter between the individual data sets indicates a higher uncertainty than it was the case for the previous orbitals. The FHI data shows a very pronounced maximum at around 175 eV being in principle agreement with the theory, whereas the 'BW3'-data shows a more flat, but very consistent development. Regarding the fact that a β-minimum at 200 eV is observed in the FHI data which is absent in the calculations and the complementary experimental data of this work, a larger uncertainty of this data than predicted might be possible. Higher energetic extreme positions predicted by the calculations of Toffoli *et al.* (2006) [130] cannot unambiguously be determined by the experimental

[5] Further details can be read in [109].

data of this work, even though the general agreement with the absolute β-values is good.

Summarizing the results for the N_2 $2\sigma_u^{-1}$ a good absolute agreement of this work's data with the calculations of Toffoli *et al.* (2006) [130] is observed, but due to the very narrow oscillation signature for this orbital, the Cohen-Fano oscillation pattern can only be assumed in the experimental data of this thesis.

4.2.5 Relative cross section ratios between N_2 $3\sigma_g$ and N_2 $1\pi_u$

Although our experimental data does not include total cross section analysis, as it might be interesting in regard of the original prediction of Cohen and Fano (1966) [26] an intensity ratio between corresponding electron lines can be derived from the TOF-spectra and therefore relative partial cross section information can be extracted. The underlying two center interference phenomenon must be the same as it was presented for the angular distribution data above, but the relative cross section ratios are a further way to prove the observed oscillations. The ratios are also including information of a preserved phase shift between the individual orbital's interference pattern.
This ratio calculation has to be done with respect to the electron angular distribution in order to disentangle the respective informations. Since the used experimental setup has no spectrometer at the position of the 'magic angle' at 54.7°, a correction has to be done with respect to the angular position and the corresponding β-parameter. The theoretical (absolute) partial cross section data provided in private communication by Decleva *et al.* (2010) [129] can be used for creating corresponding relative cross sections.
Regarding now the partial cross section ratios between the $3\sigma_g$ and the $1\pi_u$, it is expected that due to the g/u induced partial electron wave phase shift of π and further valence state specific shifts a persisting oscillation is evident. This phase shift for the respective parities was introduced earlier in this section and was strikingly analyzed for the inner shell photoionization of N_2 by Zimmermann *et al.* (2008) [151]. Recalling the findings for the inner shell ionization and the principles of this parity related phase phenomenon, the effective molecular bond length for an inner shell MO is well defined, since the binding energy difference between the N_2 $1\sigma_g$ and the N_2 $1\sigma_u$ is only 100 meV. In that case, the phase dependence is approximately only dominated by the different parities.

To project these findings on the presented valence ionization properties implies a hitherto unseen phase shift evidence between a gerade and an ungerade state of different configuration associations, namely the $3\sigma_g$ and the $1\pi_u$. A conservation of the π phase shift cannot necessarily be expected, because of large deviations of the effective bond lengths between the respective valence orbitals and the randomly aligned targets. Additional phase shifts due to the differing molecular potentials have to be considered.

The DFT data of Decleva *et al.* (2010) [129] shows a nice agreement with our

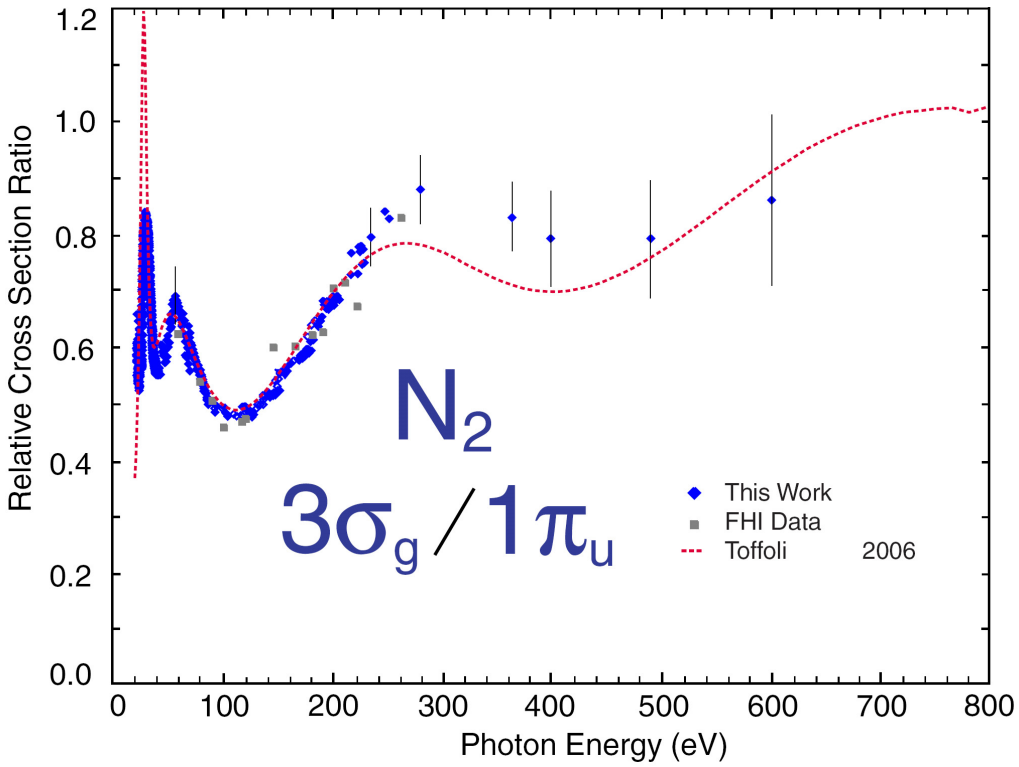

Figure 4.28: Relative partial cross section created by a deviation of the intensities of $3\sigma_g$ and $1\pi_u$ electron lines for the respective photon energy. Theoretical data is provided by Decleva (2010) [129] being calculated in the framework of Toffoli *et al.* [130].

experimental findings for the relative cross section data, especially in the low photon energy range, being an indication for an appropriate use of such an theoretical model (see figure 4.28). Comparing e.g. the theoretical approach of the plane wave approximation, the phase shift would be exactly π between N_2 $3\sigma_g$ and N_2 $1\pi_u$ disregarding the additional influences, obviously highly relevant. The same must be true for the original Cohen-Fano formalism since it is also based on a plane wave approximation. Regarding the real phase shifts of the angular distribution data shown in figure 4.29 the DFT calculations of Toffoli *et al.* (2006) [130] turn out to be an outstanding expansion of the Cohen-Fano formalism supported by the experimental work of this thesis.

Summarizing the results of the angle resolved broad photon energy study of the N_2 outer valence states, two center interferences due to electron emission from indistinguishable two emitter sites were unambiguously determined and discussed

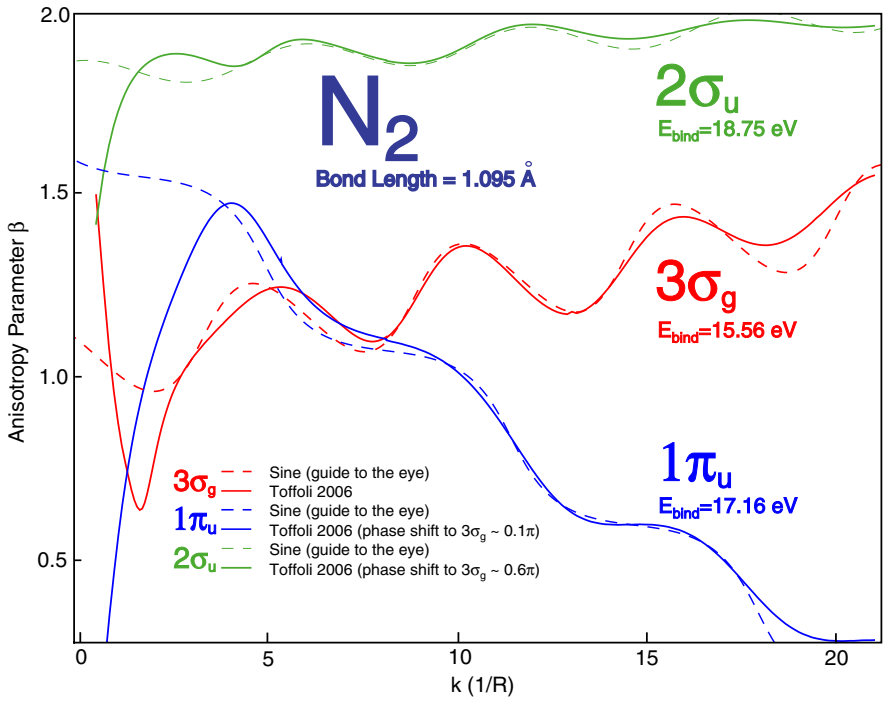

Figure 4.29: The figure includes all theoretical N_2 outer valence angular distribution data plotted over k (R^{-1}). The respective phase shifts between the included sine functions for the 3 orbitals are additionally written in the figure.

in the light of the Cohen-Fano formalism. The experimental data is in good agreement with the theoretical findings of Toffoli *et al.* (2006) [130] concerning the individual orbital's oscillation pattern. Furthermore, the relative cross section ratio data disentangling angular anisotropy and relative electron intensities show nice agreement. The work presented in this thesis is the first experimental prove of Cohen-Fano oscillations in the electron angular distribution of the N_2 outer valence states.

4.2.6 Photoelectron angular distribution of O_2 $1\pi_g^{-1}$

As is predicted in the original paper of Cohen and Fano (1966) [26], two center interferences are also expected to occur in the photoionization of O_2. In this part of the work very first data on the angular distributions for the O_2 HOMO $1\pi_g$ are presented. Since the predicted oscillatory behavior should depend on the ratio of the internuclear distance being larger for O_2 than for N_2, a longer period length in the cross section fluctuations as well as for the electron angular distributions can be expected.
Until now, there is neither theoretical nor experimental data available in this concern which would be highly desirable in order to solve part of the long standing debate on the originally predicted two center interferences for N_2 and O_2 valence ionization. One probable reason for the missing theoretical data concerning O_2 electron angular distribution data is a much more complex electron configuration (see equation 4.2). The presented data of this work on O_2 angular distribution data creates a highly accurate experimental data basis which should encourage an advent of theoretical calculations on this topic. One probable reason for the missing theoretical data concerning O_2 electron angular distribution data is a much more complex electron configuration (see equation 4.2). The presented data of this work on O_2 angular distribution data creates a highly accurate experimental data basis which should encourage an advent of theoretical calculations on this topic.

In comparison to N_2 having an equilibrium bond length of 1.09 $\mathring{A}$ the O_2 molecule has a larger bond length of 1.21 $\mathring{A}$ [139]. Since the two center interference based pattern are bond length dependent regarding equation 4.4 it is, as already stated above, expected that the corresponding Cohen-Fano oscillation for the O_2 $1\pi_g^{-1}$ electrons show a larger period length. As discussed in section 4.1, a relatively steep increase of the angular distribution anisotropy parameter β can be expected regarding theory from e.g. [80] for the low photon energy range which is in good agreement with the experimental data of this work.

Figure 4.30 shows the available experimental and theoretical data for the angular distribution of the $1\pi_g$ ionization of O_2. A clearly defined β-maximum is located at 120 eV. Since the first observed minimum is located at $\sim$ 400 eV, the initial period length is larger than it was the case for all outer valence orbitals of N_2. However, it is remarkable that the first maximum of the Cohen-Fano oscillation for the O_2 $1\pi_g^{-1}$ is observed at a lower photon energy than for all outer valences

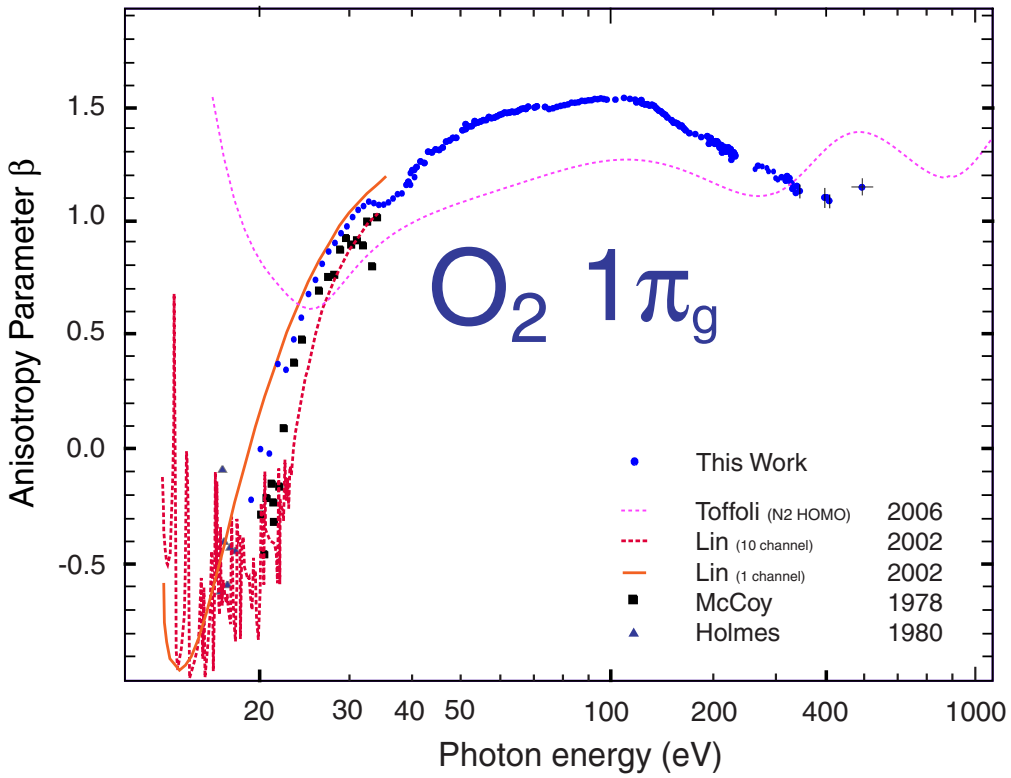

Figure 4.30: Photoelectron angular distribution data for the O_2 $1\pi_g$ ionization. The experimental data in the low energy regime is the same as presented in section 4.1. Theoretical data is taken from Lin *et al.* (2002) [80]. Experimental data is taken from McCoy *et al.* (1978) and Holmes *et al.* (1980) [59, 87]. For a better comparability the DFT β-results of Toffoli *et al.* (2006) [130] for the N_2 $3\sigma_g$ HOMO are included.

of N_2. This suggests that the real Cohen-Fano signature is still influenced by overlapping effects in the photon energy region of $\sim 100\ eV$ afterward evolving increasingly undisturbed. The highest analyzed β-value lies at a photon energy of $500\ eV$, unambiguously indicating the data points around $400\ eV$ to be a distinct minimum of two center interference. The data point at $500\ eV$ depicts both the error bar for the β-uncertainty as well as the average of three data points at the photon energies 495, 500 and $505\ eV$. The analysis of this high photon energy angular distribution is very challenging, because of a small valence electron signal in the photoelectron spectra superimposed on huge non-symmetric Auger electron pattern. Therefore, the background determination for this special case was done using different fit algorithms and exploiting the shifting valence signal with changing photon energy on the fixed Auger electron signal, in order to disentangle

both. Using these procedures and averaging the three independent β-values at closely related photon energies, the certainty was sufficiently increased to indicate the first minimum of a Cohen-Fano oscillation pattern for O_2.

The first maximum of the two center interference pattern of O_2 $1\pi_u^{-1}$ at around 120 eV shows a larger absolute β-value at $\beta = 1.55$ in contrast to the HOMO of N_2. Regarding the first observed maximum and the first minimum of this work's data the Cohen-Fano oscillation amplitude is also larger for this O_2 state as it can nicely be seen in figure 4.30. It can be determined to be 0.45 β-values peak to peak, whereas the maximum amplitude for N_2 $3\sigma_g^{-1}$ is 0.2 β-values. Assuming a similar relative β development for O_2 and N_2, the Cohen-Fano oscillation effect on the electron angular distribution can be extrapolated to be even stronger in O_2 valence ionization than it was the case for N_2.

Briefly concluding the experimental results of this thesis for the O_2 HOMO, it is unambiguously shown that the original assumption of Cohen and Fano of exceeding their formalism based on H_2 to N_2 and O_2 is valid for the valence state electron angular distribution. The two center interference in the O_2 HOMO has been shown for the first time in the framework of this thesis. It is observed to be even stronger than for the corresponding N_2 state also showing the expected longer period length of the two center interference pattern due to a larger internuclear distance. Theoretical calculations for high photon energy angular distributions of O_2 are highly desirable to further interpret and validate the new benchmark data.

4.2.7 Photoelectron angular distribution of CH_4

As a further step to more complex targets CH_4 is investigated in the light of both the near threshold ionization behavior of the electron angular distribution as well as coherent emission from multiple centers. Since there is neither theoretical interpretation nor experimental data available on the topic of high photon energy interferences for CH_4, this work presents initial discussion in this regard. The experimental data of this thesis will be compared to very recent calculations of Decleva (2011) [36] showing first indication of β-oscillations at high photon energies for the CH_4 $1t_2^{-1}$.

CH_4 is a heteronuclear polyatomic molecule and will be presented in this section as a showcase for more complex systems compared to N_2 and O_2. It is investigated to emphasize similarities and differences to homonuclear diatomic molecules. It can be expected that due to the large mass difference and the high symmetry of the CH_4 molecule that vibrational signatures are less pronounced than for homonuclear diatomic molecules. Since the hydrogen atoms are highly symmetrically aligned around the carbon atom with only single bonds (each C-H bond length is $l_{Bond} = 1.09$ $\mathring{A}$), this tetrahedral saturated alkane molecule is still a very simple and therefore theoretically accessible target. Due to the symmetric alignment of the hydrogen atoms the H-H bond length is accordingly $l_{Bond} = 1.54$ $\mathring{A}$. Buckingham *et al.* (1941) initially proposed to regard the four protons around the carbon nucleus as a spherically symmetrical potential field [19, 84] which principally allows an atom-like theoretical treatment of the CH_4 molecule. Its electron configuration of the ground state is [18]

$$1a_1^2\ 2a_1^2\ 1t_{2x}^2\ 1t_{2y}^2\ 1t_{2z}^2. \tag{4.3}$$

According to e.g. Braunstein *et al.* (1988) [18] this ground state configuration of CH_4 suggests a comparison of the valence states of methane to neon regarding their similar electronic properties. The ground state configuration for neon is $(1s)^2\ (2s)^2\ (2p)^6$.
Figure 4.31 shows the evolving electron lines of CH_4 up to a photon energy of 195 eV. The single photoelectron spectrum (figure 4.31(b)) does not resolve the splitting of the HOMO $1t_2$ state into three degenerated energy levels being evident according to e.g. Wang *et al.* (2004) [138]. The literature values for binding energies of the CH_4 valences are ranging within several hundreds of meV between different experiments and theoretical calculations. The binding energies cited in the caption of figure 4.31 are chosen, since they are supported by the experimen-

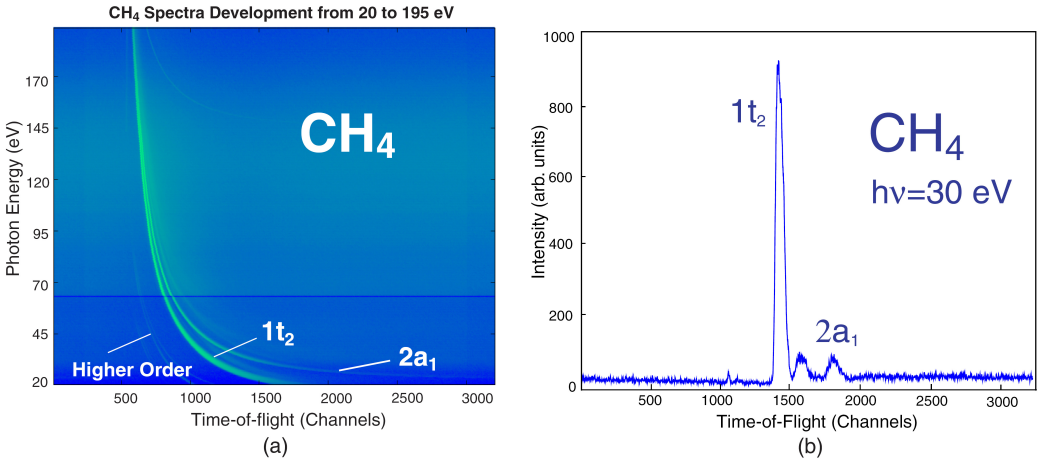

Figure 4.31: (a) False color plot of the photoelectron time-of-flight development of CH_4 from 20 to 195 eV. Figure (b) shows a single spectrum at $h\nu = 30$ eV. The respective binding energies of the $1t_2$ is $E_{bind} \sim 14.5$ eV and for the $2a_1$ is $E_{bind} \sim 23.05$ eV according to experimental data of Banna *et al.* (1975) and references therein [7].

tal data of this work.

The partial cross section of CH_4 $1t_2$ shows strong changes especially in the photon energy region up to 30 eV. In contradiction to the predicted similarity to the Ne valence due to the comparable electron configuration [18, 32, 84] the partial cross sections differ essentially (see figure 4.32). The data shown in figure 4.32 suggests that no sharp fluctuation features in the photoionization cross section occur as it was the case for N_2 and O_2. Further data of Lee et al. (1973) ([78] and references therein) supports this absence of prominent features also for the absolute cross section.

In figure 4.33 photoelectron angular distribution data is presented from 19 to 300 eV. Good qualitative agreement to the available experimental data and the selected theoretical data is achieved. Nevertheless, a significant offset of our data to the data of Holmes *et al.* (1980) [59] in the order of 0.2 β-values is determined which is possibly the case due to a lower photon polarization of $< 80\%$ in their experiments. The β-fluctuation in the photon energy region around ~ 25 eV is according to the given errorbars of Holmes *et al.* (1980) [59] unambiguously evident. No available theoretical or experimental data supports this and also the data presented in this thesis shows very little -if any- comparable structure.

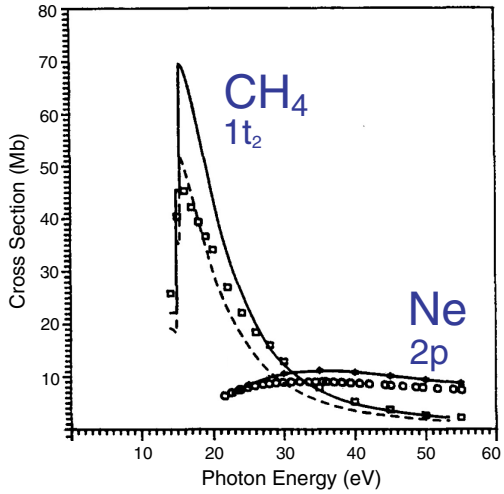

Figure 4.32: Partial cross section of CH_4 $1t_2$ and Ne $2p$ from threshold up to 55 eV taken from Braunstein *et al.* (1988) [18]. The included experimental data is taken from Backx *et al.* (1975) [4] (CH_4 $1t_2$) and West *et al.* (1976) [142] (Ne $2p$).

The theoretical data shown in figure 4.33 is based on different approaches. Rabalais *et al.* (1977) [103] use a orthogonalized plane wave approximation, indicating a steep increase of β from 0 to 1.5 within less than 10 eV. As it was important for the discussion of two center interferences for N_2 and O_2 a plane wave approximation does not take deviations of the molecular potential, especially at short distances, into account. Therefore, its parameters are not sufficient for a precise β calculation.

The calculated data of Braunstein *et al.* (1988) is using a fixed-nuclei approximation at a single nuclear geometry [18]. This data fits much better in the β-development of the experimental data of this thesis although a plateau feature predicted by Braunstein *et al.* (1988) around 30 eV is not in agreement with our data. Good qualitative agreement is observed in comparison to the theoretical data using the time dependent density functional theory approach, provided by Decleva (2011) [36]. Beside a qualitative agreement of the general β-trend this TDDFT data of Decleva (2011) shows a broad superimposed oscillation for higher photon energies. This oscillation is comparable (in period length and amplitude) to the two center interference pattern of N_2 and O_2 as they were presented in the previous section. Initial discussions and considerations suggest that two processes might be the reason for these oscillations. One interpretation is to account these pattern to a scattering of the photoelectrons by the hydrogen atoms. The other

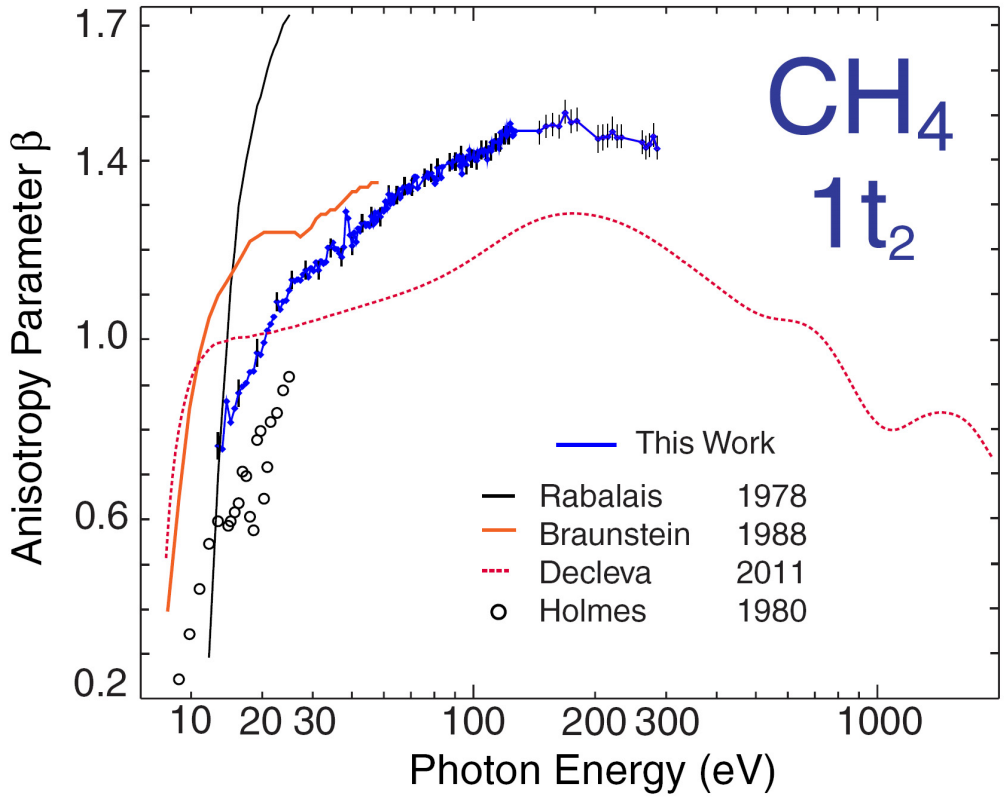

Figure 4.33: Photoelectron angular distribution data for the CH_4 HOMO $1t_2$. Theoretical data of [18, 36, 104] and experimental data of [59] is included in the figure.

possible explanation is that a coherent electron emission due to indistinguishable multiple emitter sites takes place in the photoionization process since the different hybrid orbitals are equal [138] and therefore principally fulfilling the coherence condition in accordance to the Cohen-Fano formalism. This interpretation could then be considered in the light of a molecular multi-slit experiment which has never been done so far.

Although the experimental data of this work do not cover the relevant photon energy range in order to resolve one full period of the predicted oscillation, an initial indication of the first maximum is observed. Since the amplitude of the theoretically predicted oscillation is very small, it is highly challenging to resolve with the new ARPES setup introduced in this work (compare discussion for N_2 $1\pi_u$ in the previous section).

Regarding the general development of the electron angular distribution for the CH_4 $1t_2$ HOMO, it is remarkable that no comparable sharp features were observed in the presented photon energy range as it was the case for N_2 and O_2.

Summarizing the results for the angular distribution data of the CH_4 $1t_2^{-1}$ HOMO, an essential extension of existing data sets supporting the predicted β increase in the low photon energy region as well as the convergence to an absolute β-value of ~ 1.5 are observed. Furthermore, the data of this thesis includes the first indication for the very recent theoretical findings of Decleva (2011) [36] concerning narrow β-oscillations at high photon energies for CH_4. The underlying effect is under discussion to be originated by scattering at the H-atoms or by multi-slit interference in the light of the Cohen-Fano formalism. These calculations all together with the presented experimental results, should encourage further measurements at even higher photon energies as well as a deeper theoretical understanding in order to be able to interpret the predicted β-oscillations for the CH_4 $1t_2^{-1}$ properly.

Chapter 5

Conclusion

The angle resolving electron time-of-flight experiments presented in this thesis are an experimental realization of the molecular double slit experiment proposed by Cohen and Fano in 1966 to angle resolved electron studies of valence states of the homonuclear diatomic molecules N_2 and O_2. In the original assumption of Cohen and Fano a versatile formalism on interference effects in the molecular photoionization has been presented. This formalism has many times been proven to be of far-reaching validity for the description of molecular interference processes due to electron emission from two indistinguishable emitter sites. However, this formalism had to be adapted for an appropriate description of angular distribution effects as it was done by Toffoli *et al.* in 2006. The presented work in this thesis experimentally supports these recent calculations in order to extend the debate on molecular double slit experiments to electron angular distributions. In the light of the originally predicted showcases of the Cohen Fano work of 1966, a comparison between two center interferences from inner shell and valence shell ionization of N_2 shows interesting differences concerning the phase shifts of the Cohen-Fano oscillation pattern in the angular distribution between gerade and ungerade parities. It has been shown that the simple model of a pure parity related electron wave function phase dependence is only valid for the parity splitting of the same orbitals and cannot be extrapolated to different molecular orbitals as it is indicated by the presented showcase of the valence electron lines N_2 $3\sigma_g$ and N_2 $1\pi_u$.

Summarizing the relevance of this thesis's main topic, it shall be pointed out that molecular double slit experiments contain extensive information on photoionization processes, molecular properties and quantum dynamics which can be exploited for a better understanding of more complex systems. Photoelectron

angular distributions of valence electrons for the targets N_2, O_2 and CH_4 were studied in the frame of the Cohen-Fano formalism for the first time, expanding the related debate to higher differential insights experimentally.
A deep understanding of such basic processes is not only essential for the fundamentals of molecular photoemission and quantum dynamics but it is also providing essential information for future experiments e.g. at FEL based light sources where time resolved measurements in a challenging experimental environment will result in observations of completely new photoionization phenomena. But it also complicates the data analysis and interpretation. To face these challenges, it is essential that the relevant effects are well understood and characterized. The results of this thesis contribute in this concern, as they can serve as a solid base and benchmark for future theoretical and experimental work on molecular photoionization dynamics.

Not only the investigations on two center interferences, but additionally the study of near threshold phenomena in the valence photoionization of N_2 and O_2 lead to new considerations of fundamental photoionization dynamics showing hitherto unexplored angular distribution effects for these targets. All topics addressed in this thesis essentially benefit from the highly efficient spectrometer setup developed during the work on this thesis. This experimental development is the basis of these studies in order to face low photoionization cross sections on the one hand and the need for highly dense data sets on the other hand.
The spectrometer setup is also dedicated to online photon beam diagnosis which was tested in several proof-of-principle experiments, highlighting the achieved technical advance leading to more sophisticated diagnostics for storage ring and free-electron-laser based synchrotron radiation sources. Both, in science as well as for diagnostic purposes several new experimental investigations have been realized.

Chapter 6

Outlook

The work presented in this thesis is dedicated to investigations of angular distributions in the frame of the dipole approximation. In future work it would be very interesting to go beyond this approximation and to study Cohen-Fano oscillations from even higher differential perspectives than the β-parameter allows. The theo-

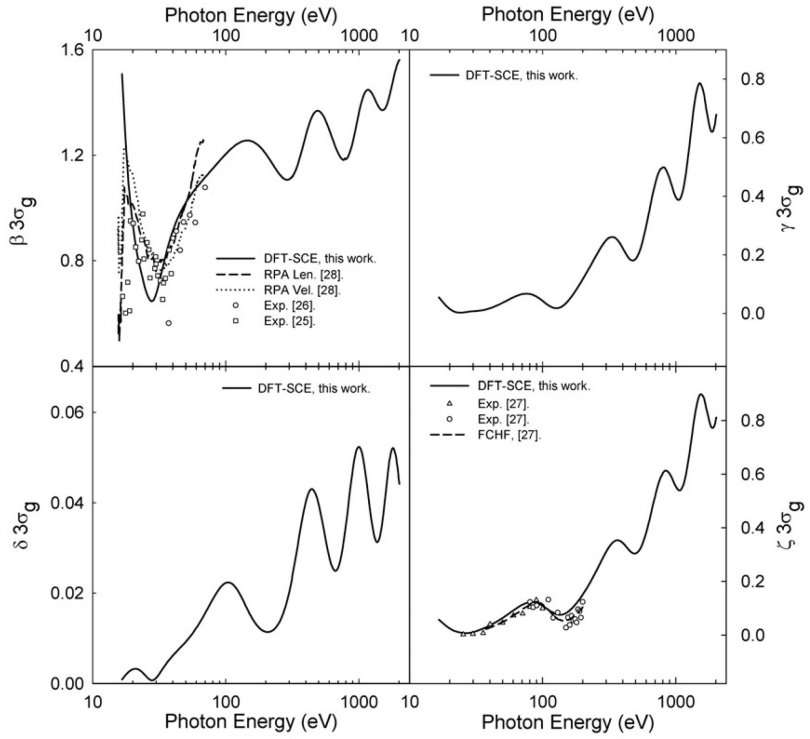

Figure 6.1: The figure shows theoretical calculations of β as well as the non-dipole parameters for the N_2 $3\sigma_g$ ionization as they are plotted in Toffoli *et al.* (2006) [130].

retical data of Toffoli *et al.* (2006) [130] discussed in this thesis also include results for the non-dipole parameters δ, γ and ζ, as well predicting strong Cohen-Fano oscillations for these parameters (see figure 6.1). It is planned to extend the capabilities of the experimental setup for the study of these predicted oscillations in the non-dipole parameters in order to allow additional insight in the fundamental process of such quantum interference effects and their relevance for future studies.

Another complementary approach on studying two center interferences shall be realized, using the electron-electron coincidence technique introduced in chapter 3 of this work. The analysis of such coincidences above the double ionization threshold of the respective targets should show distinct evidence for two center interferences. These even higher differential measurements could be a further step toward a more complex understanding of the underlying phenomenon presented in this thesis. Figure 6.2 shows electron-electron coincidences for nitrogen at a photon energy of 80 eV as a showcase of initial coincidence recording with the new experimental setup. The signatures of the different double ionization processes are angle dependent and the high quantity and efficiency of the spectrometers of the present setup therefore already allow a systematic angle resolving investigation of electron-electron coincidences. It is reasonable to expect a resulting deeper insight into the details of the relevant partial wave compositions influencing the double ionization process in the frame of the Cohen-Fano formalism.

The new P04 beamline at PETRA III will be highly beneficial for such studies with its exceptional high photon flux and energy resolution. As mentioned in chapter 4, the β points taken at high photon energies above 500 eV at the BW3 beamline at DORIS III had acquisition times in the order of 10 hours per data point. This was the main reason why the presented studies in this thesis 'only' cover one full period of Cohen-Fano oscillations. Future experiments at the P04 beamline should reduce the required acquisition times for β data at photon energies even far above 500 eV from hours to minutes. Together with the newly developed highly efficient spectrometer setup this will allow manifold studies of photoionization dynamics.

As already mentioned in the concluding chapter, a distinct understanding of phenomena such as e.g. Cohen-Fano oscillations could be beneficial for future free-electron-laser studies not only by providing benchmark data. Especially when new fields of science are to be explored, as it is still the case for free-electron-laser

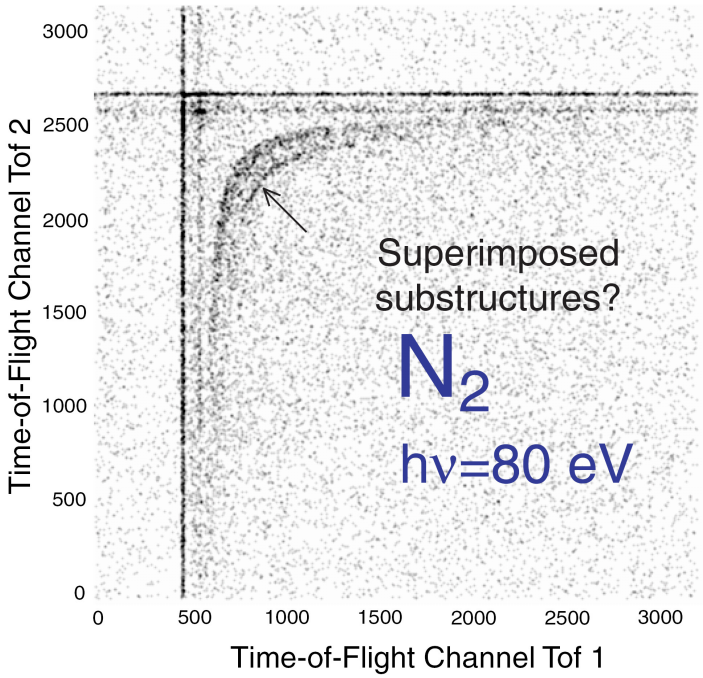

Figure 6.2: The figure shows electron-electron coincidences after N_2 double ionization as they were shown in chapter 3.

experiments, the understanding of all relevant photoionization effects has to be assured to allow for an appropriate data interpretation. Furthermore, it is highly interesting to extend experiments to time-resolved measurements e.g. for probing effects like the two center interferences in the light of molecular dissociation dynamics. Such experiments, investigating the coherence behavior of electron emission evolving during molecular dissociation, have been proposed by Rolles (2005) [107] and recently been realized by Sanov *et al.* (2008) [112].

Chapter 7

Acknowledgements

First of all I would like to thank my advisor Jens Viefhaus at DESY! He has guided my way toward the great research field of atomic and molecular physics and he never became tired in sharing his outstanding expertise. I have never thought such a great support and motivation during the whole time I have been working at DESY to be possible. I am thankful and proud of having been his PhD student.

I believe that the foundation of almost every PhD thesis is a deep dedication to the corresponding field of science and without a great motivation it would surely be hard to realize. I had the opportunity to build up such a dedication and motivation for physics and in senior University years for the research with photons due to the passionate educational environment at the University of Bremen. Especially I would like to thank Prof. Jens Falta and his work group for their exciting lectures and their open minds ensuring the students' interest for such science. Also I would like to thank Prof. Jens Falta for his willingness to review this work and for having supported my wish to do a PhD at DESY right away.

Prof. Thomas Möller was also open to review this thesis right away, what I highly appreciate and would like to greatly acknowledge. Furthermore, I thank him for his advice concerning my future plans and I hope to get the chance to work with him in future collaborative projects. It really impressed me that despite all the widespread duties in his and also Prof. Jens Falta's position there is still time for and so much interest in young scientists' work. Thinking of a longer future, I hope I can adapt this spirit for my own professional life.

Coming to the persons of my every day work at DESY. I have to say that during

my youth I thought work to be the hard part of life or as a friend of mine put it: " If you are having fun, you are not working". During the last years at DESY I got to know that work can be so much more when it motivates every day for realizing great ideas and exploring new exciting properties of our nature. In this concern I would like to thank the HASYLAB in general for the opportunity to use the outstanding photon sources at DESY.

In particular I owe a huge part of my still growing motivation to the people of the P04 work group at PETRA III.
I thank Leif Glaser for all his support during the experimental preparations, the beamtimes and for always having time for help and advice. I really do not appreciate that during the last years he became a better table soccer player than I am, but anyway I am thankful for one or the other game after long working days.
Furthermore, I would like to thank Frank Scholz. His innovative thinking and his ideas for new experimental improvements were always very inspiring. He was always open for questions, new ideas and his dedication for this work's belongings is remarkable. Furthermore, he is undoubtly an essential driving force for the development of the new spectrometer setup presented in this work.
For the help during many beamtimes, many fruitful discussions and just for being very kind colleagues, I would like to thank Sascha Deinert and Jörn Seltmann. Also the help of the students and trainees during my time at DESY shall be acknowledged at this point.
I would finally like to thank Peter Walter for being an outstandingly motivated and competent colleague who always helped me with experimental preparations, technical issues and the realization of all the beamtimes and projects far beyond his usual working times. I had not just the great opportunity to work with such a nice colleague but it became the work with a good friend.

Much more technical and scientific staff of the HASYLAB was responsible for the great working atmosphere and efficiency which initially inspired me to stay at DESY and to start this PhD work. For their patient support concerning the programming of the analysis tools I would like to thank especially Gerd Wellenreuther and André Rothkirch but many more people contributed to this works success.

Since the nature of almost all science is the communication and collaboration with close colleagues and colleagues all around the world, I would like to ac-

knowledge the great input, exciting discussions and fruitful collaborations with e.g. Prof. Uwe Becker, Burkhard Langer and André Meissner from the FHI in Berlin, André Knie from the University of Kassel and Daniel Rolles from the 'Center for Free-Electron-Laser Science'.
Furthermore, I would especially like to thank Markus Braune who offered me the chance to participate in the work of the FHI at the beginning of my PhD work. Under his experimental supervision the Cohen-Fano related measurements were initiated and he was always a very pleasant collaborator.
Not only much of the theoretical basis of this work was created by Prof. Piero Decleva and his associates, he was furthermore a very kind and always interested advisor for the many interpretative questions and suggestions I had concerning the investigations of this work. This kind of communication was very delightful and I really thank Piero for this nice experience.

On the personal side I have been greatly supported by my parents, always having an open ear for me and always taking so much care. I am deeply thankful for having them.
Finally I would like to thank my best friends Olaf, Sören, Alex and Jens for their continuous support in private life and of course my girlfriend Anika for her patience when time was little and for her happy spirit which inspired me many times.

Chapter 8

Abbreviations

ADC Analog to Digital Converter

AMO Atomic and Molecular (Physics)

APPLE II Advanced Planar Polarized Light Emitter II

BESSY Berliner Speicherring Gesellschaft für Synchrotronstrahlung

BW3 Bypass Wiggler 3 am DORIS III Speicherring

CFD Constant Fraction Discriminator

CFEL Center for Free-Electron Laser Science

DESY Deutsches Elektronen Synchrotron

DFT Density Functional Theory

DORIS III Doppel-Ring-Speicher III

EXAFS Extended X-ray-Absorption Fine Structure

FEL Free Electron Laser

FHI Fritz-Haber-Institut der Max Planck Gesellschaft

FLASH Freie-Elektronen-Laser in Hamburg

FWHM Full Width at Half Maximum

GRPAE Generalized Random Phase Approximation with Exchange

HASYLAB Hamburger Synchrotronstrahlungslabor

HF Hartree-Fock

HOMO Highest Occupied Molecular Orbital

HV High Voltage

HZB Helmholtz Zentrum Berlin

IC Interchannel Coupling

IR Infrared

LCAO Linear Combination of Atomic Orbitals

LCLS Linac Coherent Light Source

LS Angular Momentum Coupling

MCP Micro (or Multi) Channel Plate

MO Molecular Orbital

NIM Nuclear Instrumentation Module Standard

PC Personal Computer

PEPICO Photo-Electron Photo-Ion Coincidence Spectroscopy

PES Photoelectron Spectroscopy

PETRA III Positron-Elektron-Tandem-Ring-Anlage III

PGM Plane Grating Monochromator

RC Resistor and Capacitor

RF Radiofrequency

RPA Random Phase Approximation

RCHF Relaxed Core Hartree-Fock

SC Single Channel

SCSI Small Computer System Interface

SCF Self Consistent Field

SLAC Stanford Linear Accelerator

TAC Time to Amplitude Converter

TDC Time to Digital Converter

TDDFT Time Dependent Density Functional Theory

TOF Time-of-Flight

UHV Ultra High Vacuum

UV Ultraviolet

VUV Vacuum Ultraviolet (radiation)

WP 73 Work Package 73 of the European XFEL GmbH

XFEL X-ray Free-Electron-Laser

XPP X-ray Pump Probe

XUV eXtreme Ultraviolet (radiation)

Bibliography

[1] M. Y. Adam, P. Morin, and G. Wendin. Photoelectron satellite spectrum in the region of the 3s Cooper minimum of argon. *Phys. Rev. A*, 31:1426–1433, 1985.

[2] M. Y. Amusia. *Atomic Photoeffect.* Plenum Press, 1990.

[3] M. Y. Amusia. *Theory of Photoionization*, chapter Theory of Photoionization, pages 1–44. Plenum Press, 1996.

[4] C. Backx, G. R. Wight, R. R. Tol, and M. J. Van der Wiel. Electron-electron coincidence measurements of CH_4. *J. Phys. B*, 8:3007–3019, 1975.

[5] K. Balewski, W. Decking, H. Franz, R. Röhlsberger, and E. Weckert. PETRA III: A Low Emittance Synchrotron Radiation Source. Technical Report 0418-9833, Deutsches Elektronen Synchrotron DESY, 2004.

[6] P. Baltzer, B. Wannberg, L. Karlsson, M. Carlsson Göthe, and M. Larsson. High-resolution inner-valence uv photoelectron spectra of the O_2 molecule and configuration-interaction calculation of $^2\Pi_u$ states between 20 and 26 eV. *Phys. Rev. A*, 45:4374–4384, 1992.

[7] M. S. Banna and D.A. Shirley. Molecular photoelectron spectroscopy at 132.3 eV. The second-row hybrides. *J. Chem. Phys.*, 63:4759–4766, 1975.

[8] U. Becker. *VUV and soft X-ray Photoionization.* Plenum Press, New York, 1996.

[9] U. Becker. Matter-wave interference made clear. *Nature Physics*, 474:586–587, 2011.

[10] L.-E. Berg, P. Erman, E. Källne, S. Sorensen, and G. Sundström. Studies of photoionisation and photodissociation of N_2 in the $15 - 30\ eV$ region using intense synchrotron radiation. *Physica Scripta*, 44:131–137, 1991.

[11] Helmholtz Zentrum Berlin. Double slit experiment. http://www.helmholtz-berlin.de/angebote/arbeiten-lernen/info/dualismus/doppelspaltexperiment_en.html, 02 2012. Text to figure written by T. Wilpert and C. Schulz.

[12] N. Berrah, J. Bozek, J.T. Costelloc, S. Düsterer, L. Fang, J. Feldhaus, H. Fukuzawa, M. Hoener, Y.H. Jiang, P. Johnsson, E.T. Kennedy, M. Meyer, R. Moshammer, P. Radcliffe, M. Richter, A. Rouzée, A. Rudenko, A.A. Sorokin, K. Tiedtke, K. Ueda, J. Ullrich, and M.J.J. Vrakking. Non-linear processes in the interaction of atoms and molecules with intense EUV and X-ray fields from SASE free electron lasers (FELs). *Journal of Modern Optics*, 57:1015–1040, 2010.

[13] H. A. Bethe and E. E. Salpeter. *Quantum Mechanics of One and Two-Electron Atoms*. Springer, Berlin, 1957.

[14] N. Bohr. On the Constitution of Atoms and Molecules. *Philosophical Magazine*, 26:4, 1913.

[15] M. Born and R. Oppenheimer. Zur Quantentheorie der Moleküle. *Annalen der Physik*, 389:457–484, 1927.

[16] B.H. Bransden and C.J. Joachain. *Physics of Atoms and Molecules*. Longman Scientific and Technical, New York, 1983.

[17] M. Braunstein and V. McKoy. Shape resonance behavior in $1\pi_u$ photoionization of O_2. *J. Chem. Phys.*, 90:2575–2579, 1989.

[18] M. Braunstein, V.McKoy, L.E. Machado, L.M. Brescansin, and M.A.P. Lima. Studies of the Photoionization of CH_4. *J. Chem. Phys.*, 89:2998–3002, 1988.

[19] R. A. Buckingham, H. S. W. Massey, and S. R. Tibbs. A Self-Consistent Field for Methane and its Applications. *Proc. Roy. Soc. A*, 178:119–134, 1941.

[20] I. Cacelli, R. Moccia, and A. Rizzo. Gaussian-type-orbital basis sets for the calculation of continuum properties in molecules : The differential photoionisation cross section of molecular nitrogen. *Phys. Rev. A*, 57:1895–1905, 1998.

[21] S.E. Canton, E. Plésiat, J.D. Bozek, B.S. Rude, P. Decleva, and F. Martín. Direct observation of Young s double slit interferences in vibrationally resolved photoionization of diatomic molecules. *Proceedings of the National Academy of Sciences (USA)*, 108:7302–7306, 2011.

[22] T. A. Carlson. Angular dependence of vibrational structure in the photoelectronic spectra of N_2 and O_2. *Chem. Phys. Lett.*, 9:23–26, 1971.

[23] T. A. Carlson, M. O. Krause, D. Mehaffy, J. W. Taylor, F. A. Grimm, and J. D. Allen. Angular distribution in the photoelectron spectrum of the ground and first excited vibrational bands of the $X^2\Sigma_g^+$ state in the N_2 measured as a function of photon energy. *J. Chem. Phys.*, 73:6056–6058, 1980.

[24] E. S. Chang. Influence of parity favouredness on the asymmetry of the angular distribution in molecular photoionisation. *J. Phys. B*, 11:L293–L296, 1978.

[25] K. Codling. Structure in the photoionization continuum of N_2 near 500 A. *National Bureau of Standards*, 143:552–558, 1966.

[26] H.D. Cohen and U. Fano. Interference in the Photo-Ionization of Molecules. *Phys. Rev.*, 150:30–33, 1966.

[27] J. Cooper and R. N. Zare. Angular Distributions of Photoelectrons. *J. Chem. Phys.*, 48:942–944, 1968.

[28] J. W. Cooper. Multipole corrections to the angular distribution of photoelectrons at low energies. *Phys. Rev. A*, 42:6942–6945, 1990.

[29] J. W. Cooper and S. T. Manson. Photo-Ionization in the Soft X-Ray Range: Angular Distributions of Photoelectrons and Interpretation in Terms of Subshell Structure. *Phys. Rev.*, 177:157–163, 1969.

[30] M. Coreno, L. Avaldi, R. Camilloni, K. C. Prince, M. de Simone, J. Karvonen, R. Colle, and S. Simonucci. Measurement and ab inition calculation of the Ne photoabsorption spectrum in the region of the K edge. *Phys. Rev. A*, 59:2494–2497, 1999.

[31] R. P. Crease. The most beautiful experiment. *Physics World*, September:97, 2002.

[32] A. Dalgarno. The Photo-Ionization Cross section of Methane. *Proc. Phys. Soc.*, 65:663–667, 1952.

[33] L. V. de Broglie. *Recherches sur la theorie des Quanta.* PhD thesis, University of Paris, 1924.

[34] A. R. B. de Castro and R. Reininger. Optimization of undulators for a SX700 Instrument: Finite element coupled to ray tracing. *Rev. Sci. Instr.*, 63:1317–1320, 1992.

[35] A.R.B. de Castro, C. Bostedt, E. Eremina, M. Hoener, H. Thomas, T. Laarmann, T. Fennel, K.H. Meiwes-Broer, E. Plönjes, M. Kuhlmann, H. Wabnitz, and T. Möller b. Spectroscopy of rare gas clusters using VUV light from a free-electron-laser. *J. Electron Spectrosc. Relat. Phenom.*, 156-158:25–29, 2007.

[36] P. Decleva. N_2 outer valence DFT and TDDFT calculations on partial cross sections and angular distributions. private communication in 2011.

[37] J. L. Dehmer, W. A. Chupka, J. Berkowitz, and W. T. Jivery. Wavelength dependence of the photoelectron angular distributions of the rare gases. *Phys. Rev. A*, 12:1966–1973, 1975.

[38] J. L. Dehmer, D. Dill, and S. Wallace. Shape-Resonance-Enhanced Nuclear-Motion effects in molecular photoionization. *Phys. Rev. Lett.*, 43:1005–1008, 1979.

[39] Ph. V. Demekhin, D. V. Omelyanenko, B. M. Lagutin, V. L. Sukhorukov, L. Werner, A. Ehresmann, K. H. Schartner, and H. Schmoranzer. Investigation of Photoionization and Photodissociation of an Oxygen Molecule by the Method of Coupled Differential Equations. *Optics and Spectroscopy*, 102:318–329, 2007.

[40] M. Domke, K. Schulz, G. Remmers, G. Kaindl, and D. Wintgen. High-resolution study of $^1P^0$ double-excitation states in helium. *Phys. Rev. A*, 53:1424–1438, 1996.

[41] G. Doumy, C. Roedig, S.-K. Son, C. I. Blaga, A. D. DiChiara, R. Santra, N. Berrah, C. Bostedt, J. D. Bozek, P. H. Bucksbaum, J. P. Cryanand L. Fang, S. Ghimire, J. M. Glownia, M. Hoener, E. P. Kanter, B. Kraässig, M. Kuebel, M. Messerschmidt, G. G. Paulus, D. A. Reis, N. Rohringer,

L. Young, P. Agostini, , and L. F. DiMauro. Nonlinear Atomic Response to Intese Ultrashort X Rays. *Phys. Rev. Lett.*, 106:083002–1–4, 2011.

[42] A. Einstein. Über einen die Erzeugung und Verwandlung des Lichtes betreffenden heuristischen Gesichtspunkt. *Annalen der Physik*, 322:132–148, 1905.

[43] J. H. D. Eland, O. Vieuxmaire, T. Kinugawa, P. Lablanquie, R. I. Hall, and F. Penent. Complete Two-Electron Spectra in Double Photoionization: The Rare Gases Ar, Kr, and Xe. *Phys. Rev. Lett.*, 90:053003–1–4, 2003.

[44] A. T. J. B. Eppink and D.H. Parker. Velocity map imaging of ions and electrons using electrostatic lenses: Application in photoelectron and photofragment ion imaging of molecular oxygen. *Rev. Sci. Instr.*, 68:3477–3484, 1997.

[45] J. Falta and T. Möller, editors. *Forschung mit Synchrotronstrahlung*. Vieweg + Teubner, 2010.

[46] U. Fano. Effects of Configuration Interaction of Intensities and Phase Shifts. *Phys. Rev.*, 124:1866–1878, 1961.

[47] R. Feifel, J. H. D. Eland, L. Storchi, and F. Tarantelli. An experimental and theoretical study of double photoionization of CF_4 using time-of-flight photoelectron-photoelectron (photoion-photoion) coincidence spectroscopy. *J. Chem. Phys.*, 125:194318–1–8, 2006.

[48] E. Fermi. Nuclear Physics. *University of Chicago Press.*, 1950.

[49] O. Gabriel. Franck-Condon-Prinzip. http://de.wikipedia.org/wiki/Franck-Condon-Prinzip, 08 2007.

[50] B. Greene. *The Elegant Universe: Superstrings, Hidden Dimensions, and the Quest for the Ultimate Theory*. W.W. Norton, 1999.

[51] F. A. Grimm and T. A. Carlson. Angular distribution for the major photoelectron bands of nitrogen below 45 eV binding energy. *J. Chem. Phys.*, 80:389–394, 1983.

[52] R. E. Grisenti, W. Schöllkopf, J. P. Toennies, G. C. Hegerfeldt, T. Köhler, and M. Stoll. Determination of the Bond Length and Binding Energy of the Helium Dimer by Diffraction from a Transmission Grating. *Phys. Rev. Lett.*, 85:2284–2287, 2000.

[53] P. Gürtler, V. Saile, and E. E. Koch. High resolution absorption spectrum of nitrogen in the vacuum ultraviolet. *Chem. Phys. Lett.*, 48:245–250, 1977.

[54] W. H. Hancock and J. A. R Samson. Angular Distribution of Photoelectrons at 584 $\AA$ using Polarized Radiation. *J. Electron Spectrosc. Relat. Phenom.*, 9:211–216, 1976.

[55] O. Hemmers. *Korrelationseffekte in kleinen Molekülen.* PhD thesis, Technische Universität Berlin, 1993.

[56] O. Hemmers, R. Guillemin, and D.W. Lindle. Nondipole effects in soft X-ray photoemission. *Radiation Physics and Chemistry*, 70:123–147, 2004.

[57] I. V. Hertel and C. P. Schulz. *Atome, Moleküle und optische Physik II.* Springer, 2010.

[58] D. P. Holland, D. A. Shaw, S. M. McSweeney, M. A. MacDonald, A. Hopkirk, and M. A. Hayes. A study of the absolute photoabsorption, photoionisation and photodissociation cross sections and the photoionisation quantum efficiency of oxygen from the ionization threshold to 490 $\AA$. *J. Chem. Phys.*, 173:315–331, 1993.

[59] R. M. Holmes and G. V. Marr. The angular distribution of photoelectrons from N_2, O_2 and CO as a function of photon energy. *Journal of Physics B : Atomic, Molecular and Optical Physics*, 13:945–950, 1980.

[60] K. Hosaka, J. Adach, A. V. Golovin, M. Takahash, T. Teramoto, N. Watanabe, A. Yagishita, S. K. Semenov, and N. A. Cherepkov. Non dipole effects in the angular distribution of photoelectrons from the K shell of N_2 molecule. *J. Phys. B*, 39:L25, 2006.

[61] K. N. Huang, W. R. Johnson, and K. T. Cheng. Theoretical Photoionization Parameters for the Noble Gases Argon, Krypton and Xenon. *Atomic Data and Nuclear Data Tables*, 26:33–45, 1981.

[62] S. Hüfner, editor. *Very High Resolution Photoelectron Spectroscopy.* Springer, 2007.

[63] I. Iga, A. Svenson, and J. B. West. Vibrationally resolved photoelectron angular distributions and branching ratios for the ground state of N_2. *Journal of Physics B : Atomic, Molecular and Optical Physics*, 22:2991–3000, 1989.

[64] W. R. Johnson and K. T. Cheng. Photoionization of the outer shells of neon, argon, krypton, and xenon using the relativistic random-phase approximation. *Phys. Rev. A*, 20:978–988, 1979.

[65] N. Jonathan, A. Morris, M. Okuda, and K. J. Rost. Vacuum Ultraviolet Photoelectron Spectroscopy of Transient Species. *J. Chem. Soc., Faraday Trans. 2*, 70:1810–1818, 1974.

[66] C. Jönsson. Elektroneninterferenzenan mehreren künstlich hergestellten Feinspalten. *Zeitschrift für Physik*, 161:454–474, 1961.

[67] P. N. Juranic, M. Martins, J. Viefhaus, S. Bonfigt, L. Jahn, M. Ilchen, S. Klumpp, and K. Tiedtke. Using I-TOF spectrometry to measure photon energies at FELs. *Journal of Instrumentation*, 4:P09011, 2009.

[68] D. J. Kennedy and S. T. Manson. Photoionization of the Noble Gases: Cross Sections and Angular Distributions. *Phys. Rev. A*, 5:227–247, 1972.

[69] G. C. King, M. Tronc, F. Read, and R. C. Bradford. An investigation of the structure near the $L_{2,3}$ edges of argon, the $M_{4,5}$ edges of krypton and the $N_{4,5}$ edges of xenon, using electron impact with high resolution. *J. Phys. B*, 10:2479–2496, 1977.

[70] E. Kinmond, J. H. D. Eland, and L. Karlsson. Dissociation of N_2O^+ ions from the valence states reached by one-photon photoionisation. *Int. Journal of Mass Spectrometry*, 185-87:437–447, 1999.

[71] L. Kipp. Photoelectron Spectroscopy. *Forschung mit Synchrotronstrahlung*, pages 200–220, 2010.

[72] P. Kolorenc, N. V. Kryzhevoi, N. Sisourat, and L. S. Cederbaum. Interatomic Coulombic decay in a He dimer: Ab initio potential-energy curves and decay widths. *Phys. Rev. A*, 82:013422–1–6, 2010.

[73] A. M. Kondratenko and E. L. Saldin. Generation of Coherent Radiation by a Relativistic Electron Beam in an Undulator. *Part. Accelerators*, 10:207, 1980.

[74] B. Langer. *Anregungsenergieabhängigkeit von Photoelektronensatelliten unter spezieller Berücksichtigung des Schwellbereiches.* PhD thesis, Technische Universität Berlin, 1992.

[75] B. Langer. N_2 cross section oscillation. private communication, 2010.

[76] B. Langer, N. Berrah, R. Wehlitz, T. W. Gorczyca, J. Bozek, and A. Farhat. Angular distribution of the Ne 2s → np autoionization resonances: experimental and theoretical study. *J. Phys. B*, 30:593–607, 1997.

[77] C.U.S. Larsson, A. Bevtler, O. Björneholm, F. Federmann, U. Hahn, A. Rieck, S. Verbin, and T. Möller. First results from the high resolution XUV undulator beamline BW3 at HASYLAB. *Nucl. Instr. and Meth. A*, 337:603–608, 1994.

[78] L. C. Lee, R. W. Carlson, D. L. Judge, and M Ogawa. THE ABSORPTION CROSS SECTIONS OF N_2, O_2, CO, NO, CO_2, N_2O, CH_4, C_2H_4, C_2H_6, AND C_4H_10 FROM 180 TO 700 $\AA$. *J. Quant. Spectrosc. Radiat. Transfer.*, 13:1023–1031, 1973.

[79] J. E. Lennard-Jones. The electronic structure of some diatomic molecules. *Trans. Faraday Soc.*, 25:668–686, 1929.

[80] P. Lin and R. R. Lucchese. Theoretical studies of cross sections and photoelectron angular distributions in the valence photoionization of molecular oxygen. *J. Chem. Phys.*, 116:8863–8875, 2002.

[81] D. Lindle and O. Hemmers. Breakdown of the dipole approximation in soft x-ray photoemission. *J. Electron Spectrosc. Relat. Phenom.*, 100:297–311, 1999.

[82] R. R. Lucchese, G. Raseev, and V. McKoy. Studies of differential and total photoionization cross sections of molecular nitrogen. *Phys. Rev. A*, 25:2572–2587, 1982.

[83] R. R. Lucchese and R. W. Zurales. Comparison of the random-phase approximation with the multichannel frozen-core Hartree-Fock approximation for the photoionization of N_2. *Phys. Rev. A*, 44:291–303, 1991.

[84] G. V. Marr and R. M. Holmes. The angular distribution of photoelectrons from CH_4 as a function of photon energy from near threshold to 30 eV. *Journal of Physics B : Atomic, Molecular and Optical Physics*, 13:939–940, 1980.

[85] G. V. Marr, J. M. Morton, R. M. Holmes, and D.G. McCoy. Angular distribution of photoelectrons from free molecules of N_2 and CO as a function of photon energy. *J. Phys. B*, 12:43–52, 1979.

[86] N. L. S. Martin, D. B. Thompson, R. P. Bauman, C. P. Caldwell, M. O. Krause, S. P. Frigo, and M. Wilson. Electricdipole quadrupole interference of overlapping autoionizing levels in photoelectron energy spectra. *Phys. Rev. Lett.*, 81:1199–1202, 1998.

[87] D. G. McCoy, J. M. Morton, and G. V. Marr. The angular distribution of photoelectrons as a function of photon energy for the ground state photoionisation of molecular oxygen. *Journal of Physics B : Atomic, Molecular and Optical Physics*, 11:547–549, 1978.

[88] J. Mehra and H. Rechenberg, editors. *The historical development of quantum theory Band 2,6.* Springer, 2001.

[89] A. Menzel, S.P. Frigo, S. B. Whitfield, C. D. Caldwell, and M. O. Krause. Partial photoionization cross sections and photoelectron angular distributions for double excitations up to the $N = 5$ threshold in helium. *Phys. Rev. A*, 54:2080–2090, 1996.

[90] M. Meyer, J. T. Costello, S. Düsterer, W. B. Li, and P. Radcliffe. Two-colour experiments in the gas phase. *J. Phys. B*, 43:194006 1–10, 2010.

[91] T. Möller. First Results from the HASYLAB XUV Undulator Beamline BW3. *Synchrotron Radiation News*, 6:16–18, 1993.

[92] T. Möller and C. Kumpf. *Streuung, Absorption und Reflexion*, chapter 2.1, pages 29–54. Vieweg + Teubner, 2010.

[93] M. Mucke, Markus Braune, Silko Barth, Marko Förstel, Toralf Lischke, Volker Ulrich, Tiberiu Arion, Uwe Becker, Alex Bradshaw, and Uwe Hergenhahn. A hitherto unrecognized source of low-energy electrons in water. *Nature Physics*, 6:143–146, 2010.

[94] G. E. Muilenberg, editor. *Handbook of X-ray Photoelectron Spectroscopy.* Perkin-Elmar Coorp. Minnesota, 1979.

[95] NIST. National Institute for Standards and Technology. www.nist.gov, 12 1998.

[96] S. Pabst, L. Greenman, P. J. Ho, D. A. Mazziotti, and R. Santra. Decoherence in Attosecond Photoionozation. *Phys. Rev. Lett.*, 106:05003–1 to 053003–4, 2011.

[97] R.L. Park and G.Lagally. *Solid state physics: surfaces*. Academic Press, 1985.

[98] W. Pauli. *Zeitschrift für Physik*, 31:765, 1925.

[99] Wm. B. Peatman, B. Gotchev, P. Gürtler, E. E. Koch, and V. Saile. Transition probabilities at threshold for the photoionization of molecular nitrogen. *J. Chem. Phys.*, 69:2089–2095, 1978.

[100] M.N. Piancastelli. The neverending story of shape resonances. *J. Electron Spectrosc. Relat. Phenom.*, 100:167–190, 1999.

[101] R. Della Picca, P. D. Fainstein, and A. Dubois. Cooper minima and Young type interferences in the photoionization of H_2^+. *Phys. Rev. A*, 84:033405–1–8, 2011.

[102] M. Planck. Über irreversible Strahlungsvorgaenge. *Sitzungsberichte der Preußischen Akademie der Wissenschaften*, 5:497–480, 1899.

[103] J. W. Rabalais. Principles of Ultraviolet Photoelectron Spectroscopy. *Wiley Interscience*, page 290, 1977.

[104] J. W. Rabalais, T. P. Debies, J. L. Berkosky, J. T. J. Huang, and F. O. Ellison. Calculated photoionization cross sections and relative experimental photoionization intensities for a selection of small molecules. *J. Chem. Phys.*, 61:516–528, 1974.

[105] R. Reininger and V. Saile. A Soft X Ray Grating Monochromator for Undulator Radiation. *Nucl. Instr. and Meth. A*, 288:343–348, 1990.

[106] RIKEN/JASRI. Multistep Ionization of Ar Atoms by Extreme Ultraviolet Free Electron Laser (Press Release). Press Release, 09 2010. http://www.spring8.or.jp/en/news_publications/press_release/2010/100924.

[107] D. Rolles. *Scattering and Coherence Phenomena in the Photoionization of Small Molecules*. PhD thesis, Technische Universität Berlin, 2005.

[108] D. Rolles. *Kohärente Elektronenemission in homonuklearen Molekülen - ein molekulares Doppelspaltexperiment*, chapter 6.1.2, pages 275–282. Vieweg + Teubner Verlag, 2010.

[109] E. Runge and E. K. U. Gross. Density-Functional Theory for Time-Dependent Systems. *Phys. Rev. Lett.*, 52:997–1000, 1984.

[110] Saiht. General principle of ARPES in: Photoemission spectroscopy. Wikipedia: The free Encyclopedia, 06 2009.

[111] J. A. R. Samson and R. B. Cairns. Total absorption cross section of H_2, N_2 and O_2 in the region $550 - 200$ $\AA$. *Journal of Opt. Soc. Am.*, 55:1035, 1965.

[112] A. Sanov and R. Mabbs. Photoelectron imaging of negative ions. *International Reviews in Physical Chemistry*, 27:53–85, 2008.

[113] R. Santra and C. H. Greene. Multiphoton ionization of xenon in the vuv regime. *Phys. Rev. A*, 70:053401–1–8, 2004.

[114] K. H. Schartner, B. Möbus, G. Mentzel, A. Ehresmann, F. Vollweiler, and H. Schmoranzer. Threshold scan of the Ne 2s-electron photoionization cross section. *Phys. Lett. A*, 169:393–395, 1992.

[115] E. Schrödinger. Quantisierung als Eigenwertproblem. *Annalen der Physik*, 79 and 81:361, 489, 734, 109, 1926.

[116] J. Schwinger. On the Classical Radiation of Accelerated Electrons. *Phys. Rev.*, 75:1912–1925, 1949.

[117] K. Siegbahn. Electron Spectroscopy for Atoms, Molecules and Condensed Matter. *Noble Lecture*, pages 1–30, 1981.

[118] A. A. Sorokin, S. V. Bobashev, T. Feigl, K. Tiedke, and M. Richter. Photoelectric Effect at Ultrahigh Intensities. *Phys. Rev. Lett.*, 99:213002–1–4, 2007.

[119] S. H. Southworth, A. C. Parr, J. E. Hardis, J. L. Dehmer, and D. M. P. Holland. Calibration of a Monochromator/Spectrometer System for the Measurement of Photoelectron Angular Distributions and Branching Ratios. *Nucl. Instr. and Meth. A*, 246:782–786, 1986.

[120] S.H. Southworth, A.C. Parr, P.E. Hardis, and J.L. Dehmer. Channel coupling and shape resonance effects in the photoelectron angular distribution of the $3\sigma_g^{-1}$ and the $2\sigma_u^{-1}$ channels of N_2. *Phys. Rev. A*, 33:1020–1023, 1986.

[121] J. A. Stephens and D. Dill. Shape-Resonance effects mediated by channel interaction : Angular distributions of N_2 $2\sigma_u$ photoelectrons. *Phys. Rev. A*, 31:1968–1970, 1985.

[122] N. Stolterfoht, B. Sulik, V. Hoffmann, B. Skogvall, J. Y. Chesnel, J. Rangama, F. Frémont, D. Hennecart, A. Cassimi, X. Husson, A. L. Landers, J. A. Tanis, M. E. Galassi, and R. D. Rivarola. Evidence for Interference Effects in Electron Emission from H_2 Colliding with 60 MeV/u Kr^34+ Ions. *Phys. Rev. Lett.*, 87:023201, 2001.

[123] R. E. Stratmann and R. R. Lucchese. A graphical unitary group approach to study multiplet specific multichannel electron correlation effects in the photoionization of O_2. *J. Chem. Phys.*, 102:8493–8505, 1995.

[124] R.E. Stratmann, G. Bandarage, and R. Lucchese. Electron correlation effects in the photoionization of N_2. *Phys. Rev. A*, 51:3756–3765, 1995.

[125] K. T. Tang, J. P. Toennies, and C. L. Yiu. Accurate Analytical He-He van der Waals Potential Based on Perturbation Theory. *Phys. Rev. Lett.*, 74:1546–1549, 1995.

[126] M. Tashiro. Application of the R-matrix method to photoionization of molecules. *J. Chem. Phys.*, 132:134306–1 to 134306–10, 2010.

[127] Agilent Technologies. DC 282 Specifications. http://www.home.agilent.com/agilent/product.jspx?nid=-35502.733409.00&lc=ger&cc=DE, 2012.

[128] W. Thiel. Theoretical Analysis of Photoelectron Angular Distributions of Linear Molecules. *J. Chem. Phys.*, 77:103–122, 1983.

[129] D. Toffoli and P. Decleva. Absolute partial cross sections for the photoionization of N_2 valence states. priv com.

[130] D. Toffoli and P. Decleva. Photoelectron angular distributions beyond the dipole approximation: a computational study on the N_2 molecule. *J. Phys. B*, 39:2681–2691, 2006.

[131] J. Ullrich, R. Moshammer, A. Dorn, R. Dörner, L. Ph. Schmidt, and H. Schmidt Böcking. Recoil-ion and electron momentum spectroscopy: reaction microscopes. *Rep. Prog. Phys.*, 66:1463–1545, 2003.

[132] http://en.wikipedia.org/wiki/Quantum-number. Quantum number, 12 2011.

[133] http://www.gpta.de/. Time to Digital Converters, 01 2012.

[134] www.webofknowledge.com, 02 2012.

[135] J. Viefhaus. *Emissionsrichtungskorrelationen bei der Untersuchung von Mehrelektronenprozessen*. PhD thesis, Technische Universität Berlin, 1997.

[136] J. Viefhaus. Relative Beam Positioning of the ARPES setup. Proof of principle analysis for beam positioning, 2010.

[137] J. Viefhaus, B. Langer, and K. Wieliczek. Figure of dipole angular distribution anisotropy. private communication.

[138] F. Wang. Molecular orbitals of methane : Symmetry or hybridization. *Journal of Molecular Structure (Theochem)*, 678:105–106, 2004.

[139] Webelements. Nitrogen and Oxygen. http://www.webelements.com/nitrogen/atom_sizes.html and http://www.webelements.com/oxygen/atom_sizes.html, 01 2012.

[140] M. Wellhöfer, J.T. Hoeft, M. Martins, W. Wurth, M. Braune, J. Viefhaus, K. Tiedtke, and M. Richter. Photoelectron spectroscopy as a non-invasive method to monitor SASE-FEL spectra. *Journal of Instrumentation*, 3:P02003, 2008.

[141] G. Wendin. Collective Effects, Relaxation, and Localization of Hole Levels in Atoms, Molecules, Solids, and Adsorbates. *Int. J. Quantum Chem. Symp.*, 13:659–670, 1979.

[142] J. B. West and G. V. Marr. The Absolute Photoionization Cross Sections of Helium, Neon, Argon and Krypton in the Extreme Vacuum Ultraviolet Region of the Spectrum . *Proc. Roy. Soc. A.*, 349:397–421, 1976.

[143] K. Wieliczek. elecion - Data Acquisition Program For GPTA MP^2 TDC Based Systems, 2001-2005. K. Wieliczek Gierkeplatz 10 D-10585 Berlin Germany Tel: +4930 38377665.

[144] Wikipedia. Franck-Condon-principle. http://en.wikipedia.org/wiki/Franck%E2%80%93Condon_principle, 12 11.

[145] D. P. Woodruff. Angular dependence in photoemission: from atoms to surfaces to atoms. *J. Electron Spectrosc. Relat. Phenom.*, 100:259–272, 1999.

[146] C. Y. R. Wu, L. C. Lee, and D. L. Judge. Fluorescence from photofragments as an aid in identifying new molecular states : The N_2 case. *J. Chem. Phys.*, 80:4682–4685, 1984.

[147] F. Wuilleumier and M. O. Krause. Photoionization of neon between 100 and 2000 eV: Single and multiple processes, angular distributions, and subshell cross sections. *Phys. Rev. A*, 10:242–258, 1974.

[148] F. Wuilleumier and M. O. Krause. Redetermination of Partial and Differential Photoionization Cross Sections of L-Subshells of Neon. *J. Electron Spectrosc. Relat. Phenom.*, 15:15–20, 1979.

[149] C. N. Yang. On the Angular Distribution in Nuclear Reactions and Coincidence Measurements. *Phys. Rev.*, 74:764–772, 1948.

[150] T. Young. On the Nature of Light and Colours. *A course of lectures on natural philosophy and the mechanical arts*, 1:464, 1807.

[151] B. Zimmermann, D. Rolles, B. Langer, R. Hentges, M. Braune, S. Cvejanovic, O. Geßner, F. Heiser, S. Korica, T. Lischke, A. Reinköster, J. Viefhaus, R. Dörner, V. McKoy, and U. Becker. Localization and loss of coherence in molecular double-slit experiments. *Nature Physics*, 4:649–655, 2008.